# SUNIVERSITY OF NAPLES "FEDERICO II"
**Polytechnic and Basic Sciences School**

**Department of Chemical Sciences**


**Ph.D School in Chemical Science**

# Structure-function relationships of bacterial glycans in biofilm-associated infections: LPS remodelling in *Pseudomonas aeruginosa* and antibiofilm strategies from *Psychrobacter* sp. TAE2020


**Raffaele D'Amico**

***Supervisor*:** Prof. M.M. Corsaro ***Examiner***: Prof. O.Maglio


**XXXVIII Cycle 2022 – 2025**

***Coordinator*:** Prof. A. Napolitano

## Table of Contents

## List of Abbreviations

| Abbreviation | Meaning |
|---|---|
| AA | *Acetylated Alditols* |
| $Ac_2O$ | *Acetic anhydride* |
| AMGs | *Acetylated O-methyl glycosides* |
| ANOVA | *Analysis of Variance* |
| ATP | *Adenosine Triphosphate* |
| ATCC | *American Type Culture Collection* |
| BHI | *Brain Heart Infusion* |
| CATASAN | *Cold-Adapted Alansan* |
| CF | *Cystic Fibrosis* |
| CFTR | *Cystic Fibrosis Transmembrane Conductance Regulator* |
| MeOH | *Methanol* |
| Chol | *Cholesterol* |
| CLSM | *Confocal Laser Scanning Microscopy* |
| COL1A1 | *Collagen type I alpha-1* |
| COMSTAT | *Software for quantitative 3D biofilm analysis from confocal images.* |
| COSY | *Correlation Spectroscopy (NMR)* |
| COSY-DQF | *Double-Quantum Filtered COSY* |
| CPS | *Capsular Polysaccharide* |
| CPMG | *Carr-Purcell-Meiboom-Gill* |
| CTR | *Control (untreated cells)* |
| DHB | *2,5-Dihydroxybenzoic acid* |
| DNase | *Deoxyribonuclease* |
| DOC-PAGE | *Deoxycholate–Polyacrylamide Gel Electrophoresis* |
| DLS | *Dynamic Light Scattering* |
| DMEM/F12 | *Dulbecco's Modified Eagle Medium / Nutrient Mixture F-12* |
| DMSO | *Dimethyl sulfoxide* |
| DPPC | *Dipalmitoylphosphatidylcholine* |
| E24 | *Emulsification index at 24 h* |
| ECL | *Enhanced Chemiluminescence* |
| eDNA | *Extracellular DNA* |
| ELISA | *Enzyme-Linked Immunosorbent Assay* |
| EPS | *Exopolysaccharides / Extracellular Polymeric Substances* |
| ESI-$MS^n$ | *Electrospray Ionization tandem Mass Spectrometry* |
| EUCAST | *European Committee on Antimicrobial Susceptibility Testing* |
| EVs | *Extracellular Vesicles* |
| FAMEs | *Fatty Acid Methyl Esters* |
| FBS | *Fetal Bovine Serum* |
| GAPDH | *Glyceraldehyde-3-Phosphate Dehydrogenase* |
| GC content | *Guanine-Cytosine content* |
| GC-MS | *Gas Chromatography-Mass Spectrometry* |
| HPLC | *High-Performance Liquid Chromatography* |
| HMBC | *Heteronuclear Multiple Bond Correlation* |
| HR-MAS (NMR) | *High-Resolution Magic Angle Spinning NMR* |
| HSQC | *Heteronuclear Single Quantum Coherence* |

| | |
|---|---|
| IL-6 | *Interleukin-6* |
| Da | *Dalton* |
| λ | *Wavelength* |
| LOS | *Lipooligosaccharide* |
| LPS | *Lipopolysaccharide* |
| $LPS_{H_2O}$ | *LPS fraction from phenol/water extraction (aqueous phase)* |
| $LPS_{PCP}$ | *LPS fraction from phenol/chloroform/petroleum ether extraction* |
| LTA | *Lipoteichoic Acid* |
| MALDI-TOF | *Matrix-Assisted Laser Desorption/Ionization Time-of-Flight* |
| MAS | *Magic Angle Spinning* |
| Mb / Mbp | *Megabase pairs* |
| MDR | *Multi-Drug Resistant* |
| MD-2 | *Myeloid Differentiation factor 2* |
| MS | *Mass Spectrometry* |
| $MS^n$ | *Multistage Mass Spectrometry* |
| MWCO | *Molecular Weight Cut-Off* |
| MTT | *3-(4,5-Dimethylthiazol-2-yl)-2,5-diphenyltetrazolium* |
| NF-κB | *Nuclear Factor kappa-B* |
| NMR | *Nuclear Magnetic Resonance* |
| NOESY | *Nuclear Overhauser Effect Spectroscopy* |
| $OD_{600}$ | *Optical density at 600 nm* |
| $OD_{570}$ | *Optical density at 570 nm* |
| PA14 | *Pseudomonas aeruginosa reference strain PA14* |
| P/W | *Phenol/Water* |
| PBS | *Phosphate-Buffered Saline* |
| PCP | *Phenol/Chloroform/Petroleum ether extraction* |
| PG | *Peptidoglycan* |
| PI | *Phosphatidylinositol* |
| PMAA | *Partially Methylated Alditol Acetates* |
| PNAG | *Poly-N-acetylglucosamine* |
| POPG | *Palmitoyl-oleoyl-phosphatidylglycerol* |
| POPE | *Palmitoyl-oleoyl-phosphatidylethanolamine* |
| POPS | *Palmitoyl-oleoyl-phosphatidylserine* |
| PDR | *Pan-Drug Resistant* |
| QS | *Quorum Sensing* |
| q | *Scattering vector modulus* |
| qRT-PCR | *Quantitative Real-Time PCR* |
| Rg | *Radius of gyration* |
| RIPA | *Radio-Immunoprecipitation Assay* |
| rpm | *Revolutions per minute* |
| RT | *Room Temperature* |
| SAXS | *Small-Angle X-ray Scattering* |
| SD | *Standard Deviation* |
| SDS-PAGE | *Sodium Dodecyl Sulfate-Polyacrylamide Gel Electrophoresis* |
| SEAP | *Secreted Embryonic Alkaline Phosphatase* |
| SLS | *Static Light Scattering* |
| SM | *Sphingomyelin* |
| TA | *Teichoic Acid* |

| | |
|---|---|
| TEM | *Transmission Electron Microscopy* |
| THAP | *2,4,6-Trihydroxyacetophenone* |
| THP1-Blue™ | *THP-1 reporter cell line for NF-κB/SEAP* |
| TFA | *Trifluoroacetic acid* |
| TLR | *Toll-Like Receptor* |
| TLR-4 | *Toll-Like Receptor 4* |
| TOCSY | *Total Correlation Spectroscopy* |
| Tris-HCl | *Tris(hydroxymethyl)aminomethane hydrochloride buffer* |
| TTBS | *Tris-Buffered Saline with 0.05% Tween-20* |
| WB | *Western Blot(ting)* |
| WT | *Wild-Type* |
| ζ-potential | *Zeta potential* |
| RF (coil) | *Radiofrequency coil (NMR probe)* |

## Monosaccharide abbreviations

| Abbreviation | Sugar name |
|---|---|
| **Fuc** | *Fucose* |
| **FucN** | *Fucosamine* |
| **Gal** | *Galactose* |
| **GalA** | *Galacturonic acid* |
| **GalN** | *Galactosamine* |
| **GalNAc** | *N-acetyl-galactosamine* |
| **GalNAcA** | *N-acetyl-galactaminuronic acid* |
| **Glc** | *Glucose* |
| **GlcA** | *Glucuronic acid* |
| **GlcN** | *Glucosamine* |
| **GlcNAc** | *N-acetyl-glucosamine* |
| **Gul** | *Gulose* |
| **GulN** | *Gulosamine* |
| **GulNAc** | *N-acetyl-gulosamine* |
| **GulNAcA** | *N-acetyl-gulosaminuronic acid* |
| **GulN(Pyr)** | *Gulosamine (4,6)-O-pyruvate* |
| **Hep** | *Heptose* |
| **Kdo** | *3-deoxy-D-manno-oct-2-ulosonic acid* |
| **Man** | *Mannose* |
| **ManN** | *Mannosamine* |
| **ManNAc** | *N-acety-mannosamine* |
| **Bac/QuiN4N** | *Bacillosamine/ 2,4-diamino-2,4-dideoxy-quinovose* |
| **Qui** | *Quinovose/ 6-deoxy-glucose* |
| **QuiN** | *Quinovosamine/ 2-amino-2,6-dideoxy-glucose* |
| **Rha** | *Rhamnose* |

# Abstract

This project investigated extracellular glycans produced by different bacterial species to understand how their structures influence physiological adaptations and biological activities, including antimicrobial resistance, immunomodulation, and potential biotechnological applications. Two complementary research lines were pursued: (i) the characterization of extracellular glycans, particularly lipopolysaccharides (LPS), from *Pseudomonas aeruginosa* strains isolated from cystic fibrosis (CF) patients, to assess how structural variations contribute to antibiotic resistance and inflammation; and (ii) the analysis of surface-associated glycans from the non-pathogenic Antarctic bacterium *Psychrobacter* sp. TAE2020 as a source of molecules with antibiofilm activity and potential nanocarrier applications.

For *P. aeruginosa*, six clinical isolates (WT2, WT4, MDR1, MDR5, PDR5, PDR7) and the reference strain PA14 were analyzed under planktonic and biofilm conditions reproducing key features of the CF lung environment. Structural analyses of LPS and lipid A by DOC-PAGE, NMR, HR-MAS NMR, GC-MS, MALDI-TOF, and ESI-MS/MS revealed a conserved lipid A backbone undergoing strain- and condition-specific remodelling, with increased acyl heterogeneity in biofilm-grown and multidrug-resistant strains. Functional assays showed that extracellular molecules produced under biofilm conditions, particularly from WT4 and PDR7, triggered stronger activation of TLR-4, NF-κB, and COL1A1, key mediators of the persistent inflammatory and fibrotic processes typical of CF lungs. qRT-PCR, ELISA, and Western blot analyses confirmed elevated expression of IL-6, TLR-4, and COL1A1 together with NF-κB activation, especially in lipid A and LPS from biofilm-derived PDR7, without inducing cytotoxicity. These findings indicate that specific lipid A remodelling events contribute to sustained inflammatory and fibrotic responses, promoting infection persistence and antibiotic tolerance.

The second research line focused on extracellular glycans from *Psychrobacter* sp. TAE2020. *Psychrobacter* sp. TAE2020 is a Gram-negative bacterium that produces extracellular membrane vesicles (EMVs) and a bioactive complex named CATASAN. The capsular polysaccharide (CPS), the major bioactive component of the CATASAN complex, together with LPS and the outer membrane protein PsyOmp38, shows an unusual tetrasaccharide repeating unit composed of α-D-galactosamine, 2,4-diacetamido-2,4,6-trideoxy-glucose (α-D-bacillosamine), and the rare α-L-gulosamine. This amino sugar-rich composition confers distinctive physicochemical properties, including strong antibiofilm and emulsifying activities. These properties were further enhanced

when CPS was combined with LPS or used to coat liposomes, while depolymerization completely abolished its activity, highlighting the requirement for structural integrity. Confocal laser scanning microscopy and COMSTAT analysis, a software tool for the quantitative evaluation of three-dimensional biofilm structures, showed a marked reduction in biofilm biomass and disruption of biofilm architecture without cytotoxic effects. SAXS and ζ-potential analyses confirmed CPS adhesion to lipid membranes, forming multilayer coatings with physicochemical features suitable for nanocarrier development. LPS from *Psychrobacter* sp. TAE2020 exhibited a rough-type profile containing rhamnose, glucose, glucosamine, and Kdo, with lipid A variably acylated by C10:0, C12:0(3-OH), and C14:0(3-OH).

Overall, this work highlights clear structure-function relationships within extracellular glycans: in *P. aeruginosa*, lipid A remodelling modulates inflammatory and fibrotic responses associated with chronic infection, whereas in *Psychrobacter* sp. TAE2020, amino sugar-rich extracellular glycans emerge as multifunctional biopolymers with antibiofilm, emulsifying, and nanocarrier potential.

## Overview of the Thesis

Glycans are central determinants in the persistence and pathogenicity of biofilm-associated infections. As structural and functional elements, they contribute to microbial adhesion, intercellular cohesion, and matrix formation, while dynamically modulating interactions with the host immune system. In *Pseudomonas aeruginosa*, the clinical model for cystic fibrosis lung infections, glycans such as lipopolysaccharides and exopolysaccharides illustrate this dual role. Structural remodelling of lipid A and alterations in the O-antigen reduce immune recognition and increase resistance to antimicrobial peptides, while the overproduction of alginate, Psl, and Pel polysaccharides stabilizes the biofilm matrix and impedes antibiotic penetration. This combination of surface glycan plasticity and biofilm maturation mechanisms underlies the remarkable persistence of *P. aeruginosa* in chronic airway infections.

Insights from extremophilic microorganisms, particularly Antarctic bacteria, further expand our understanding of glycan-mediated adaptation. *Psychrobacter* sp. TAE2020 produces complex glycoconjugates such as CATASAN, which simultaneously inhibit biofilm formation, block microbial adhesion, and exhibit surfactant and emulsifying properties. These multifunctional roles emphasize how glycans evolved in resource-limited, cold ecosystems provide both ecological advantages and translational potential for anti-biofilm strategies. Furthermore, *Psychrobacter* sp. TAE2020 represents a source of extracellular membrane vesicles. In Antarctic bacteria, vesicles display unique lipid and polysaccharide signatures that confer stability under extreme conditions and enable the transport of bioactive molecules. Compared with synthetic nanocarriers, bacterial EVs are biocompatible, biodegradable, and able to penetrate biofilm matrices, making them particularly attractive for targeting recalcitrant infections.

In conclusion, glycans emerge as the unifying thread linking bacterial adaptation, immune evasion, biofilm-associated resistance, and novel therapeutic opportunities. Understanding their structural variability and ecological functions, from pathogenic models like *P. aeruginosa* to extremophiles such as *Psychrobacter* sp. TAE2020 provides a conceptual and practical framework for developing glycan-inspired strategies. The integration of glycan-based metabolites and extracellular vesicles holds promise for next-generation therapies against chronic infections, combining ecological insight with clinical innovation.

## Take home message

*Ultimately, glycans act as the molecular axis connecting bacterial persistence in chronic infections, such as Pseudomonas aeruginosa in cystic fibrosis, with the adaptive strategies of extremophiles like Antarctic Psychrobacter spp. Their structural plasticity not only sustains biofilm resilience and immune evasion, but also inspires the design of extracellular vesicle-based, glycan-engineered systems as next-generation tools for drug delivery and anti-biofilm therapy.*

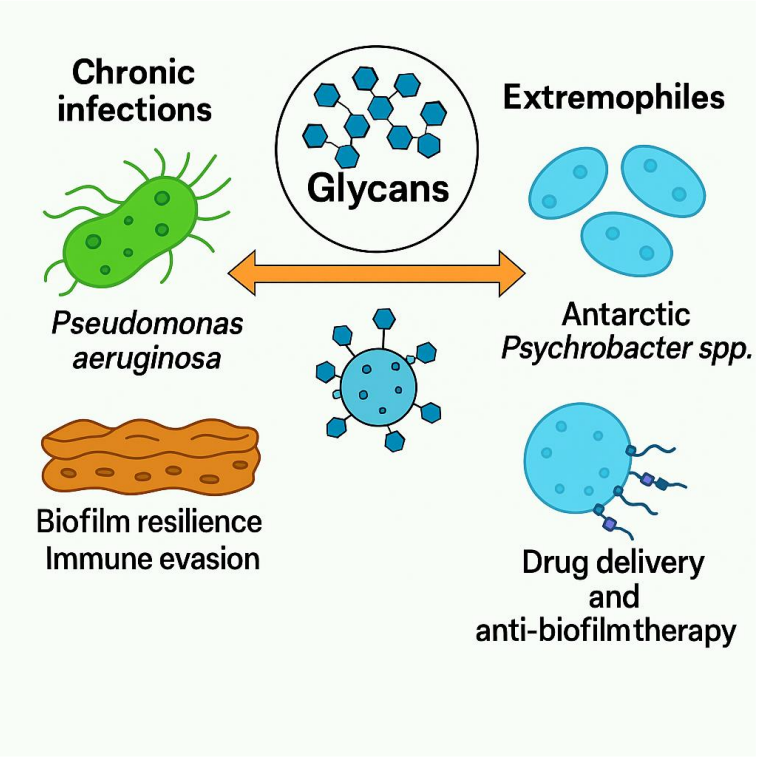


**Fig. I** Role of glycans in biofilm resilience and therapeutic potential from extremophilic bacteria.

**The results presented in this PhD thesis were adapted from the following articles co-authored by the author of the present thesis.**

D'Amico, R., Casillo, A., Olimpo, D., Gallucci, N., D'Angelo, C., Tutino, M. L., Paduano, L., Parrilli, E., & Corsaro, M. M. (2025). Capsular polysaccharide from *Psychrobacter* sp. TAE2020: An unusual amino sugar-enriched macromolecule with anti-biofilm and emulsification activities. *Carbohydrate polymers*, *370*, 124484. https://doi.org/10.1016/j.carbpol.2025.124484.

Casillo, A., D'Amico, R., Lanzetta, R., & Corsaro, M. M. (2024). Marine Delivery Vehicles: Molecular Components and Applications of Bacterial Extracellular Vesicles. *Marine drugs*, *22*(8), 363. https://doi.org/10.3390/md22080363.

D'Amico, R., Vassallo, V., Paris, I., Trecca, M., Casillo, A., Schiraldi, C., Papa, R., & Corsaro, M.M. Biofilm and Planktonic Lifestyles Modulate Lipid A Structure and Inflammatory Response in *Pseudomonas aeruginosa* from People with Cystic Fibrosis. *Scientific reports.* Manuscript accepted for publication.

**Manuscript in preparation**

D'Amico, R., Casillo, A., Jachymek, W., Papa, R., Maciejewska, A., Kaszowska, M., Lukasiewicz, J. & Corsaro, M.M. Structure–Activity Relationship of Glycoconjugates in Pan-Drug Resistant *Pseudomonas aeruginosa.*

References to the related publications are provided throughout the thesis.

Parts of the experimental work and results presented in this thesis have been previously published in peer-reviewed journals. Access to some publications may be restricted by copyright; therefore, only summarized or re-elaborated versions of the results are included here, with proper citation of the sources. Any figures or excerpts of text reproduced from published articles are included exclusively for academic and non-commercial purposes, in compliance with copyright regulations, and are intended solely for inclusion in this doctoral dissertation.

**Collaborations**

Several experimental activities presented in this thesis were carried out in collaboration with different research groups and have been partially reported in scientific publications.

Analyses related to molecular weight determination, aggregation, and adhesion properties were performed in collaboration with the Department of Chemical Sciences, University of Naples "Federico II" (Prof. Luigi Paduano and Dr. Noemi Gallucci).

Bacterial growth experiments involving *Pseudomonas aeruginosa* were carried out in collaboration with the Department of Public Health and Infectious Diseases, Sapienza University of Rome (Prof. Rosanna Papa, Dr. Marica Trecca).

Bacterial growth experiments involving *Psychrobacter* sp.TAE2020 and *Staphylococcus epidermidis*, as well as anti-adhesive, anti-biofilm, and emulsifying assays, were conducted in collaboration with the Department of Chemical Sciences, University of Naples "Federico II" (Prof. Ermengilda Parrilli, Prof. Maria Luisa Tutino, Dr. Caterina D'Angelo, Dr. Diana Olimpo).

In vitro assays using LPS and Lipid A from *P. aeruginosa* were performed in collaboration with the Department of Experimental Medicine, University of Campania "Luigi Vanvitelli" (Prof. Chiara Schiraldi, Dr. Valentina Vassallo).

Additional structural analyses on selected *P. aeruginosa* strains were carried out in collaboration with the Laboratory of Microbial Immunochemistry and Vaccines, Ludwik Hirszfeld Institute of Immunology and Experimental Therapy, Polish Academy of Sciences (Prof. Jolanta Lukasiewicz, Prof. Marta Kaszowska, Prof. Anna Maciejewska, Prof. Wojciech Jachymek)

# *Introduction*

# Chapter I

***Surface glycans in Gram-Negative bacteria: structure, function, and roles in biofilm formation***

## 1.1 Structural and functional roles of bacterial surface glycans in biofilm formation and antimicrobial resistance

Persistent bacterial infections are predominantly associated with the presence of biofilms, defined as organized microbial communities embedded in a hydrated, self-produced extracellular polymeric substance (EPS) matrix (Costerton et al., 1999; Peters et al., 2012). These structures can develop on both biotic and abiotic surfaces and play a central role in chronic and nosocomial infections. In wound-associated infections, *Pseudomonas aeruginosa* and *Staphylococcus aureus* are among the most prevalent pathogens, with reported prevalence rates of 52.2% and 93.5%, respectively (Hauser et al., 2011) (**Fig. 1.1**).

Biofilm formation occurs through a series of well-defined stages.

i. *Reversible adhesion*: planktonic cells approach the surface through weak physical interactions, including hydrophobic forces, van der Waals bonds, and electrostatic interactions. At this stage, attachment is easily reversible.
ii. *Irreversible adhesion*: adhesion is stabilized through surface structures such as pili, fimbriae, and flagella, as well as through the initial production of adhesins and glycans.
iii. *Microcolony formation*: cells proliferate and begin to produce matrix components, while quorum sensing (QS) facilitates intercellular communication.
iv. *Maturation*: the biofilm develops a complex three-dimensional architecture with water channels that allow nutrient diffusion and waste removal. The community becomes metabolically heterogeneous, comprising both active cells and dormant persisters.
v. *Dispersion*: individual cells or clusters detach, enabling colonization of new niches. This process is often regulated by environmental signals and matrix-degrading enzymes) (Kaplan, 2010).

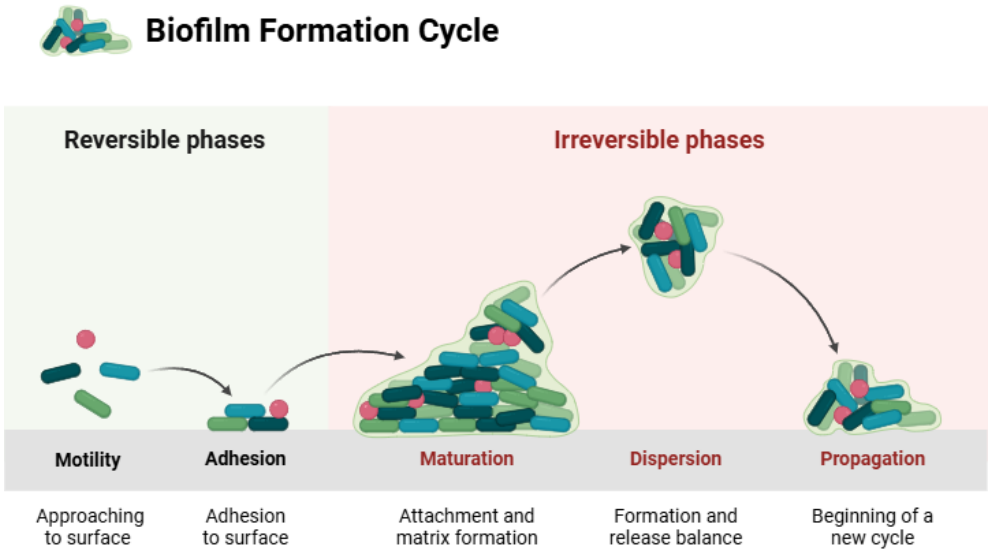


**Fig. 1.1** Biofilm formation cycle. Schematic representation of the main stages of biofilm development. The early reversible phases involve bacterial motility and initial adhesion to a surface, while the irreversible phases include biofilm maturation, dispersion of cells or clusters, and propagation to new sites, initiating a new cycle. *Created with BioRender.com.*

A key element of biofilms is the EPS matrix, which can account for up to 90% of the biofilm's dry mass and is composed of polysaccharides, proteins, extracellular DNA (eDNA), and lipids (Flemming et al., 2016). This structure, referred to as the matrixome, provides mechanical stability, promotes metabolic heterogeneity, acts as a physical barrier against antimicrobials, and facilitates immune evasion (Franklin et al., 2011; Wilton et al., 2016).

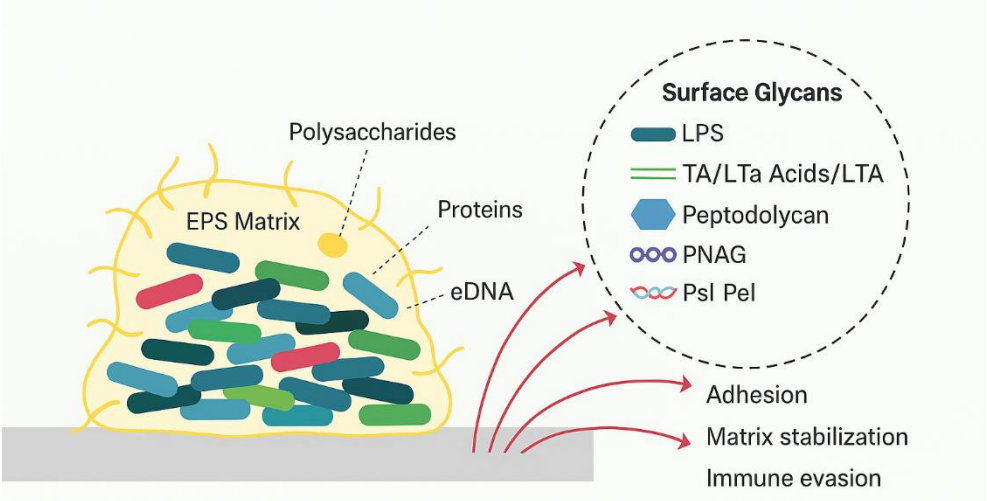


**Fig. 1.2** Schematic representation of the biofilm matrix. The EPS matrix consists of polysaccharides, proteins, eDNA, and lipids. Surface glycans (LPS, TA/LTA, peptidoglycan, PNAG, Psl/Pel) contribute to adhesion, matrix stabilization, and immune evasion. *Created with BioRender.com.*

Within this framework, surface glycans play a pivotal role (**Fig. 1.2**). In both Gram-negative and Gram-positive bacteria, they are key structural and functional components of the cell envelope. These include lipopolysaccharides (LPS) in Gram-negative species, teichoic acids (TA) and lipoteichoic acids (LTA) in Gram-positive species, peptidoglycan, and exopolysaccharides (EPS). Glycans have dual functions: they contribute to structural integrity and mechanical resistance, and they mediate critical biological processes such as surface adhesion, molecular recognition, and interactions with the host immune system (Arciola et al., 2002; Weidenmaier et al., 2004).

In Gram-negative bacteria, variations in O-antigen chain length or mutations in the LPS core can significantly influence adhesion and biofilm development (Heacock-Kang et al., 2018; Lee et al., 2007). For example, mutations in the B-band O-antigen of *P. aeruginosa* enhance biofilm formation (Makin & Beveridge, 1996), while lipid A palmitoylation in *Escherichia coli* is associated with biofilm-persistent phenotypes (Chalabaev et al., 2014). In Gram-positive bacteria, teichoic acids modulate surface charge and hydrophobicity, affecting colonization and biofilm formation on medical device surfaces (Bucher et al., 2015; Fedtke et al., 2007). Following irreversible adhesion, the secretion of exopolysaccharides - including alginates, bacterial cellulose, β-1,6-branched polysaccharides, and poly-N-acetylglucosamine (PNAG) - promotes the assembly of the mature extracellular matrix (Berk et al., 2012; Cramton et al.,

1999). Specific glycans, such as PNAG in *S. aureus* and Psl and Pel in *P. aeruginosa*, have distinct roles in intercellular adhesion, immune evasion, and matrix stabilization (Beaudoin et al., 2017; Franklin et al., 2011).
Chemical modifications of glycans, including acetylation, phosphorylation, and atypical glycosylation, modulate surface charge and hydration, influencing recognition by innate immune receptors such as Toll-like receptors (TLRs) and C-type lectins. These modifications can mask immunogenic epitopes, reduce inflammatory responses, and facilitate immune evasion and intracellular survival (Weidenmaier & Peschel, 2008). Moreover, in polymicrobial biofilms, interspecies interactions can enhance antibiotic resistance and reshape the matrix architecture. For example, extracellular products of *S. aureus* increase *P. aeruginosa* resistance to tobramycin, whereas *S. aureus* protein A inhibits Psl production in *P. aeruginosa* (Armbruster et al., 2016; Beaudoin et al., 2017).

## 1.2 Gram-negative bacteria

Gram-negative bacteria are characterized by a complex and highly organized cell envelope that plays a crucial role in their physiology and pathogenicity. Their cell wall consists of a thin peptidoglycan layer located in the periplasmic space, sandwiched between the cytoplasmic membrane and an asymmetric outer membrane. This outer membrane functions as a selective permeability barrier, contributing significantly to intrinsic resistance to a wide range of antimicrobial agents. A distinctive hallmark of Gram-negative bacteria is the presence of lipopolysaccharide (LPS), an amphipathic molecule embedded in the outer membrane and essential for bacterial survival and interaction with the host immune system (Poltorak et al., 1998)(Raetz & Whitfield, 2002).
Structurally, LPS is composed of three main domains: lipid A, the hydrophobic anchor within the outer membrane, formed by a phosphorylated glucosamine backbone with acyl chains and responsible for the molecule's endotoxic activity (Alexander & Rietschel, 2001); the core oligosaccharide, which connects lipid A to the O-antigen and contains unique sugars such as 3-deoxy-D-manno-octulosonic acid (Kdo) and heptoses; and the O-antigen, a variable polysaccharide chain exposed on the bacterial surface that contributes to immune evasion and determines serotype specificity (Whitfield & Trent, 2014) (**Fig. 1.3**). LPS is one of the most potent activators of the innate immune system through Toll-like receptor 4 (TLR4) and its co-receptor MD-2, triggering inflammatory cascades, cytokine release, and, under severe conditions, septic shock (Poltorak et al., 1998).

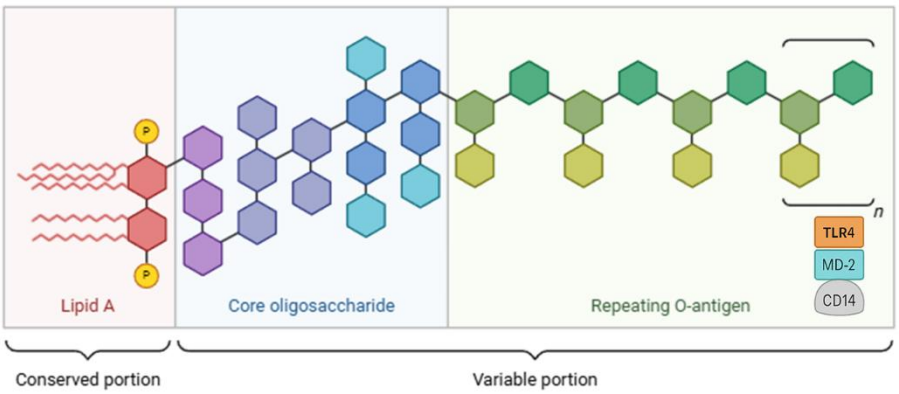


**Fig. 1.3** Structure of lipopolysaccharide (LPS) in Gram-negative bacteria. LPS consists of three main regions: Lipid A, covalently linked to the inner core through Kdo residues; the core oligosaccharide, composed of inner (conserved) and outer (variable) segments; and the O-antigen, a repeating polysaccharide responsible for antigenic variability. Lipid A serves as the membrane anchor and primary endotoxic determinant, while the core stabilizes the outer membrane and the O-antigen mediates immune evasion. *Created with BioRender.com.*

Among Gram-negative pathogens, *Pseudomonas aeruginosa* is particularly relevant due to its adaptability and clinical significance. This aerobic, motile, rod-shaped bacterium, equipped with one or more polar flagella, displays remarkable metabolic versatility. It thrives in nutrient-poor environments, tolerates oxidative stress and desiccation, and colonizes diverse ecological niches, including moist hospital surfaces and compromised host tissues (Stover et al., 2000). As an opportunistic pathogen, *P. aeruginosa* causes severe infections in immunocompromised patients and individuals with chronic respiratory diseases, particularly cystic fibrosis (CF). Its intrinsic resistance to multiple antibiotics is largely due to the low permeability of its outer membrane, the activity of multidrug efflux pumps, and the production of β-lactamases (Poole, 2011). This bacterium expresses a wide array of virulence factors, including exotoxin A, elastase, alkaline protease, secretion systems (type III and VI), pili, fimbriae, and pigments such as pyocyanin and pyoverdine, which together contribute to tissue damage, immune evasion, and persistence in the host (Hauser et al., 2011).

Cystic fibrosis is a life-limiting autosomal recessive disease caused by mutations in the gene coding for CFTR (Cystic Fibrosis Transmembrane Conductance Regulator) on chromosome 7q31.2 (Riordan et al., 1989). The most common mutation, ΔF508, leads to a defect in CFTR folding and trafficking, resulting in the loss of functional chloride channels at the apical

membrane of epithelial cells. Impaired chloride and bicarbonate secretion increases sodium and water reabsorption, producing dehydrated, viscous mucus that accumulates in the airways. This thick mucus compromises mucociliary clearance and creates a nutrient-rich environment that favors chronic bacterial colonization, particularly by *P. aeruginosa* (Ratjen, 2009). Persistent infection and inflammation progressively damage lung tissue, leading to bronchiectasis, respiratory failure, and ultimately, reduced life expectancy (Elborn et al., 2016).

Within the CF lung environment, *P. aeruginosa* undergoes profound adaptive changes that enable it to persist for years despite immune responses and aggressive antimicrobial therapies. A central element of this adaptation involves structural modifications of its LPS. During early infection, *P. aeruginosa* expresses a complete LPS with an intact O-antigen, which provides resistance to complement-mediated killing and phagocytosis. Over time, however, the bacterium shifts toward a less immunogenic phenotype through loss or reduction of the O-antigen (smooth-to-rough transition), thereby decreasing susceptibility to opsonizing antibodies (Hancock et al., 1983). In parallel, the lipid A domain is remodelled through altered acylation and phosphorylation patterns, reducing recognition by TLR4 and increasing resistance to cationic antimicrobial peptides and polymyxins (Ernst et al., 2007). Modifications to the core oligosaccharide further contribute to membrane stability and increased tolerance to antibiotics.

These molecular changes are accompanied by the bacterium's ability to form dense, structured biofilms, which are a hallmark of chronic CF infections. The biofilm matrix, composed of polysaccharides (alginate, Psl, Pel), extracellular DNA, and proteins, embeds the bacterial cells, creating a physical and chemical shield that limits antibiotic penetration and protects against neutrophil-mediated killing (Ryder et al., 2007). In mucoid strains, typically found in advanced stages of infection, excessive alginate production is driven by mutations in the *mucA* gene (Mathee et al., 1999). The combination of LPS remodelling and biofilm formation establishes a formidable barrier that hinders immune clearance and antimicrobial efficacy. Moreover, biofilm communities enable bacterial communication through quorum-sensing systems, which coordinate the expression of virulence and adaptation genes (Bjarnsholt et al., 2009). This dual strategy plays a pivotal role in the transition from acute to chronic infection and is a major factor underlying the persistence of *P. aeruginosa* in CF lungs (**Fig. 1.4**).

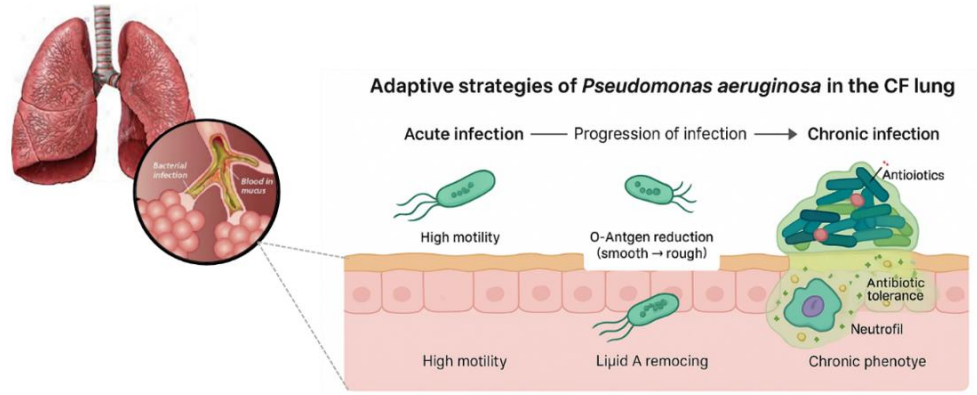


**Fig. 1.4** Adaptive strategies of *P. aeruginosa* in CF airways. Over time, the bacterium transitions from a motile, planktonic state to a biofilm-associated mucoid phenotype. LPS remodelling (O-antigen loss, lipid A modification), quorum sensing, and alginate overproduction contribute to immune evasion, antibiotic tolerance, and persistent infection in the CF lung. *Created with BioRender.com.*

LPS plays a central role in activating innate immune responses through interaction with the TLR4/MD-2/CD14 receptor complex expressed on airway epithelial cells, alveolar macrophages, and neutrophils. This recognition event triggers MyD88- and TRIF-dependent signalling pathways, leading to the activation of NF-κB and IRF transcription factors and the subsequent production of pro-inflammatory mediators, including TNF-α, IL-1β, IL-6, IL-8, and type I interferons (Beutler, 2000; Poltorak et al., 1998). Among these, IL-8 is particularly important as it drives neutrophil recruitment into the airways (**Fig. 1.5**).

In the context of chronic infection, persistent TLR4 stimulation, even if attenuated by LPS modifications, induces a sustained, low-grade inflammatory response that fails to eliminate the pathogen. Recruited neutrophils release proteolytic enzymes such as neutrophil elastase and cathepsin G, as well as reactive oxygen species, which are ineffective against biofilm-protected bacteria but cause significant collateral tissue damage. In addition, the formation of neutrophil extracellular traps (NETs) further increases mucus viscosity and contributes to airway obstruction. The biofilm matrix amplifies this process by shielding bacteria from phagocytosis, prolonging antigenic stimulation, and dampening adaptive immune responses. Over time, this persistent and dysregulated inflammatory state leads to progressive destruction of lung tissue and decline in pulmonary function, a hallmark of CF lung disease (Chmiel et al., 2002).

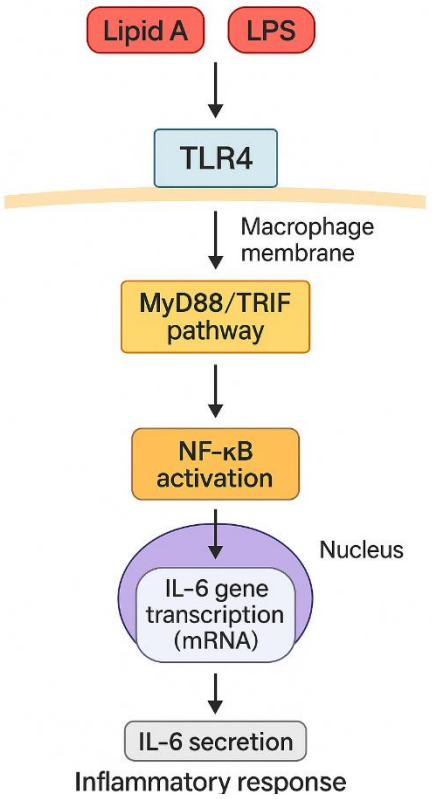


**Fig. 1.5** TLR4-mediated signalling induced by LPS. Lipid A, the bioactive component of LPS, binds to the TLR4 receptor complex, triggering NF-κB activation and the transcription of pro-inflammatory genes such as IL-6. The resulting IL-6 mRNA is translated and secreted, contributing to the inflammatory response.

# Chapter II

## *Cold-adapted bacteria as a source of novel antibiofilm strategies*

### 2.1 Polysaccharides in cold adaptation: microbial strategies in extreme environments

Psychrophilic microorganisms, whose name derives from the Greek *psychrós* (cold) and *philos* (loving), represent a fascinating example of life thriving under extremely low temperatures. These organisms grow with a minimum temperature equal to or below 0 °C, an optimum around 15 °C, and a maximum not exceeding 20 °C. They are typically found in polar regions such as the Arctic and Antarctica, but also in deep-sea environments, glaciers, and permafrost, where temperatures remain constantly low. Their presence demonstrates that cold is not an insurmountable barrier to life, but rather a selective context that has driven the evolution of extraordinary physiological and molecular strategies. These adaptations are not limited to bacteria but also involve archaea, algae, yeasts, insects, fish, and plants.

Polar and deep-sea ecosystems are particularly hostile, imposing severe selective pressures on microbial life. Low temperatures reduce membrane fluidity, increase water viscosity, and slow down solute diffusion; enzymes tend to become rigid, losing catalytic efficiency, while transmembrane transport processes are impaired. Additional factors, such as nutrient scarcity, salinity fluctuations, and ultraviolet radiation, further contribute to making these environments a constant challenge for microbial survival (De Maayer et al., 2014).

To overcome these limitations, psychrophilic microorganisms have developed a range of physiological and molecular adaptations. Their cell membranes contain higher proportions of unsaturated and branched fatty acids, which maintain membrane fluidity near freezing temperatures. Among these lipid-based mechanisms, an important adaptation is the conversion of fatty acids from the trans to the cis isomeric form, a change that increases chain flexibility and prevents tight packing of the membrane. Psychrophiles further refine membrane properties by adjusting lipid class composition and by modifying the size or charge of lipid headgroups, thereby ensuring adequate fluidity and functionality at low temperatures.

“Cold-active” enzymes exhibit structural flexibility that allows them to retain catalytic function at low temperatures, albeit often at the expense of thermal stability. Cold-shock proteins stabilize nucleic acids and support transcription and translation processes. Many psychrophiles also accumulate cryoprotective compounds such as sugars and glycerol, which reduce freezing-induced

damage. At the genomic level, modifications occur in genes associated with low-temperature metabolism and stress responses, revealing that cold adaptation involves the entire cellular organization (**Fig. 2.1**).

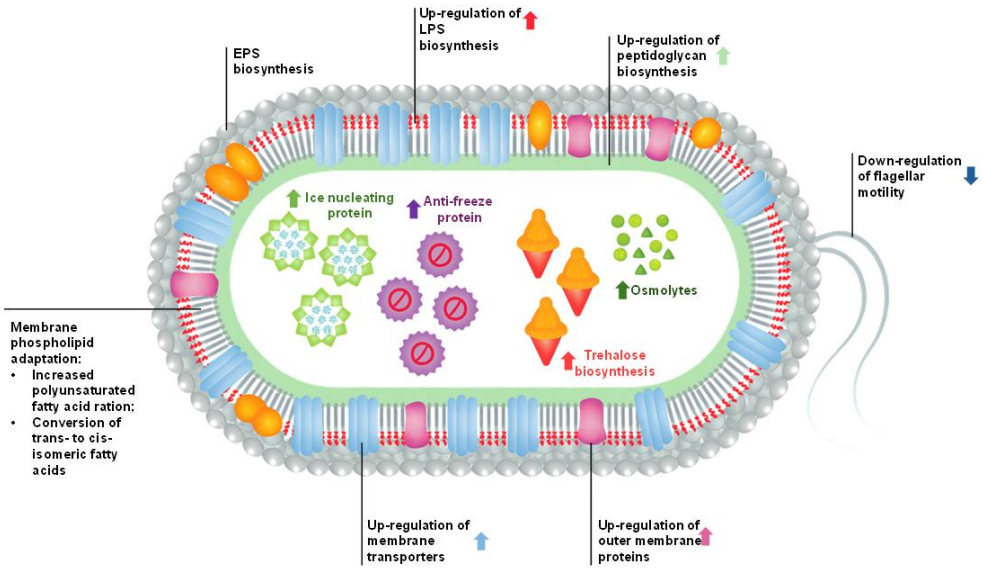


**Fig. 2.1** Schematic representation of a psychrophilic bacterium and its main cold adaptation mechanisms. *Created with BioRender.com*

Among the most significant adaptive strategies is the production of extracellular polysaccharides (EPS). These molecules can occur as capsular polysaccharides (CPS), tightly associated with the cell membrane, or as medium-released polysaccharides (MRP) (**Fig. 2.2**), often incorporated into biofilm matrices (Casillo et al., 2018). EPS play key roles by promoting surface adhesion, regulating nutrient uptake and diffusion, protecting the cell from physical and chemical stress, and sequestering environmental cations. Antarctic marine bacteria are known to produce large amounts of EPS, which modulate the physicochemical properties of their microenvironment and enhance survival under extreme conditions (Nichols et al., 2005).

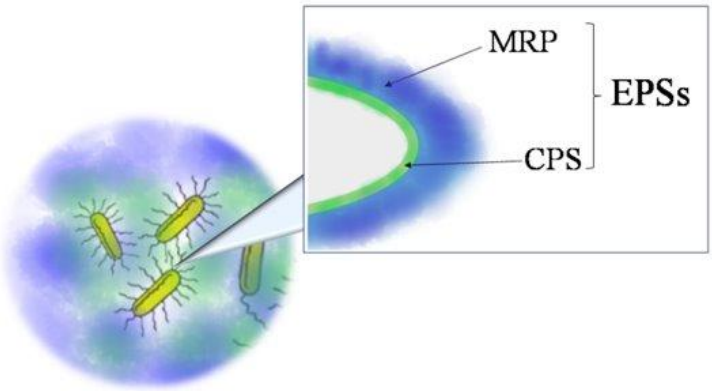


**Fig. 2.2** Representation of extracellular polysaccharides (EPSs) produced by psychrophilic bacteria. The capsule closely associated with the cell surface corresponds to capsular polysaccharides (CPS), while the matrix released into the surrounding environment corresponds to matrix-released polysaccharides (MRP). Adapted from Casillo et al. (2018), Marine Drugs 16(2):69, distributed under the terms of the Creative Commons Attribution (CC BY) license.

These adaptive traits not only ensure survival but also provide psychrophilic microorganisms with a repertoire of biologically relevant functions. They can resist environmental stress, colonize surfaces, form stable biofilms, and interact with other microorganisms through the production of extracellular molecules with protective and competitive functions. Their ability to modulate their microenvironment makes them key ecological players and mediators of microbial life in cold ecosystems.
A particularly interesting microbial group is the genus *Psychrobacter*, belonging to the family *Moraxellaceae* and the γ-proteobacteria. These are aerobic, Gram-negative, non-sporulating microorganisms, generally catalase- and oxidase-positive, widely distributed in cold habitats including polar regions, deep-sea environments, and permafrost (Madigan et al., 2017). Their ability to colonize oligotrophic and cold environments derives from physiological and molecular adaptations that enable growth under extreme conditions, often coupled with the production of functional extracellular substances (De Maayer et al., 2014; Deming et al., 2017).

Within this genus, *Psychrobacter* sp. TAE2020 represents a particularly noteworthy strain due to its biological and biotechnological potential. It was isolated from a coastal seawater sample collected near the French Dumont d'Urville Station in Terre Adélie, Antarctica (Riccardi et al., 2022). This environment, characterized by stable low temperatures and limited nutrient availability, provides an ideal setting for the selection of microorganisms with

specific adaptive strategies. *Psychrobacter* sp. TAE2020 is notable for its ability to grow at low temperatures under aerobic conditions and to produce a wide variety of extracellular substances that are important both for its own survival and for interactions with other microorganisms (D'Amico et al., 2025; D'Angelo et al., 2022).

Genomic analysis of this strain, performed through Illumina HiSeq 2500 sequencing, revealed a genome of approximately 3.29 Mbp with a GC content of 41.7%, distributed over 33 contigs (Riccardi et al., 2022). Phylogenetic analysis showed a close relationship with *Psychrobacter urativorans* and *Psychrobacter frigidicola*, members of a clade typically associated with cold marine environments. Bioinformatic analysis identified several biosynthetic gene clusters potentially involved in the production of capsular polysaccharides, surfactants, emulsifiers, and other extracellular molecules. These genomic findings were confirmed by phenotypic evidence: the strain produces surface-active molecules that lower medium surface tension and exhibits high emulsifying activity, with an emulsification index ($E_{24}$) of 70% (Riccardi et al., 2022).

One of the most remarkable features of *Psychrobacter* sp. TAE2020 is its production of extracellular molecules. This strain synthesizes natural surfactants and bioemulsifiers that remain active and stable over a wide range of pH and temperatures, providing physiological versatility. It also produces extracellular vesicles that play a role in microbial interactions and the release of bioactive compounds. A particularly distinctive product is CATASAN, a protein–polysaccharide complex composed of a polysaccharide, a lipopolysaccharide, and an outer membrane protein named PsyOmp38 (D'Amico et al., 2025; D'Angelo et al., 2022).

Beyond its protective role against environmental stressors, CATASAN exhibits significant biological activities, including anti-adhesive and anti-biofilm properties against *Staphylococcus epidermidis*, an opportunistic microorganism known to colonize medical devices and cause chronic infections. CATASAN interferes with the initial stages of cell adhesion, prevents biofilm formation, and destabilizes mature biofilm matrices. It also displays strong emulsifying activity, underscoring its multifunctional role in the physiology of *Psychrobacter* sp. TAE2020. Molecules such as CATASAN exemplify how Antarctic microorganisms integrate environmental adaptation with broader biological functions, offering promising perspectives for biotechnological and biomedical applications.

## 2.2 Multifunctional extracellular molecules as adaptive strategies in *Psychrobacter* sp. TAE2020

Biofilms represent one of the primary microbial survival strategies, allowing microorganisms to persist in unfavourable environments and acquire increased tolerance to antimicrobial agents. Although this mode of growth is advantageous ecologically, it constitutes a major medical challenge since more than 80% of chronic microbial infections are associated with biofilm formation, which provides high resistance to antibiotics and host immune defenses (Costerton et al., 1999). *Staphylococcus epidermidis*, a common commensal of the skin and mucosa, is particularly relevant as it is the most frequent cause of device-associated infections, including those involving intravascular catheters, prosthetic joints, and heart valves (Vuong et al., 2003). Its ability to adhere to abiotic surfaces and form persistent biofilms represents its major virulence factor, complicating treatment and often necessitating the removal of the infected device. This clinical impact has spurred the search for alternative strategies capable of interfering with adhesion processes and biofilm development.

Among the most promising sources of novel antibiofilm and antiadhesive compounds are microorganisms adapted to extreme environments. In cold and oligotrophic ecosystems such as Antarctica, the ability to produce molecules that modulate surface interactions may provide a competitive ecological advantage (Deming et al., 2017). *Psychrobacter* sp. TAE2020, an Antarctic marine strain, has emerged as a notable producer of extracellular polymeric substances with multifaceted activities. One of its most studied products, the protein-polysaccharide complex CATASAN, has been shown to interfere with different stages of *S. epidermidis* biofilm development, from initial adhesion to matrix destabilization, thereby preventing the establishment of mature and persistent structures (D'Angelo et al., 2022). Beyond its antibiofilm properties, CATASAN also exhibits pronounced antiadhesive activity, which can be interpreted as an ecological strategy: by inhibiting competitor colonization on surfaces, *Psychrobacter* sp. TAE2020 increases its own survival potential and access to limited resources (Decho & Gutierrez, 2017; Nichols et al., 2005).
In addition to its role in modulating microbial interactions, *Psychrobacter* sp. TAE2020 produces molecules with surfactant and emulsifying activity. Surfactants, whether synthetic or biological, are amphipathic molecules capable of reducing surface and interfacial tension between immiscible phases such as water and oil, a property essential in many physicochemical processes (Mukherjee et al., 2006; Tripathi et al., 2018). In cold environments, biosurfactants facilitate the utilization of poorly soluble hydrophobic

substrates and regulate microbial adhesion and detachment in response to changing conditions. They may also play a role in competitive interactions between microbial species, as observed for molecules such as Emulsan from *Acinetobacter venetianus* and biosurfactants from marine spp. *Pseudomonas*, *Marinomonas* and *Halomonas* (Dams-Kozlowska et al., 2008; Perfumo et al., 2018).

Experimental studies on *Psychrobacter* sp. TAE2020 revealed a strong capacity to reduce surface tension in the culture medium and to form stable emulsions, with an emulsification index ($E_{24}$) reaching ~70% (Riccardi et al., 2022). Genomic analyses identified several biosynthetic gene clusters potentially involved in biosurfactant and extracellular polysaccharide production, some of which share similarities with known systems such as those responsible for Emulsan and surfactin synthesis, suggesting the presence of structurally novel molecules (Riccardi et al., 2022). Particularly striking is the stability of the emulsifying activity of CATASAN, which remains effective across a broad range of pH and temperature values and maintains long-term emulsion stability, mirroring the environmental adaptability of the producing strain (Dams-Kozlowska et al., 2008; D'Angelo et al., 2022).

These observations highlight the multifunctional nature of extracellular macromolecular complexes in Antarctic microorganisms. In *Psychrobacter* sp. TAE2020, CATASAN, a protein-LPS-polysaccharide complex, integrates antiadhesive, antibiofilm, and surfactant properties, contributing simultaneously to ecological competitiveness and offering promising perspectives for biomedical and biotechnological applications. Altogether, the multifunctional properties of CATASAN underscore the ecological versatility of Antarctic microorganisms and their potential as a source of novel bioactive compounds.

## 2.3 Extracellular vesicles from Antarctic bacteria and perspectives in drug delivery

Extracellular vesicles (EVs) are subcellular membranous structures spontaneously released by numerous microorganisms, including both Gram-negative and Gram-positive species. They typically originate from outer membrane budding and consist of a lipid bilayer that encloses proteins, nucleic acids, polysaccharides, lipopolysaccharides or lipoproteins, and secondary metabolites (Casillo et al., 2024; Kulp & Kuehn, 2010; Schwechheimer & Kuehn, 2015) (**Fig. 2.3**).

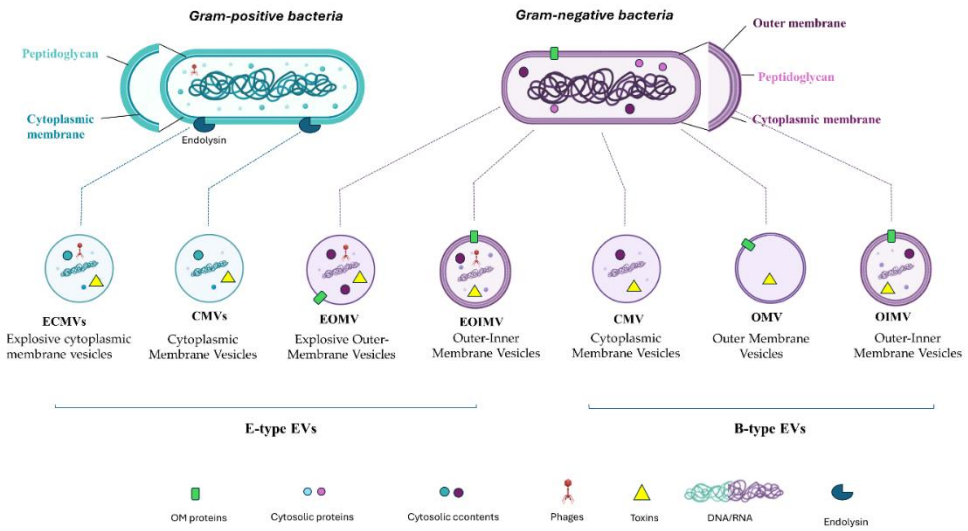


**Fig. 2.3** Biogenesis of bacterial extracellular vesicles. EVs can be produced through two different mechanisms: explosive cell lysis (E-type) and outer membrane blebbing (B-type). Gram-positive bacteria produce ECMVs and CMVs, while Gram-negative bacteria produce both B-type EVs (OMVs and OIMVs) and E-type EVs (EOMVs, CMVs, and EOIMVs). Adapted from Casillo et al. (2024), Marine Drugs 22(8):363, distributed under the terms of the Creative Commons Attribution (CC BY) license.

EVs perform complex biological functions, ranging from intercellular communication and immune modulation to the transport of enzymes and other bioactive molecules (Casillo et al., 2024). Ecologically, EVs represent versatile molecular systems that enable microorganisms to adapt to changing and unfavorable conditions. They mediate signal and nutrient exchange, promote surface adhesion, and play key roles in biofilm formation, stability, and dispersal. In marine environments characterized by extreme physical and chemical conditions, such as low temperature, high hydrostatic pressure, and nutrient scarcity, EVs support survival strategies, enhancing microbial interactions and ecological fitness (Casillo et al., 2024).

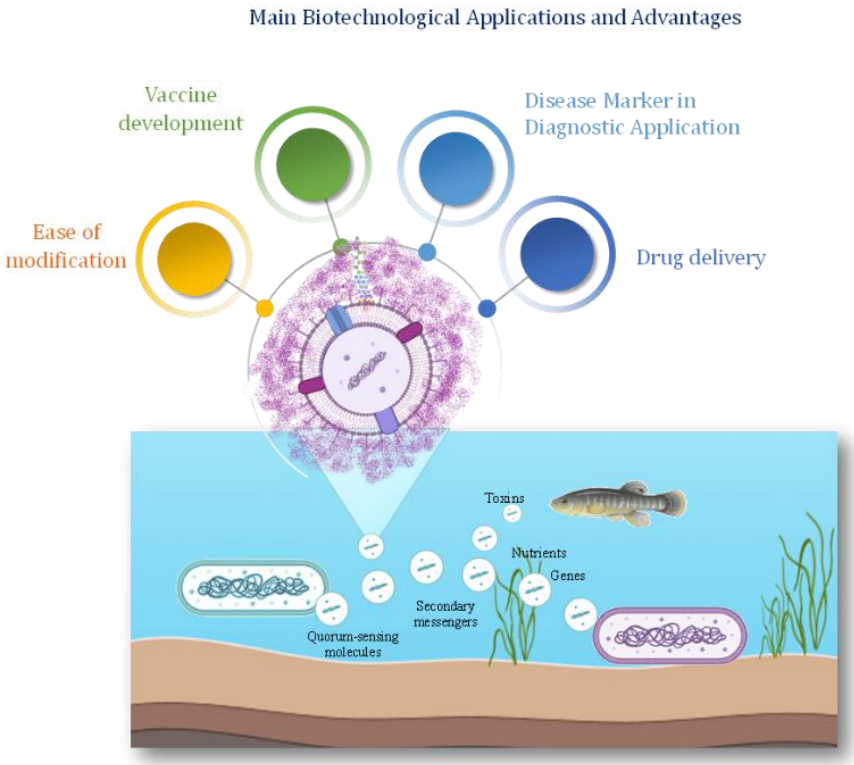


**Fig. 2.4** Roles of BEVs in marine ecosystems and their possible applications. Marine BEVs have been involved in cell-cell communication, including host-virus interactions, genes and toxins transfer, nutrient transport, and biofilm formation. The natural ability to deliver cargo molecules makes the BEVs a useful drug delivery system. Adapted from Casillo et al. (2024), Marine Drugs 22(8):363, distributed under the terms of the Creative Commons Attribution (CC BY) license.

Of particular interest are the vesicles produced by Antarctic marine bacteria, which display specific structural and biochemical features adapted to low temperatures. Their membranes are enriched in unsaturated fatty acids, which confer high fluidity and stability even under cryogenic conditions (De Maayer et al., 2014). These adaptations extend to the EVs themselves, enabling them to maintain their structural integrity and biological activity in harsh environments, making them particularly well-suited for the transport of bioactive molecules (Casillo et al., 2024). Beyond their ecological significance, EVs from Antarctic marine bacteria hold strong potential for biomedical and biotechnological applications. Their natural nanostructure provides clear advantages over synthetic delivery systems, including biocompatibility, biodegradability, the ability to cross biological barriers, and

protection of their molecular cargo from degradation. EVs derived from non-pathogenic Antarctic strains combine microbiological safety with intrinsic stability under extreme conditions, making them promising candidates as natural nanocarriers for drug, enzyme, and bioactive molecule delivery. An additional relevant aspect concerns the structural complexity of the EV surface components, including lipopolysaccharides (LPS) and capsular polysaccharides (CPS), which can significantly influence vesicle stability, biological interactions, and immune responses. Detailed structural studies, such as those performed on EVs from *Shewanella vesiculosa* HM13 (Di Guida et al., 2020), have demonstrated how these macromolecules contribute to the physicochemical properties and functional behaviour of marine EVs, providing important insights for both ecological interpretation and potential technological exploitation.

Another promising application is the control of biofilm-associated infections, which are typically resistant to conventional antimicrobial therapies. The diffusion of drug-resistant pathogens, leading to antimicrobial resistance (AMR), makes bacterial-associated infections increasingly difficult to eradicate. Conventional antibiotics often prove ineffective, highlighting the urgent need to identify novel therapeutic strategies. One of the main causes of treatment failure is biofilm formation, which confers protection to microbial communities and limits antibiotic penetration (Stewart, 2015). Among the most promising alternatives, the use of nanoparticles (NPs) for drug delivery has been extensively investigated. Liposomal drug carriers have gained considerable attention due to their biocompatibility, biodegradability, and low toxicity. However, when released into the bloodstream, liposomes are immediately exposed to high protein concentrations, leading to the formation of a protein corona on their surface. This phenomenon alters their physicochemical properties, confers a new “biological identity,” and can compromise their targeting efficiency. To overcome these limitations, polysaccharides represent a promising class of natural polymers for surface modification of liposomes. Their incorporation can enhance stability, reduce clearance, and improve biocompatibility. Coating liposomes with biopolymers modulates surface charge, membrane fluidity, and particle size, thereby extending their circulation time and improving drug delivery performance (Karn et al., 2011). Moreover, the intrinsic mucoadhesive properties of polysaccharides increase drug residence time at target sites. Recent studies have demonstrated the ability of capsular polysaccharides (CPS) to adhere both to inorganic surfaces, such as polystyrene, and to organic structures, such as liposomal membranes. This has been shown for a cold-adapted *Shewanella* strain (Casillo et al., 2022). A novel and complementary strategy for combating

antimicrobial resistance exploits the natural vesiculation capacity of bacteria. Extracellular membrane vesicles (EMVs) serve as effective carriers of bioactive compounds, including antimicrobial and antibiofilm agents, owing to their intrinsic ability to encapsulate diverse cargo molecules and their high mobility within the extracellular milieu (Casillo et al., 2024). Understanding the molecular composition and structural properties of EMVs, particularly their surface glycoconjugates, is essential for elucidating their interactions in complex biological environments. Such insights will facilitate the design of EV-based delivery platforms and experimental systems to investigate the mechanisms of action of antimicrobial drugs.

## Objectives of the study

***Chapter III***

The present work focused on the analysis of surface glycans and extracellular polysaccharides from *Pseudomonas aeruginosa*, an opportunistic pathogen responsible for respiratory tract colonization in patients with cystic fibrosis (CF).

Different bacterial strains were analyzed:

- **i.** two wild-type strains sensitive to clinically used antibiotics (WT2 and WT4), isolated during early colonization (<12 months);
- **ii.** two multidrug-resistant strains (MDR1 and MDR5);
- **iii.** two pandrug-resistant strains (PDR5 and PDR7), isolated during chronic colonization (4–15 years).

In CF-associated chronic respiratory infections, continuous antibiotic administration aims to stabilize the clinical condition. However, the selective pressure exerted by long-term antimicrobial therapy promotes adaptive mechanisms leading to drug resistance and reduced treatment efficacy. In parallel, *P. aeruginosa* progressively develops a mucoid phenotype associated with structural modifications of surface glycans, particularly lipopolysaccharides (LPS), and with a marked ability to form biofilms. Biofilms act as protective matrices that hinder antibiotic penetration, regulate nutrient availability, and reduce the effectiveness of innate and adaptive immune responses. In this scenario, glycans play a central role in antibiotic resistance and in the modulation of host-pathogen interactions.

The objectives of this study were to:

- **i.** characterize the structural modifications of glycans and lipoglycans in strains with different levels of antibiotic resistance;
- **ii.** identify glycans present in the biofilm matrix;
- **iii.** evaluate their role in modulating host immune and inflammatory responses.

To address these aims, the research was conducted in two experimental sections. In the first phase of the study, strains PA14, WT4 and PDR7 were analyzed in detail to characterize their glycans. Subsequently, during my research stay at the Hirszfeld Institute of Immunology and Experimental Therapy in Wrocław (Poland), it became possible to extend the analysis to additional clinical strains (WT2, MDR1, MDR5 and PDR5). These strains

were extracted using slightly different procedures and investigated with advanced HR-MAS NMR spectroscopy, allowing direct analysis of glycans in semi-solid preparations. This methodological difference justifies the division of the strains into two dedicated analytical sections within the thesis.
To achieve the overall goals, advanced nuclear magnetic resonance (NMR) spectroscopy and mass spectrometry were employed, supported by physicochemical analyses. Biological assays were also performed to assess immune activation and inflammatory responses induced by the isolated glycans. In cystic fibrosis, chronic airway inflammation triggered by persistent infection leads to progressive remodelling of lung parenchyma and ultimately to irreversible fibrosis, severely impairing respiratory function. Therefore, the study of *P. aeruginosa* glycans provides essential insights into their contribution to antimicrobial resistance and to the pathogenic mechanisms that sustain chronic infection in CF.

***Chapter IV***
In parallel with the investigation of pathogenic bacteria such as *P. aeruginosa*, the work also explored extremophilic microorganisms as alternative models and potential sources of bioactive molecules. In particular, the study focused on Antarctic bacteria, which represented an inexhaustible source of molecules with remarkable biological activities, often related to their unusual structural features.
Attention was directed to the species *Psychrobacter* sp. TAE2020, already known for producing molecules with antibiofilm, antiadhesive, and surfactant activities, as well as for its ability to release extracellular vesicles. The objective was to analyze surface glycans and evaluate their biological activity, with the goal of establishing a structure-function relationship. To this end, NMR spectroscopy, mass spectrometry, and complementary physicochemical techniques were applied to characterize glycans located on the bacterial cell surface. These data were also instrumental in elucidating the glycans associated with vesicles, which were derived from the bacterial cell envelope.
In conclusion, the analysis of *Psychrobacter* sp. TAE2020 surface glycans not only provided a deeper understanding of the molecular strategies underlying cold adaptation but also opened new perspectives for the development of innovative vesicle-based biotechnological applications.

# *Results*

# Chapter III

## *Analysis of glycans from clinical Pseudomonas aeruginosa isolates*

### 3.1 LPS isolation from *P. aeruginosa* PA14, WT4, and PDR7 grown under planktonic conditions and as biofilm communities

Dried cells obtained by planktonic growth (P) of PA14 (reference strain), WT4 (wild-type (WT) strain sensitive to all tested antibiotics), and PDR7 (pan-drug-resistant (PDR) strain from a patient with chronic colonization) were extracted by the hot phenol/water method (Westphal, 1965). The same procedure was applied to the strains that were grown as biofilm communities (B) (B.PA14, B.WT4, and B.PDR7). The extracted LPSs were purified to remove phospholipids, proteins and nucleic acids, dialyzed, and freeze-dried. The amount of LPS (yield, %) obtained for each sample is reported in **Table 3.1**.

**Table 3.1** Biomass of extracted cells (mg) and LPS yield of the analyzed strains. LPS yield is expressed as the percentage ratio of purified LPS (mg) relative to bacterial biomass (mg).

| | PLANKTONIC (P.) | BIOFILM (S.) | PLANKTONIC (P.) | BIOFILM (B.) |
|---|---|---|---|---|
| | Biomass (mg) | | LPS yield (%) | |
| PA14 | 516 | 234 | 1.2% | 3.9% |
| WT4 | 256 | 85 | 3.1% | 2.5% |
| PDR7 | 265 | 125 | 1.7% | 2.4% |

All extracts were analyzed by 14% DOC-PAGE followed by silver staining (**Fig. 3.1**). Purified *E. coli* lipopolysaccharide (LPS) was used as a smooth-type reference standard. Silver-stained gel revealed the production of a smooth LPS for strains PA14 and WT4. In contrast, the PDR7 strain produced an LPS

lacking the O-chain under both planktonic and biofilm growth conditions.

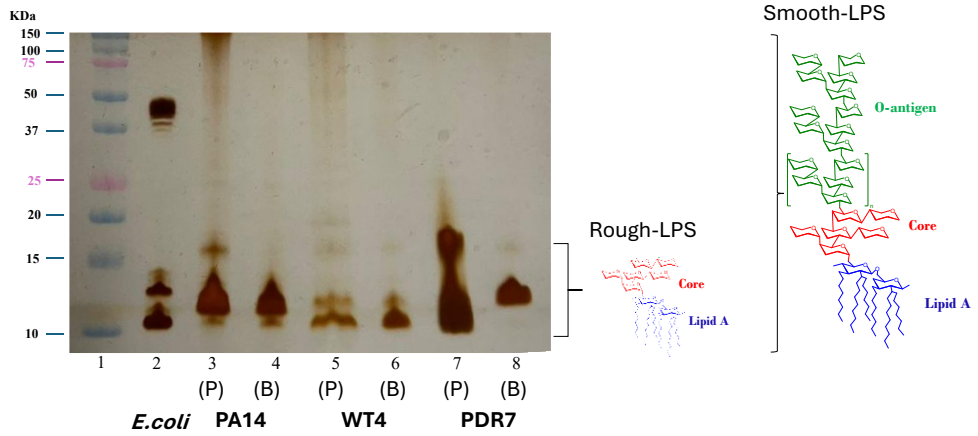


**Fig. 3.1** Electrophoretic profile of lipopolysaccharides (LPSs) analyzed by 14 % DOC-PAGE and silver staining. "P" and "B" referred to planktonic and biofilm growth conditions, respectively. Lane 1: Precision Plus protein standards; Lane 2: LPS from *E. coli* O55:B5 used as a standard to identify smooth-type LPS; Lane 3: LPS from PA14 strain grown under planktonic conditions; Lane 4: LPS from PA14 strain grown as biofilm structured communities; Lane 5: LPS from WT4 strain grown under planktonic conditions; Lane 6: LPS from WT4 strain grown as structured biofilm communities; Lane 7: LPS from PDR7 strain grown under planktonic conditions; Lane 8: LPS from PDR7 strain grown as structured biofilm communities. The differences in the banding patterns reflect variations in LPS between strains and growth conditions. The amount of loaded LPSs was 8 µg for each sample.

## 3.2 LPS glycosyl analysis

The sugar composition of each LPS was obtained after derivatization as acetylated methyl glycosides (AMGs) and achieved by gas chromatography-mass spectrometry (GC-MS).

The chromatograms showed the presence of rhamnose (Rha), glucose (Glc), mannose (Man), glucosamine (GlcN), and 2-keto-3-deoxy-manno-octulosonic acid (Kdo) in all the obtained extracts. In addition, the occurrence of 2-amino-2-deoxy-galacturonic acid (GalNA) and 2-amino-2,6-dideoxy-glucose (quinovosamine, QuiN) in the LPS of *P. aeruginosa* PA14 strain grown under planktonic (P.PA14) and in biofilm conditions (B.PA14) was detected (**Fig. 3.2**).

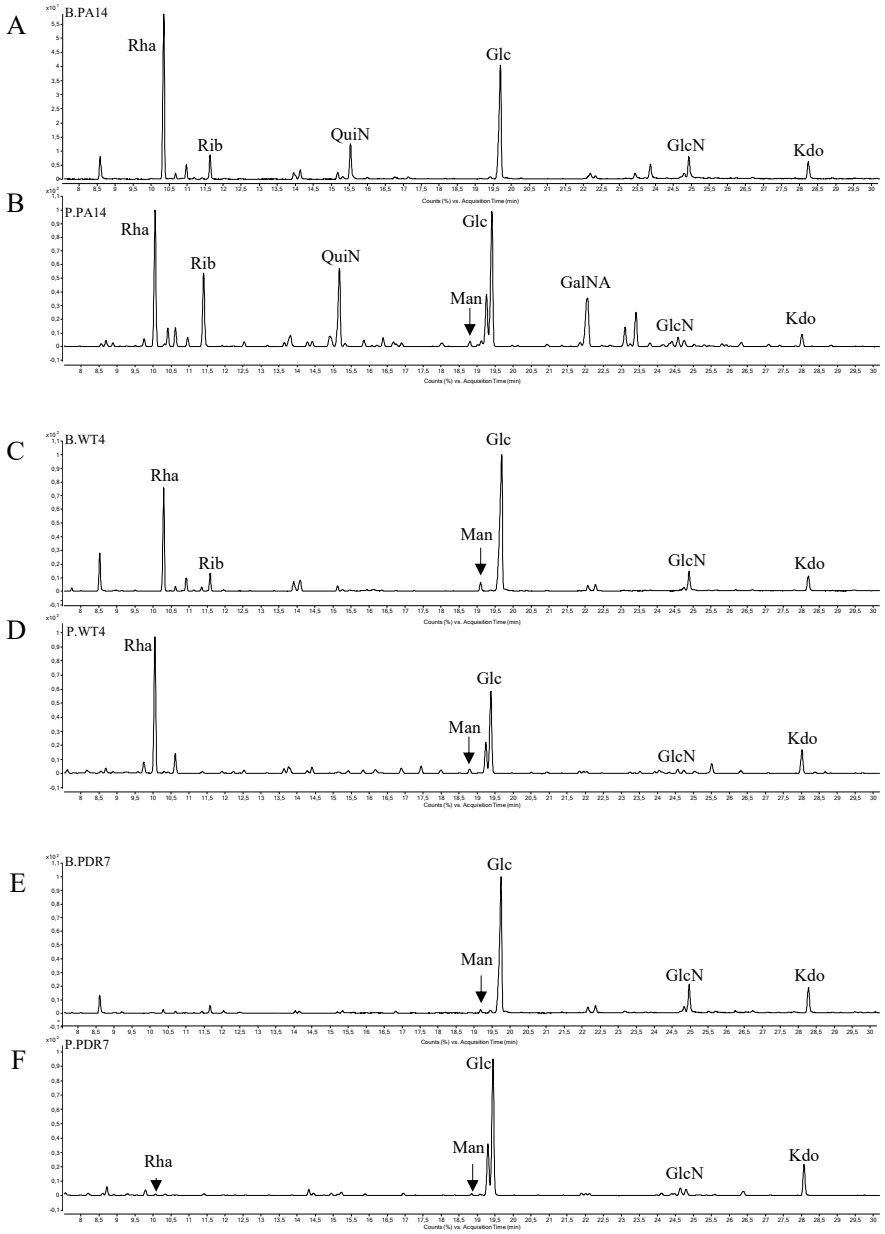


**Fig. 3.2** GC-MS chromatograms of AMGs from *P. aeruginosa* strains grown in biofilm and planktonic conditions. A) PA14 grown in biofilm condition (B.PA14); B) PA14 grown under planktonic conditions (P.PA14); C) WT4 grown in biofilm condition (B.WT4); D) WT4 grown under planktonic conditions (WT4); E) PDR7 grown in biofilm condition (B.PDR7); F) PDR7 grown under planktonic conditions (P.PDR7).

### 3.3 Lipid A isolation and compositional analysis

LPSs were subjected to mild acid hydrolysis with 1% acetic acid to purify the lipid A portion. Lipid A samples were derivatized as AMG and analyzed by GC-MS. The chromatogram indicated glucosamine as the only monosaccharide constituent of the glycolipid, thus confirming the absence of arabinosamine, as reported for another Lipid A of the genus *Pseudomonas* (Ernst et al., 2007).

The total fatty acid composition was obtained by analyzing the Lipid A by GC-MS after derivatization into their methyl ester derivatives (FAMEs). The fatty acids analysis mainly indicated 3-hydroxy-decanoic acid [C10:0(3OH)], 2-hydroxy-dodecanoic acid [C12:0(2-OH)] and 3-hydroxy-dodecanoic acid [C12:0(3-OH)] as hydroxylated species. The analysis also revealed the occurrence of dodecanoic acid (C12:0), and hexadecanoic acid (C16:0) (**Fig. 3.3**).

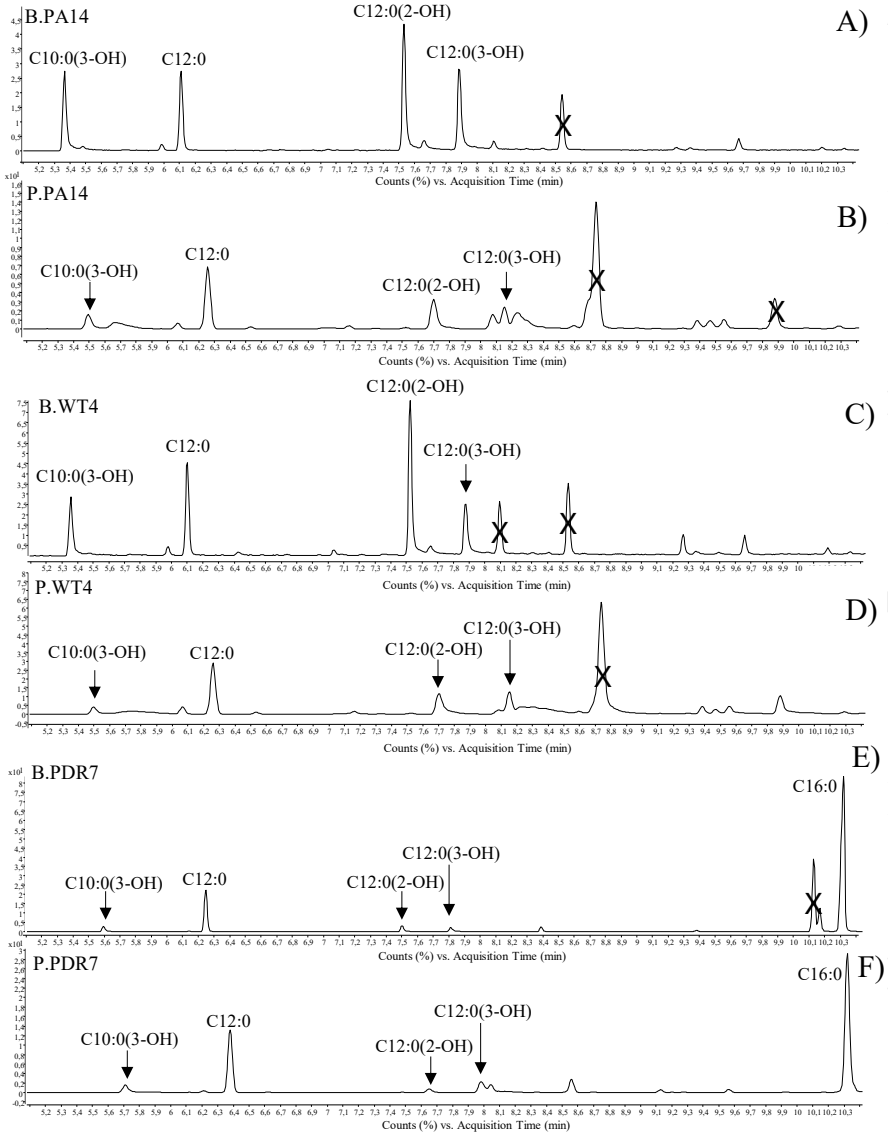


**Fig. 3.3** GC-MS chromatograms of FAMEs from *P. aeruginosa* strains grown in biofilm and planktonic conditions. A) PA14 grown in biofilm condition (B.PA14); B) PA14 grown under planktonic conditions (P.PA14); C) WT4 grown in biofilm condition (B.WT4); D) WT4 grown under planktonic conditions (WT4); E) PDR7 grown in biofilm condition (B.PDR7); F) PDR7 grown under planktonic conditions (P.PDR7). The X marks in the chromatograms indicate peaks corresponding to impurities

### 3.4 Mass spectrometry analysis

Reflectron MALDI-TOF spectra recorded in the negative ion mode revealed variations in Lipid A structures, both for the same strain grown under planktonic conditions and as biofilm communities (P.PA14-B.PA14), (P.WT4-B.WT4), (P.PDR7-B.PDR7), as well as differences ranging from antibiotic-sensitive to antibiotic-resistant strains.

MALDI-TOF spectrum of Lipid A from P.PA14 revealed the presence of glycoforms ranging from tetra-acylated to hexa-acylated (**M1**-**M6**), differing in their acylation and phosphorylation degree (**Fig. 3.4**).

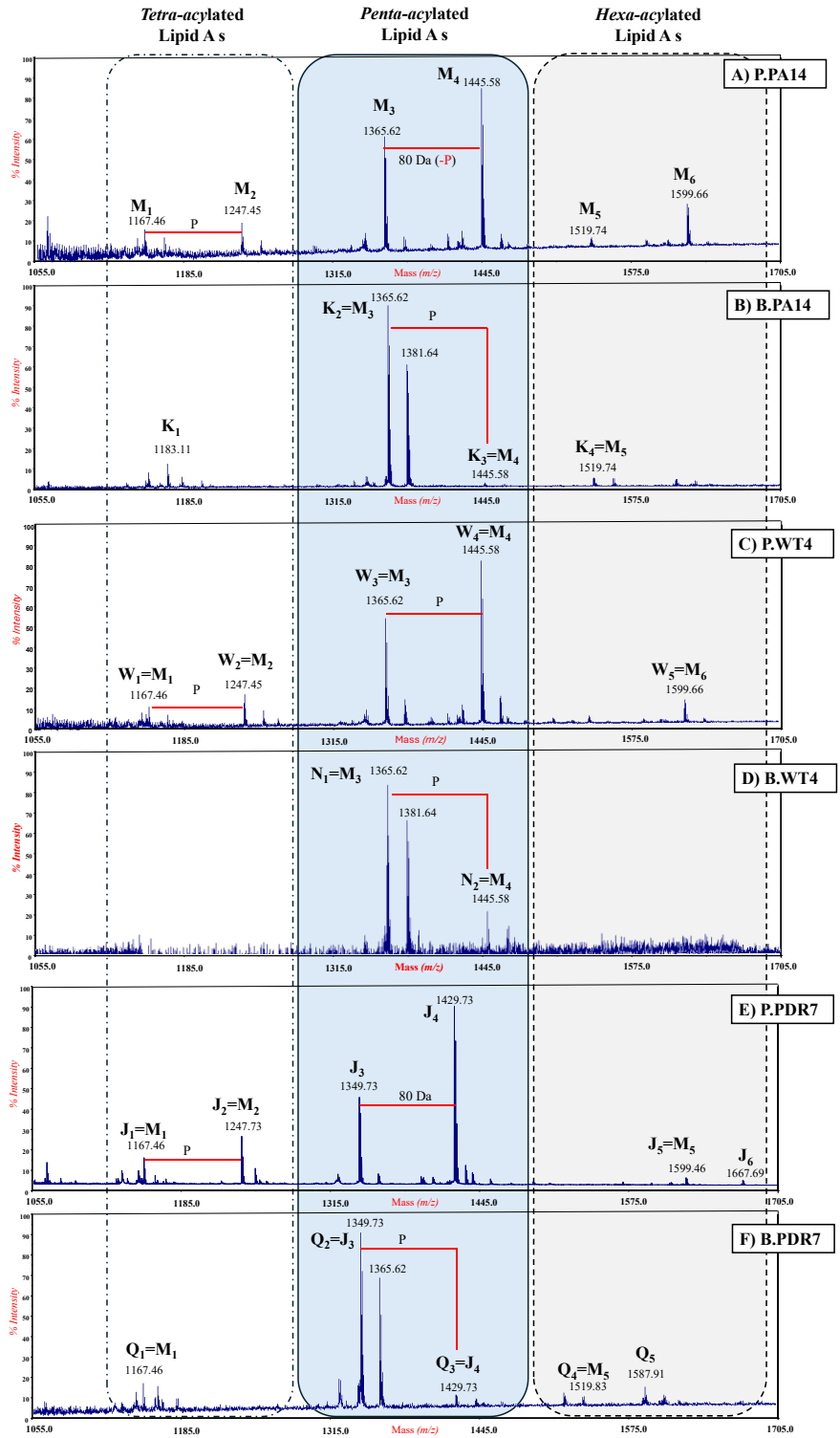
Tetra-acylated Lipid A s
Penta-acylated Lipid A s
Hexa-acylated Lipid A s
A) P.PA14
M1 1167.46
P
M2 1247.45
M3 1365.62
80 Da (-P)
M4 1445.58
M5 1519.74
M6 1599.66
B) B.PA14
K1 1183.11
K2=M3 1365.62
P
1381.64
K3=M4 1445.58
K4=M5 1519.74
C) P.WT4
W1=M1 1167.46
P
W2=M2 1247.45
W3=M3 1365.62
P
W4=M4 1445.58
W5=M6 1599.66
D) B.WT4
N1=M3 1365.62
P
1381.64
N2=M4 1445.58
E) P.PDR7
J1=M1 1167.46
P
J2=M2 1247.73
J3 1349.73
80 Da
J4 1429.73
J5=M5 1599.46
J6 1667.69
F) B.PDR7
Q1=M1 1167.46
Q2=J3 1349.73
P
1365.62
Q3=J4 1429.73
Q4=M5 1519.83
Q5 1587.91
% Intensity
Mass (m/z)
1055.0
1185.0
1315.0
1445.0
1575.0
1705.0

**Fig. 3.4** Reflectron MALDI-TOF mass spectra recorded in negative ion mode of Lipid A from (A) PA14 grown under planktonic conditions (P.PA14), (B) PA14 grown as biofilm communities (B.PA14), (C) WT4 grown under planktonic conditions (P.WT4), (D) WT4 grown as biofilm communities (B.WT4), (E) PDR7 grown under planktonic conditions (P.PDR7), and (F) PDR7 grown as biofilm communities (B.PDR7). The spectra reveal strain- and condition-dependent variations in Lipid A composition, with distinct phosphorylation patterns and molecular profiles observed across the samples.

Furthermore, heterogeneity was found due to the difference of ±16 Da corresponding to the replacement of a C12:0 with a [C12:0(2-OH)]. The most abundant glycoform, denoted as **M4**, corresponds to the bis-phosphorylated penta-acylated, (Calculated Mass $[M-H]^-$ 1445.58 Da) with a composition of $GlcN_2P_2$[C12:0(3-OH)]$_2$[C12:0(2-OH)][C10:0(3-OH)][C12:0] (**Fig. 3.5**) (Knirel et al., 2006).

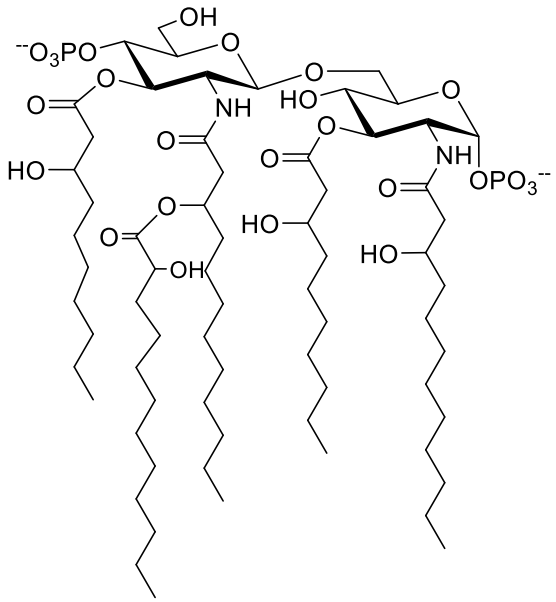


**Fig. 3.5** Bis-phosphorylated penta-acylated glycoform of *Pseudomonas aeruginosa* PA14 (reference strain) (Knirel et al., 2006). The lipid A moiety is phosphorylated at positions 1 and 4′. The acylation pattern consists of 3-OH-dodecanoic acid [C12:0(3-OH)] at positions 2 and 2′, each substituted with 2-OH-dodecanoic acid [C12:0(2-OH)], and 3-OH-decanoic acid [C10:0(3-OH)] at position 3′.

In addition, the **$M_3$** at *m/z* 1365.62 was identified as a monophosphorylated penta-acylated glycoform due to a difference of 80 Da from the signal of **$M_4$** species. The glycoform **$M_2$** with the signal at *m/z* of 1247.45 (Calculated Mass $[M-H]^-$ 1247.71 Da) corresponds to the bis-phosphorylated tetra-acylated, revealing the following composition $GlcN_2P_2[C12\text{-}3OH]_2[C12:0][C10:0(3\text{-}OH)]$. The composition was also confirmed by the presence of cluster the **$M_1$** corresponding to the monophosphorylated tetra-acylated with a calculated $[M-H]^-$ of 1167.50 Da. The ion at *m/z* 1599.66 (**$M_6$**) corresponds to the hexa-acylated bisphosphorylated species (Calculated Mass $[M-H]^-$1600.01 Da) with the composition $GlcN_2P_2[C12\text{-}3OH]_2[C12]_2[C10\text{-}3OH]_2$. The ion at *m/z* 1519.74 (**M5**) is assigned to the monophosphorylated form of **$M_6$**, likely resulting from the loss of one phosphate group (**Table 3.2**). The MALDI-TOF spectrum of Lipid A from the same strain grown as biofilm communities (B.PA14) showed that the bis-phosphorylated **$K_3$** species are almost completely absent. The monophosphorylated penta-acylated **$K_2$** glycoform, corresponding to **$M_3$**, was the most abundant. The **$K_4$** species, also detected, corresponds to the **$M_5$** signal.

**Table 3.2** Composition of the main lipid A species of *P. aeruginosa* PA14 grown under planktonic conditions (P.PA14) and *P. aeruginosa* PA14 grown under biofilm conditions (B.PA14), as observed in the MALDI-TOF mass spectra.

| Strain | Mass $[M-H]^-$ obs | Mass $[M-H]^-$ acc | Composition | |
|---|---|---|---|---|
| **P.PA14** | 1599.66 | 1600.01 | $HexN_2P_2$[C12-3OH]$_2$[C12]$_2$[C10-3OH]$_2$ | **M6** |
| | 1519.74 | 1520.05 | $HexN_2P$ [C12-3OH]$_2$[C12]$_2$[C10-3OH]$_2$ | **M5** |
| | 1461.57 | 1461.87 | $HexN_2P_2$[C12-3OH]$_2$[C12-2OH]$_2$[C10-3OH] | |
| | 1445.58 | 1445.87 | $HexN_2P_2$[C12-3OH]$_2$[C12-2OH][C12][C10-3OH] | **M4** |
| | 1429.63 | 1429.88 | $HexN_2P_2$[C12-3OH]$_2$[C12]$_2$[C10-3OH] | |
| | 1381.61 | 1381.90 | $HexN_2P$[C12-3OH]$_2$[C12-2OH]$_2$[C10-3OH] | |
| | 1365.62 | 1365.91 | $HexN_2P$[C12-3OH]$_2$[C12-2OH][C12][C10-3OH] | **M3** |
| | 1349.63 | 1349.91 | $HexN_2P$[C12-3OH]$_2$[C12]$_2$[C10-3OH] | |
| | 1247.45 | 1247.71 | $HexN_2P_2$[C12-3OH][C12-2OH][C12][C10-3OH] | **M2** |
| | 1167.50 | 1167.74 | $HexN_2P$[C12-3OH][C12-2OH][C12][C10-3OH] | **M1** |
| | | | | |
| **B.PA14** | 1519.74 | 1520.05 | $HexN_2P$ [C12-3OH]$_2$[C12]$_2$[C10-3OH]$_2$ | **K4** |
| | 1445.58 | 1445.87 | $HexN_2P_2$[C12-3OH]$_2$[C12-2OH] [C12][C10-3OH] | **K3** |
| | 1381.64 | 1381.90 | $HexN_2P$[C12-3OH]$_2$[C12-2OH]$_2$[C10-3OH] | |
| | 1365.65 | 1365.91 | $HexN_2P$[C12-3OH]$_2$[C12-2OH][C12][C10-3OH] | **K2** |
| | 1211.53 | 1211.77 | $HexN_2P$[C12-3OH]$_2$[C12-2OH]$_2$ | |
| | 1183.11 | 1183.74 | $HexN_2P$[C12-3OH]$_2$[C12-2OH][C10-3OH] | **K1** |
| | 1167.50 | 1167.74 | $HexN_2P$[C12-3OH][C12-2OH][C12][C10-3OH] | |

The distribution of Lipid A species in WT4 confirmed the same trend found for PA14, with the predominance of the bis-phosphorylated penta-acylated species at *m/z* of 1445.58 (**$W_4$** corresponding to **$M_4$**) in planktonic, and the mono-phosphorylated penta-acylated Lipid A structure (**$N_1$** equivalent to **$M_3$)** when the bacterium was grown as a biofilm community (**Table 3.4**).

**Table 3.4**Composition of the main lipid A species of *P. aeruginosa* WT4 grown under planktonic conditions (P. WT4) and *P. aeruginosa* WT4 grown under biofilm conditions (B.WT4), as observed in the MALDI-TOF mass spectra.

| Strain | Mass [M-H]- obs | Mass [M-H]- acc | Composition | |
|---|---|---|---|---|
| **P.WT4** | 1599.62 | 1600,01 | $HexN_2P_2$[C12-3OH]$_2$[C12]2[C10-3OH]$_2$ | **W5** |
| | 1445.54 | 1445.87 | $HexN_2P_2$[C12-3OH]$_2$[C12-2OH][C12][C10-3OH] | **W4** |
| | 1429.54 | 1429.88 | $HexN_2P_2$[C12-3OH]$_2$[C12]$_2$[C10-3OH] | |
| | 1365.58 | 1365.91 | $HexN_2P$[C12-3OH]$_2$[C12-2-OH][C12][C10-3OH] | **W3** |
| | 1349.58 | 1349.91 | $HexN_2P$[C12-3OH]$_2$[C12]2[C10-3OH] | |
| | 1247.42 | 1247.71 | $HexN_2P_2$[C12-3OH][C12-2OH] [C12][C10-3OH] | **W2** |
| | 1167.47 | 1167.74 | $HexN_2P$[C12-3OH]$_2$[C12][C10-3OH] | **W1** |
| **B.WT4** | 1461.54 | 1461.87 | $HexN_2P_2$[C12-3OH]$_4$[C10-3OH] | |
| | 1445.57 | 1445.87 | $HexN_2P_2$[C12-3OH]$_3$[C12][C10-3OH] | **N2** |
| | 1381.60 | 1381.90 | $HexN_2P$[C12-3OH]$_4$[C10-3OH] | |
| | 1365.61 | 1365.91 | $HexN_2P$[C12-3OH]$_3$[C12][C10-3OH] | **N1** |

The PDR7 strain also exhibited distinct phosphorylation patterns depending on the growth mode. In the negative-ion MALDI-TOF spectrum of Lipid A from planktonically grown cells (P.PDR7), the major ion at *m/z* 1429.54 (**J$_4$**) corresponds to the bisphosphorylated penta-acylated species, in which C12:0(2-OH) is replaced by C12:0. As observed for PA14, the ion at *m/z* 1247.41 (**J$_2$** corresponding to **M$_2$**) was assigned to the bisphosphorylated tetra-acylated form. Importantly, the ion at *m/z* 1667.69 (**J$_6$** species, calculated [M-H]$^-$ 1668.11 Da) corresponds to the bisphosphorylated hexa-acylated glycoform with the composition $GlcN_2P_2$[C12:0(3-OH)]$_2$[C10:0(3-OH)][C12:0]$_2$[C16:0], and was detected exclusively in PDR7 under planktonic growth conditions.

When the bacterium PDR7 was grown as a biofilm community (B.PDR7), the MALDI-TOF spectrum revealed a predominance of the monophosphorylated penta-acylated glycoform (**Q$_2$** corresponding to **J$_3$**), along with the **Q$_4$** species corresponding to **M$_5$**. In addition, only the ion at *m/z* 1587.91 (**Q5**) corresponding to the monophosphorylated hexa-acylated species (**J$_6$** -80 Da) was evident.

Interestingly, the PDR7 strain demonstrated distinct phosphorylation patterns under different growth conditions. The major signal observed at *m/z* 1429.54 (**J4**) in negative ions MALDI-TOF mass spectra of Lipid A from the pan-drug resistant strain PDR7, grown under planktonic (P.PDR7), corresponded to bis-phosphorylated penta-acylated Lipid A, in which the C12:0(2-OH) is replaced by the C12:0. As already found for P.PA14, the signal at *m/z* 1247.41 (**J2** corresponding to **M2**) was attributed to the bis-phosphorylated tetra-acylated Lipid A structure. In addition, the signal at *m/z* value of 1667.69 (**J6**) (Calculated Mass $[M-H]^-$ 1668.11 Da) corresponded to the bis-phosphorylated hexa-acylated glycoform with the following composition: $GlcN_2P_2$[C12:0(3-OH)]$_2$[C10:0(3-OH)] [C12:0]$_2$[C16:0]. Interestingly, this hexa-acylated structure containing C16:0 had already been observed in Lipid A extracted from *P. aeruginosa* clinical isolates from individuals affected by CF, but not in laboratory-adapted strain PA14 [20]. Finally, the MALDI TOF mass spectrum of PDR7 grown in as biofilm communities revealed that the main Lipid A glycoform **J4** corresponds to the monophosphorylated penta-acylated (**Q3**) (**Table 3.5**).

**Table 3.5** Composition of the main Lipid A species of *P. aeruginosa* PDR7 grown under planktonic conditions (P.PDR7) and *P. aeruginosa* PDR7 grown under biofilm conditions (B.PDR7), as observed in the MALDI-TOF mass spectra.

| Strain | Mass $[M-H]^-$ | Mass $[M-H]^-$ acc | Composition | |
|---|---|---|---|---|
| **P.PDR7** | 1667.69 | 1668,11 | $HexN_2P_2$[C12-3OH]$_2$[C12]$_2$[C10-3OH][C16] | **J6** |
| | 1599.62 | 1600.01 | $HexN_2P_2$[C12-3OH]$_2$[C12]$_2$[C10-3OH]$_2$ | **J5** |
| | 1445.54 | 1445.87 | $HexN_2P_2$[C12-3OH]$_3$[C12][C10-3OH] | **J4** |
| | 1429.54 | 1429.88 | $HexN_2P_2$[C12-3OH]$_2$[C12]$_2$[C10-3OH] | |
| | 1349.58 | 1349.91 | $HexN_2P$[C12-3OH]$_2$[C12]$_2$[C10-3OH] | **J3** |
| | 1247.41 | 1247.71 | $HexN_2P_2$[C12-3OH]$_2$[C12][C10-3OH] | **J2** |
| | 1167.46 | 1167.74 | $HexN_2P$ [C12-3OH]$_2$[C12][C10-3OH] | **J1** |
| | | | | |
| **B.PDR7** | 1587.91 | 1588.14 | $HexN_2P$ [C12-3OH]$_2$[C12]$_2$[C10-3OH][C16] | **Q5** |
| | 1519.83 | 1520.05 | $HexN_2P$ [C12-3OH]$_2$[C12]$_2$[C10-3OH]$_2$ | **Q4** |
| | 1445.65 | 1445.87 | $HexN_2P_2$[C12-3OH]$_3$[C12][C10-3OH] | |
| | 1429.73 | 1429.88 | $HexN_2P_2$[C12-3OH]$_2$[C12]$_2$[C10-3OH] | **Q3** |
| | 1365.72 | 1365.91 | $HexN_2P$[C12-3OH]$_2$[C12-2OH][C12][C10-3OH]] | |
| | 1349.73 | 1349.91 | $HexN_2P$[C12-3OH]$_2$[C12]$_2$[C10-3OH] | **Q2** |
| | 1167.46 | 1167.74 | $HexN_2P$ [C12-3OH]$_2$[C12][C10-3OH] | **Q1** |

## 3.5 Biological assays

Metabolic activity analyses by MTT, reported in **Fig. 3.6**, showed that all the tested samples were not cytotoxic in agreement with ISO 10993-5. In general, **Fig. 3.6** shows that increasing doses of both LPS and Lipid A corresponded to a decreased viability of cells; however, appropriate statistical analyses were performed. It has to be noted that longer incubation with higher concentrations, especially for biofilm-derived LPS and Lipid A, showed viability lower than 69% of the control (**Fig. 3.6 B**)(Srivastava et al., 2018).

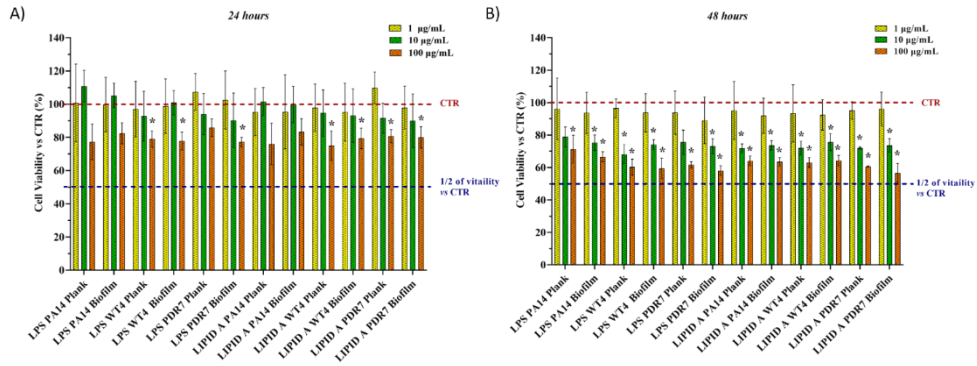


**Fig. 3.6** Cell viability evaluations were performed by MTT assay on murine primary lung-derived fibroblasts treated with *P. aeruginosa* LPS or Lipid A at 1-10-100 µg/mL for 24 (A) and 48 (B) hours. Data are presented as mean± SD. t-test was used to compare the significance of each treatment with respect to CTR (* $p < 0.05$). Planktonic form is indicated as PLANK. The red dotted line indicates the CTR (100% value). The blue dotted line indicates values that are equivalent to half of CTR (50%).

To assess the ability of LPSs and Lipids A to affect the inflammatory pathway, IL-6 and TLR-4 mRNA modulation in treated and untreated murine fibroblasts was analyzed (**Fig. 3.7**). In this respect, all the samples significantly ($p<0.05$) up-regulated IL-6 gene expression for CTR (except for LPS PA14 plank), confirming they can prompt inflammatory pathways. In detail, as shown in **Fig. 3.7 A**, biofilm growth conditions appeared more effective in increasing IL-6 gene expression than their respective planktonic ones. Moreover, for both LPSs and Lipids A, the strains WT4 and PDR7 showed higher efficacy when compared to reference-derived ones (namely PA14) at each tested concentration. At 10 µg/mL, among the LPSs, IL-6 up-regulations were more marked for WT4 biofilm (about 30-fold) and PDR7 biofilm (about 40-fold).

When comparing Lipid A treatments, P.PDR7, prompted gene expression 45-fold for IL-6 compared to untreated cells. Instead, at higher doses, all Lipid A samples and LPS B.PDR7 induced an over 50-fold increase of IL-6 gene expression compared to untreated cells (**Fig. 3.7 A**). Even higher increments were found for B.WT4 and P.PDR7 Lipids A and these latter also resulted significantly ($p<0.05$) effective compared to their LPSs (namely LPS B.WT4 and LPS P.PDR7), respectively. Concerning LPSs, biofilm growth proved more effective than respective planktonic forms, the most effective being B.PDR7, with IL-6 up-regulation of about 70-fold with respect to CTR.

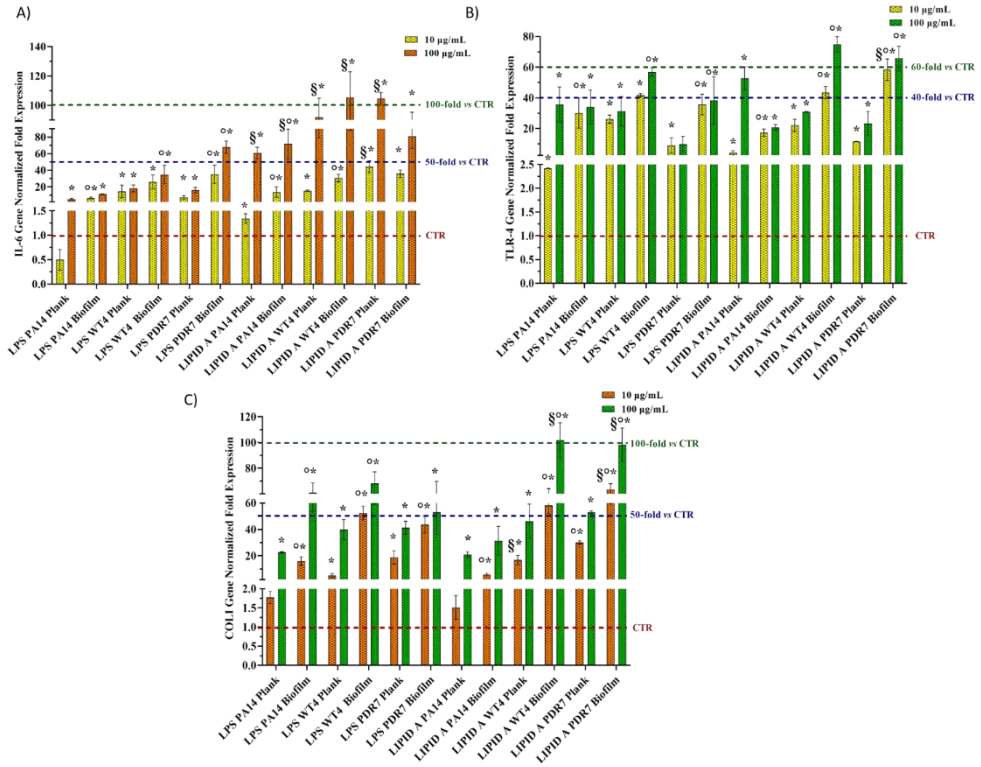


**Figure 3.7** Gene expression analyses performed by qRT-PCR on murine primary lung-derived fibroblasts treated with *P. aeruginosa* LPS or Lipid A at 10-100 µg/mL for 24 hours of IL-6 (A), TLR-4 (B) and COL 1A1(C). Data are presented as mean± SD. t-test was used to compare the significance of each treatment with respect to CTR (* $p < 0.05$), biofilm form vs relative plank form ($p < 0.05$) and Lipid A biofilm or plank vs relative LPS biofilm or plank form (§ < 0.05). Planktonic form is indicated as PLANK. In fig A and C, red dotted line indicates CTR (1 value), blue dotted line indicates 50 value, and the green dotted line indicates 100 value. In fig B, red dotted line indicates CTR (1 value), blue dotted line indicates value 40, and green dotted line indicates value 60.

**Fig. 3.7 B** showed that all the samples significantly ($p<0.05$) up-regulated TLR-4 gene expression compared to CTR. For both tested concentrations, the major efficacy was found for LPSs and Lipids A derived from biofilm communities compared to the planktonic growth for all three strains. In detail, at low concentrations, the LPS and Lipids A obtained from the reference strain were less effective than the ones isolated from the clinical isolates. In particular, the planktonic forms resulted in the weakest with TLR-4 increase vs untreated cells of about 2-fold and 4-fold for LPS and Lipid A, respectively (**Fig. 3.7 B**). Differently from IL-6 results, B.PDR7 Lipid A strongly increased TLR-4 (about 58-fold vs CTR). At higher concentrations, PA14 LPS from both planktonic and biofilm cultivations had a very similar effect in TLR-4 gene modulation. For this biomarker, B.WT4 and B.PDR7 derived LPS and Lipid A showed a major efficacy compared to the planktonic-derived molecules (**Fig. 3.7 B**).
COL 1A1 was also analyzed at the transcriptional level. Relative results showed its over-expression ($p<0.05$) vs CTR in all treatments (**Fig. 3.7 C**). Also, for COL 1A1 the upregulation was less marked for LPS and Lipid A isolated/purified from P.PA14 compared to the others (about 1.7-fold and 1.5-fold). For both the tested concentrations, biofilms-derived forms were prompting expression more than the corresponding planktonic ones. In fact, at 10 μg/mL LPS B.WT4 and LPS B.PDR7 presented an up-regulation of COL 1A1 compared to CTR of about 52-fold and 43-fold, and their Lipid A led to an increase of about 58-fold and 63-fold, respectively. Lastly, at high doses in the presence of B.WT4 and B.PDR7 Lipids A, COL 1A1 gene expression increased about 100-fold in comparison to untreated cells and these latter resulted significantly ($p<0.05$) more effective than the corresponding LPSs .

To assess the inflammation pathway activation, THP1-Blue™ cells were employed here. **Fig. 3.8** shows the results obtained in the *in vitro* model presented here, upon treatments of murine primary lung-derived fibroblasts with LPSs or Lipid A derived from three strains of *P. aeruginosa.* In fact, the supernatants were collected after 24 h treatments from the multiwell and added to THP1-Blue™ cells. In detail, as displayed by the graph in **Fig. 3.8**, at low concentration, the PA14 LPSs and Lipid As resulted in a NF-κB activation increase lower/similar to that in untreated cells. B.PDR7 Lipid A showed to increase NF-κB activation more than 2-fold with vs CTR. On the other hand, at high doses, all the samples significantly ($p<0.05$) increased NF-κB

activation with respect to untreated cells. LPSs and Lipid A derived from the reference strain (PA14) showed similar behaviour to the untreated cells or only modest upregulation. Furthermore, NF-κB activation was similarly enhanced by LPSs and Lipid As isolated from WT4 grown in both planktonic and biofilm conditions. Finally, both LPS and Lipid A derived from B.PDR7 prompted the highest NF-κB activation (> 3-fold vs CTR).

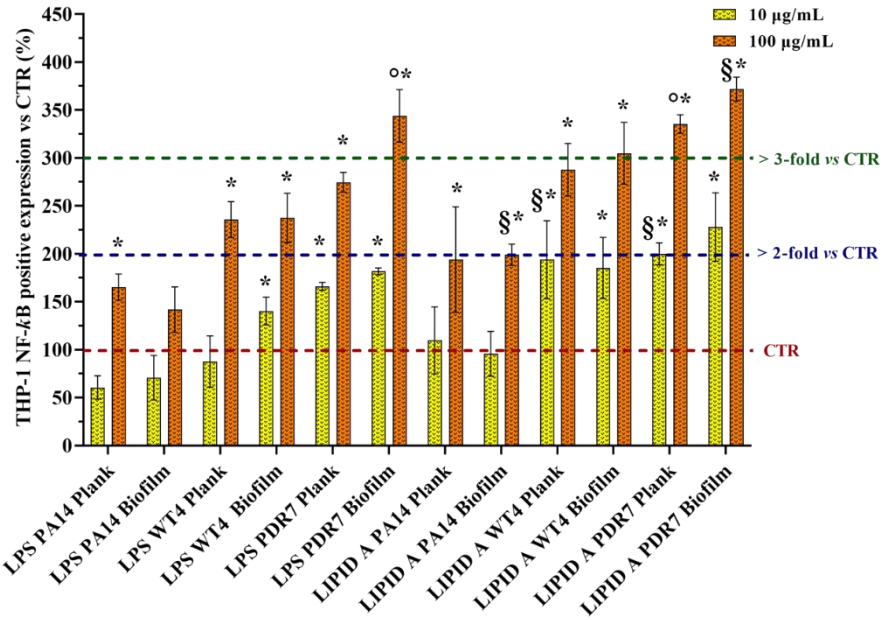


**Fig. 3.8** Spectrophotometric quantification of NF-κB by QUANTI-Blue™ assay performed on supernatants of murine primary lung-derived fibroblasts treated with P. aeruginosa LPS or Lipid A at 10 (yellow) and100 (orange) µg/mL for 24 hours. Data are presented as mean±SD. t-test was used to compare the significance of each treatment compared to CTR (* $p < 0.05$), biofilm form vs relative planktonic form ($p < 0.05$), and Lipids A biofilm or planktonic vs relative LPS biofilm or planktonic form (§ $< 0.05$). Planktonic form is indicated as PLANK. The red dotted line indicates the CTR (100% value). The blue dotted line indicates values that are equivalent to double of CTR (200%) and green dotted line indicated values that are equivalent to three times the CTR (300%).

The expression of COL1A1, NF-*k*B and caspase-4 proteins in murine fibroblasts treated with LPS (100 µg/mL) based samples is shown in **Fig. 3.9 A**. In detail, the data obtained demonstrated that all the samples tested, except for the P.PA14, significantly ($p< 0.05$) increased COL1A1 vs untreated cells. Moreover, PDR7 planktonic and biofilm up-regulated collagen protein

expression by about 2.5 and 2.7-fold compared to CTR, thus confirming a potential factor influencing tissue fibrosis. Also, NF-*k*B was significantly higher than CTR ($p<0.05$) for all samples except PA14 planktonic. Generally, it can be noted that in cells treated with LPS isolated from cells grown in biofilm conditions, NF-*k*B up-regulation was superior with respect to the relative planktonic ones.

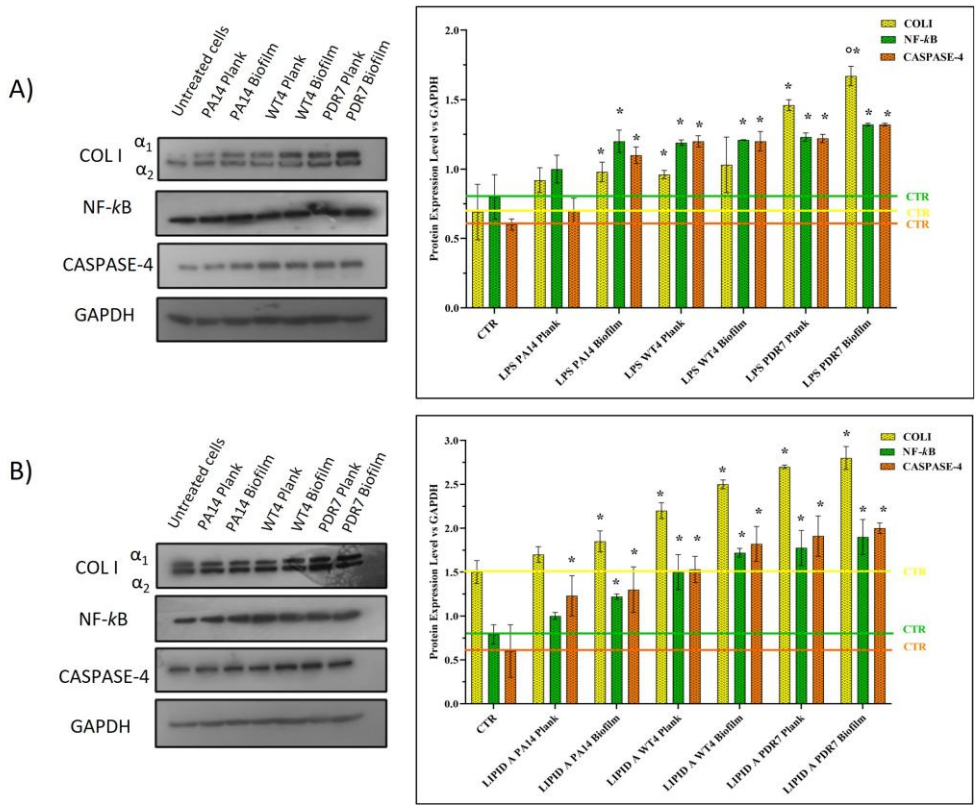


**Fig. 3.9** NF-kB, CASPASE-4 and COL 1A1 protein expression analyses performed by western blotting on murine primary lung-derived fibroblasts treated with *P. aeruginosa* LPS (A) or Lipid A (B) at 100 µg/mL for 48 hours. Data are presented as mean± SD of two different western blotting, the images of signals are representative of one of them. t-test was used to compare the significance of each treatment with respect to CTR (* $p < 0.05$). Planktonic form is indicated as PLANK. Yellow, green and oranges lines indicate the values of CTR for COLI, NF-kB and CASPASE-4 respectively.

The highest increase of this biomarker was revealed for fibroblasts (mFB) treated with B.WT4 and B.PDR7 LPSs (1.6-fold vs CTR and 1.7-fold vs CTR, respectively). Considering caspase-4, a significant ($p<0.05$) increase was observed for all the samples, except for PA14 planktonic. More precisely, LPS from B.WT4 and B.PDR7 confirmed a major effect (2-fold and 2.3-fold vs untreated cells). **Fig. 3.9 B** also displayed that Lipid A samples significantly ($p< 0.05$) enhanced COL1A1 protein expression vs untreated cells, except for the P.PA14. Lipid A from B.PDR7 showed a collagen increase with respect to untreated cells of about 1.6-fold. For NF-*k*B, PA14 Lipid A in planktonic form was less effective with respect to the other tested samples. In detail, WT4 planktonic and biofilm increased about 1.8-fold in this biomarker vs untreated cells; besides, only B.PDR7 Lipid A showed 2.4-fold up-regulation. Finally, caspase-4 was significantly ($p<0.05$) increased with respect to untreated cells in all samples, that presented a very similar profile, even among planktonic and biofilm culture conditions.

Secreted IL-6 was quantified by ELISA in untreated and treated cell supernatants (**Fig. 3.10 A**) was higher in treated samples with respect to CTR (except for LPS B.PA14). Higher concentrations were found in LPS B.PDR7 and Lipid A B.PDR7 treatments, both being more effective than the corresponding planktonic ones. In addition, B.PDR7-derived samples showed Lipid A to better upregulate IL-6 than LPS. On the other hand, when the dose increased (100 μg/mL), all treatments significantly increased IL-6 secretion (**Fig. 3.10 B**). Moreover, for each of the biofilm-derived molecules a significant ($p<0.05$) increase of IL-6 was found compared to the relative planktonic form. Finally, the highest up-regulation of this biomarker was found for B.PDR7 LPS treated cells (about 40-fold vs CTR), followed by PDR7 Lipid A from both planktonic and biofilm growths (about 50-fold and 60-fold vs CTR respectively).

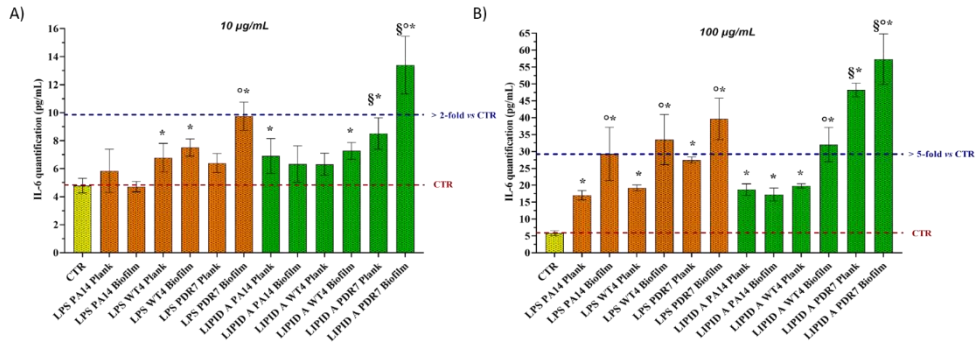


**Figure 3.10** IL-6 ELISA assay: secretion of the interleukin by murine lung primary fibroblasts treated with *P. aeruginosa* LPS or Lipid A at 10 (A) and 100 (B) µg/mL for 24 hours. Data are presented as mean± SD. t t-test was used to compare the significance of each treatment compared to CTR (* $p < 0.05$), biofilm form vs relative plank form ($p < 0.05$), and Lipid A biofilm or plank vs relative LPS biofilm or plank form (§ $< 0.05$). Planktonic form is indicated as PLANK. In fig A, the red dotted line indicates the CTR, and the blue dotted line indicates values that are equivalent to double of CTR. In fig B, the red dotted line indicates the CTR, and the blue dotted line indicates values that are equivalent to five times the CTR.

## 3.6 Discussion and conclusion

The treatment of antimicrobial resistance-associated diseases poses a formidable challenge in medicine. It is well established that bacteria can adapt to the host, causing the persistence of infection, and that the adaptation is often related to the bacteria's ability to form biofilms (Cámara et al., 2022).

*P. aeruginosa* is commonly associated with hospital-acquired infections, infections in immunocompromised hosts, and chronic infections in people with structural lung diseases such as cystic fibrosis (Govan & Deretic, 1996). It is widely believed that biofilm growth within the lungs of people with CF (pwCF) is a hallmark for the facilitation of disease (Govan & Deretic, 1996). Biofilms promote antibiotic tolerance by reducing bacterial metabolic activity and slowing growth, while the dense extracellular matrix limits antimicrobial penetration, further enhancing survival (Pai et al., 2023; Uruén et al., 2020). Beyond tolerance, biofilms facilitate the spread of antibiotic resistance through enhanced HGT mechanisms, including conjugation, transformation, and transduction, with plasmids and integrons further propagating resistance within bacterial communities (Michaelis & Grohmann, 2023). Moreover, *P. aeruginosa* biofilms resist immune clearance by incorporating Type I collagen, impairing neutrophil phagocytosis (Zhou et al., 2023). Despite neutrophil recruitment and complement activation, bacteria in biofilm evade opsonization

and other defenses (Mauch et al., 2018; Parsek & Singh, 2003; Shaikh et al., 2022). Overall, the combination of antibiotic tolerance, genetic resistance, and immune evasion underscores the multifaceted survival strategies of *P. aeruginosa* in chronic lung infections. Investigating the structural and functional differences between planktonic and biofilm-grown strains is therefore essential to understanding the mechanisms underlying chronic infection and antibiotic recalcitrance, justifying the focus of the present research. In this study, we established the chemical structure of Lipids A from *P. aeruginosa* strains isolated from two pwCF at different stages of infection to find out a relationship between the structure and the role of LPS accounting for different profiles of antibiotic resistance.

The analyzed strains, PA14, WT4, and PDR7, were grown under planktonic (P) and biofilm conditions (B), which reproduce the pulmonary environment of pwCF (Scoffone et al., 2017). The structural study performed on purified Lipids A suggested a common response of the strains moving from planktonic to a biofilm lifestyle. Specifically, MALDI-TOF mass spectrometry revealed that the previously reported transition affects the Lipid A structure in the phosphorylation pattern. The antibiotic-sensitive strains PA14 and WT4 displayed a similar distribution of Lipid A species, with bisphosphorylated pentacylated as the predominant. However, the same strains grown in biofilm showed monophosphorylated species as the most abundant. Interestingly, the PDR7 strain, isolated from a patient with chronic CF infection, showed further alterations in Lipid A acylation and phosphorylation, likely linked to mutations in Lipid A regulatory systems such as PhoP/PhoQ and PmrA/PmrB. Indeed, both systems modify Lipid A structure in response to environmental stress, thereby enhancing bacterial resistance (Scoffone et al., 2017).

This phenomenon has also been observed in other chronic pathogens, such as *Burkholderia cenocepacia*, a multidrug-resistant bacterium that uses similar mechanisms to adapt and survive in the lungs of pwCF (Scoffone et al., 2017). The predominance of monophosphorylated Lipid A species in biofilm-grown bacteria is particularly relevant for chronic infections in pwCF, where high antibiotic concentrations and a strong immune response challenge infection eradication. This structural shift is a strategy already found in LPS modification. The substitution of the phosphate groups by L-Ara4N decreases the negative charge on the bacterial membrane, allowing bacteria to evade immune detection and increase their resistance to cationic antibiotics such as polymyxin B and colistin, to which the PDR7 strain is resistant (Gellatly &

Hancock, 2013; Olaitan et al., 2014; Raetz & Whitfield, 2002; Scoffone et al., 2017).

A comprehensive array of biological and biochemical assays was performed to compare LPS and Lipid A purified from planktonic and biofilm cultures of clinical strains of *P. aeruginosa* (PA14, WT4, and PDR7). The results showed that LPS and Lipid A species isolated from biofilm-grown strains, particularly WT4 and PDR7 but also for PA14, had a more pronounced impact on affecting the inflammatory markers TLR4, NF-*k*B, and COL1A1, which are key elements in the fibrotic process observed in the lungs of pwCF. All the samples modulated NF-*k*B as shown by monocyte activation (THP1 blue assay) and by western blotting analyses. These data, together with gene expressions, support that the higher the concentration, the higher the effectiveness in TLR-4 mediated prompting of NF-*k*B expression and translocation to nuclei, and COL1A1 modulation. LPS and Lipid A derived from the biofilm of WT4 and PDR7 had a greater impact on the inflammation pathway-related biomarkers. The same effect was observed for LPS and Lipid A derived from PA14 when grown in biofilm, even if less pronounced. Furthermore, it is worth noting that laboratory reference strains, such as PA14, fail to mimic *in vivo* bacterial infections for high genome plasticity that drives bacteria to rapidly adapt to the habitat where they grow. For this reason, even if PA14 is a hypervirulent strain it is plausible that it is less immunogenic compared to clinical strains.

The molecules extracted from clinical isolates showed a relevant increase in TLR-4 as a key receptor correlated to the inflammation cascade through NF-*k*B, which in turn increased the secretion of IL-6. Relevant differences among control and reference strains, compared to clinical isolates from the early pathological state and the chronic one, were found. Specifically, for all the experimental sets, the treatments related to *P. aeruginosa* PDR7 strain showed the highest prompting of the inflammatory cascade here tested, even without showing significant cytotoxic effects.

In most of the assays, WT4 and even more PDR 7 showed a more marked COL1A1 expression and production as a fingerprint for a fibrosis-induced status in the *in vitro* model here tested. It has been shown that COL1A1 fibers may interact with biofilm even encapsulating the pathogens, thus hampering to eradication of the infection (hampering diffusion of the antibiotics, for instance). Despite the caspase-4 upregulation, cell death, even at higher doses, was not so relevant, whereas a fibrotic process was probably ongoing due to persistent inflammation prompted by TLR-4 mediated action of the diverse LPS and Lipid A.

The modulation of LPS/Lipid A structure and the consequent inflammatory response could be a marker for formulating hypotheses about the stage of infection. It is important to acknowledge that, despite the significance of the results obtained, this study has some inherent limitations that should be considered and addressed in future investigations. First, the analysis was performed on a limited number of strains, which inevitably restricts the generalizability of the conclusions. This work should therefore be regarded as a preliminary contribution within a broader research program. Second, all strains analyzed, exhibited, in laboratory conditions, a non-mucoid phenotype. By contrast, mucoid *P. aeruginosa* variants, frequently isolated in chronic CF infections, are known to display modified LPS structures and distinct immunogenic properties. Extending the analysis to include mucoid strains would enable more comprehensive comparisons, not only among isolates collected at different stages of infection and characterized by diverse resistance profiles and growth conditions, but also across distinct phenotypic states (mucoid vs. non-mucoid). Future studies involving a larger and more representative collection of clinical isolates, including mucoid variants, will therefore be crucial to fully elucidate the breadth of *P. aeruginosa* adaptations in CF lungs and to validate and expand the present findings.

### 3.7 LPS isolation from *P. aeruginosa* WT2, MDR1,MDR5 and PDR5 grown under planktonic conditions and as biofilm communities

LPS from *P. aeruginosa* strains WT2, MDR1, MDR5, and PDR5 grown under planktonic conditions and as biofilm communities were extracted from bacterial cells using the hot phenol/water method (Westphal, 1965) and subsequently purified by dialysis and ultracentrifugation as previously described (Petersson et al., 1997).
The LPS yields ranged between 2% and 6%, as reported in **Table 3.6**.

**Table 3.6** Summary of the *P. aeruginosa* strains analyzed, the amount of bacterial cells used, and the LPS extraction yield expressed as a percentage (w/w).

| ***P. aeruginosa* strain** | **Dried cells (mg)** | **LPS (yield)** |
|---|---|---|
| **Strains grown under planktonic conditions (P)** | | |
| **WT2** | 630.0 | 2.65 % |
| **MDR1** | 495.0 | 2.79 % |
| **MDR5** | 355.0 | 3.02 % |
| **PDR5** | 395.0 | 4.30 % |
| **Strains grown as biofilm communities (B)** | | |
| **WT2** | 75.0 | 2.13 % |
| **MDR1** | 42.0 | 2.51 % |
| **MDR5** | 110.0 | 1.82 % |
| **PDR5** | 240.0 | 6.25 % |

All LPSs were then analyzed by 14% DOC-PAGE and visualized by silver staining, using smooth-type LPS from *E. coli* O111:B4 as a reference. Strains cultured under planktonic conditions exhibited a high-molecular-weight polysaccharide fraction, consistent with the presence of smooth-type LPS (**Fig. 3.11**).

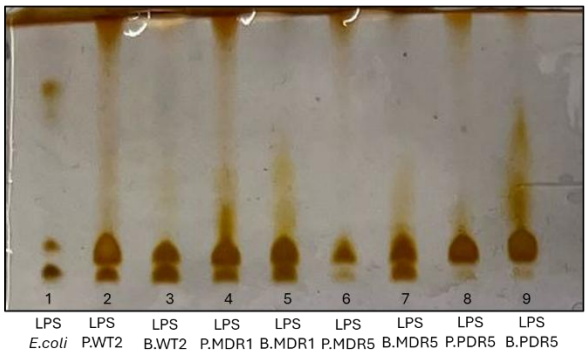


**Fig. 3.11** Electrophoretic profiles of lipopolysaccharides (LPS) from *P. aeruginosa* strains analyzed by 14% DOC-PAGE and silver staining. Smooth-type LPS from *E. coli* O111:B4 was used as a reference. P, planktonic culture conditions; B, culture grown as biofilm communities.

## 3.8 HR-MAS analysis

HR-MAS NMR analysis was used to obtain a preliminary characterization of LPS from *P. aeruginosa* strains WT2, MDR1, MDR5, and PDR5 grown under planktonic and as biofilm communities. Initial experiments performed directly on intact bacterial cells, after repeated washing with $D_2O$ and lyophilization, did not yield informative spectra (data not shown), indicating that cellular complexity interfered with LPS signal resolution.

Subsequent analyses were conducted on purified LPS extracts (3-4 mg), which produced well-resolved $^1$H-NMR spectra. Characteristic carbohydrate resonances were detected, including signals in the anomeric region (δ 4.5-5.5 ppm) corresponding to glycosidic linkages, resonances in the carbinolic region (δ 3.0-4.5 ppm) attributable to ring protons of hexoses and hexosamines, and high-field resonances (δ 1.0-1.5 ppm) associated with methyl groups of deoxy sugars (**Fig. 3.12**). These spectral features are consistent with typical LPS carbohydrate structures. Notably, qualitative comparison of spectra revealed differences between planktonic and biofilm growth conditions within each strain, as well as subtle variations among antibiotic-susceptible, multidrug-resistant (MDR), and pan-drug-resistant (PDR) phenotypes.

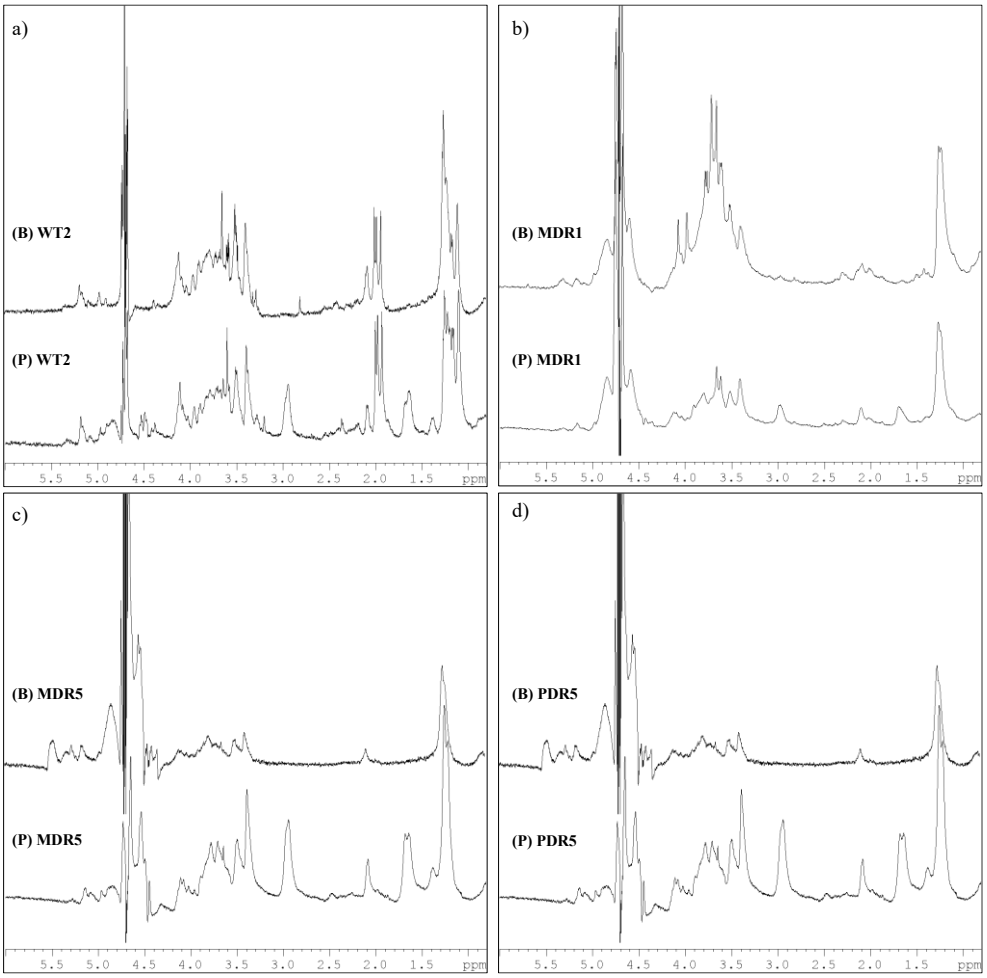


**Fig 3.12.** HR-MAS $^{1}H$ NMR spectra of LPS extracted from *Pseudomonas aeruginosa* strains grown under planktonic (P) and biofilm (B) conditions, recorded in $D_2O$ at 298 K. (a) wild-type strain WT2; (b) multi-drug resistant strain MDR1; (c) multi-drug resistant strain MDR5; (d) pan-drug resistant strain PDR5.

This approach enabled a rapid comparative analysis across all strains investigated; nevertheless, a more detailed study would be required to achieve full structural characterization (**Fig. 3.12**).

### 3.9 LPS glycosyl analysis

Sugar and lipid compositions of LPS from *P. aeruginosa* strains grown under planktonic conditions were determined by GC-MS after derivatization (AMGs for sugars, FAMEs for acyl residues). The fatty acid fraction was characterized by the presence of 3-hydroxydecanoic acid 10:0(3-OH) dodecanoic acid C12:0, 2-hydroxydodecanoic acid C12:0(2-OH), 3-hydroxydodecanoic acid C12:0(3-OH), and hexadecanoic acid C16:0. In addition, long-chain fatty acids such as octadecanoic acid C18:0, octadecenoic acid C18:1, and eicosanoic acid C20:0, most likely associated with phospholipids, were also detected.

The sugar composition of the LPS from each *P. aeruginosa* strain is reported in **Table 3.7**. For strains grown under planktonic conditions, the analysis was performed on purified LPS, whereas for those grown as biofilm communities, it was carried out directly on bacterial cells due to the limited amount of material available. No differences were observed between planktonic and biofilm growth; therefore, the reported sugar composition is representative of both conditions. Only *P. aeruginosa* WT2 contained the deoxyaminosugar quinovosamine (QuiN), making its composition more similar to that of the antibiotic-sensitive reference strain *P. aeruginosa* PA14 (Coulon et al., 2010).

**Table 3.7**. LPS sugar composition of the *P. aeruginosa* strains (P:planktonic; B:biofilm) analyzed in this study. Rha, rhamnose; QuiN, quinovosamine; FucN, fucosamine; Glc, glucose; GlcN, glucosamine; Hep, heptose; Kdo, 3-deoxy-D-*manno*-oct-2-ulosonic acid.

| ***P. aeruginosa* strains** | **Sugar composition** |
|---|---|
| (P) WT2 | Rha, QuiN, Glc, GlcN, Hep, Kdo |
| (b) WT2 | Rha, QuiN, Glc, GlcN, Hep, Kdo |
| (P) MDR1 | Rha, FucN, Glc, GlcN, Hep, Kdo |
| (B) MDR1 | Rha, FucN, Glc, GlcN, Hep, Kdo |
| (P) MDR5 | Rha, FucN, Glc, GlcN, Hep, Kdo |
| (B) MDR5 | Rha, FucN, Glc, GlcN, Hep, Kdo |
| (P) PDR5 | Rha, FucN, Glc, GlcN, Hep, Kdo |
| (B) PDR5 | Rha, FucN, Glc, GlcN, Hep, Kdo |

## 3.10 Lipid A isolation and compositional analysis

Lipid A was liberated by acidic hydrolysis of LPS (1.0% acetic acid, 30 min, at 100 °C). The reaction mixture was cooled and centrifuged. The sediment was resuspended in water and freeze-dried. The yield of lipid A preparations ranged from 11% to 16%.

Lipids A isolated from *P. aeruginosa* strains WT2, MDR1, MDR5, and PDR5 grown under planktonic and biofilm conditions were subjected to chemical characterization of its sugar and fatty acid constituents. GC-MS investigated the sugar moiety after derivatization to acetylated methyl glycosides (AMGs), which identified glucosamine (GlcN) as the sole carbohydrate unit. Fatty acid analysis was performed by GC-MS of fatty acid methyl esters (FAMEs), revealing the presence of C10:0(3-OH), C12:0, C12:0(2-OH), C12:0(3-OH), and C16:0, consistent with the acyl composition typically associated with *P. aeruginosa* lipid A. C18:0, C18:1, and C20:0 species are not part of the canonical acylation pattern of *P. aeruginosa* lipid A (Knirel et al., 2006) and are most likely attributable to trace phospholipid carryover co-extracted with LPS. Consequently, C18/C20 peaks were excluded from the compositional profile of lipid A.

## 3.11 MALDI-TOF MS analysis

MALDI-TOF spectra acquired in reflectron negative ion mode revealed variations in the structures of lipids A, both within the same strain grown under planktonic conditions (P.WT2, P.MDR1, P.MDR5, P.PDR5) and as a biofilm community (B.WT2, B.MDR1, B.MDR5, B.PDR5). A comparative analysis clearly distinguished the lipid profiles of antibiotic-susceptible strains (WT) from those of multi-drug-resistant (MDR) and pan-drug-resistant (PDR) strains. In addition, the comparison between planktonic and biofilm growth highlighted marked heterogeneity in the spectral patterns.

Lipid A structural characterization was achieved by combining MALDI-TOF and ESI-MS spectrometric analyses with previously published data by Knirel et al. (Knirel et al., 2006).

The MALDI-TOF spectrum of lipid A extracted from *P. aeruginosa* WT2 strain grown under planktonic conditions (P.WT2) revealed different species, including tetra-, penta- and hexa-acylated forms, with the tetra-acylated species observed at lower intensity (**Fig. 3.13**).

The most abundant $[M-H]^-$ ion signal in the planktonic spectrum was observed at *m/z* 1366.13 (calculated Mass $[M-H]^-$ 1365.91 Da), corresponding to a penta-acylated, monophosphorylated lipid A species. The proposed structure consists of a diglucosamine backbone substituted with 3-hydroxydodecanoic

acid C12:0(3-OH) at positions 2 and 2′ (amide linkages), 2-hydroxydodecanoic acid C12:0(2-OH) as a secondary acyl chain linked to the C12:0(3-OH) at position 2, dodecanoic acid C12:0 as a secondary acyl chain linked to the C12:0(3-OH) at position 2′, and 3-hydroxydecanoic acid C10:0(3-OH) ester-linked at position 3′.
The structural assignment was achieved by comparing the experimental data with previously reported literature values (Knirel et al., 2006).
The mass difference of +80.0 Da compared to the signal at *m/z* 1366.13 indicates the same acyl composition but with an additional phosphate group at position 1, consistent with a penta-acylated bis-phosphorylated species (calculated Mass $[M-H]^-$ 1445.87 Da),
Among these, a signal at *m/z* 1195.97 was observed and assigned to a tetra-acylated monophosphorylated species with the composition $GlcN_2P[C12:0(3-OH)]_2[C12:0(2-OH)][C12:0]$ (Calculated Mass $[M-H]^-$ 1195.77 Da).
Hexa-acylated species were also observed. The signal at *m/z* 1632.27 was assigned to the composition $GlcN_2P_2[C12:0(3-OH)]_2[C12:0(2-OH)]_2[C10:0(3-OH)]_2$ (Calculated Mass $[M-H]^-$ 1632.01 Da). In contrast, the ion at *m/z* 1616.3 was assigned to a structural variant of the same species, lacking a hydroxyl group on one of the acyl chains (Calculated Mass $[M-H]^-$ 1616.00 Da).

The spectral profile of lipid A isolated from WT2 grown as biofilm communities (B.WT2) showed some differences compared to the planktonic form. In addition to the signals at *m/z* 1616.36 and *m/z* 1632.36, further hexa-acylated monophosphorylated species were observed, with signals at *m/z* 1536.40 ($GlcN_2P[C12:0(3-OH)]_3[C12:0(2-OH)][C12:0][C10:0(3-OH)]_2$, Calculated Mass $[M-H]^-$ 1536.04 Da) and at *m/z* 1552.38 ($GlcN_2P[C12:0(OH)]_2[C12:0(OH)]_2[C10:0(3-OH)]_2$, Calculated Mass $[M-H]^-$ 1552.04 Da).
The most intense $[M-H]^-$ ion signal was observed at *m/z* 1382.20 (Calculated Mass 1381.90 Da), consistent with a penta-acylated, monophosphorylated lipid A species identified as $GlcN_2P[C12:0(3-OH)]_2[C12:0(2-OH)]_2[C10:0(3-OH)]$. The proposed structure consists of 3-hydroxydodecanoic acid C12:0(3-OH) at positions 2 and 2′ (amide linkages), each bearing a secondary 2-hydroxydodecanoic acid C12:0(2-OH), and a 3-hydroxydecanoic acid C10:0(3-OH) ester-linked at position 3′ and a phosphate group at position 4’.This molecule represents the hydroxylated analogue of the species at *m/z* 1366.20, which predominates under planktonic conditions.
In addition, penta-acylated phosphorylated /dephosphorylated species were observed with ion signals at *m/z* 1462.19 and *m/z* 1303.44 (Calculated Mass $[M-H]^-$ 1461.90 and 1301.90 Da), confirming the structural heterogeneity of

lipid A when the bacterium grows as biofilm communities. The monophosphorylated tetra-acyl species at *m/z* 1184.01, corresponding to $GlcN_2P[C12:0(3\text{-}OH)]_2[C12:0(2\text{-}OH)][C10:0(3\text{-}OH)]$ (calculated mass $[M\text{-}H]^-$ 1183.73), was also detected.

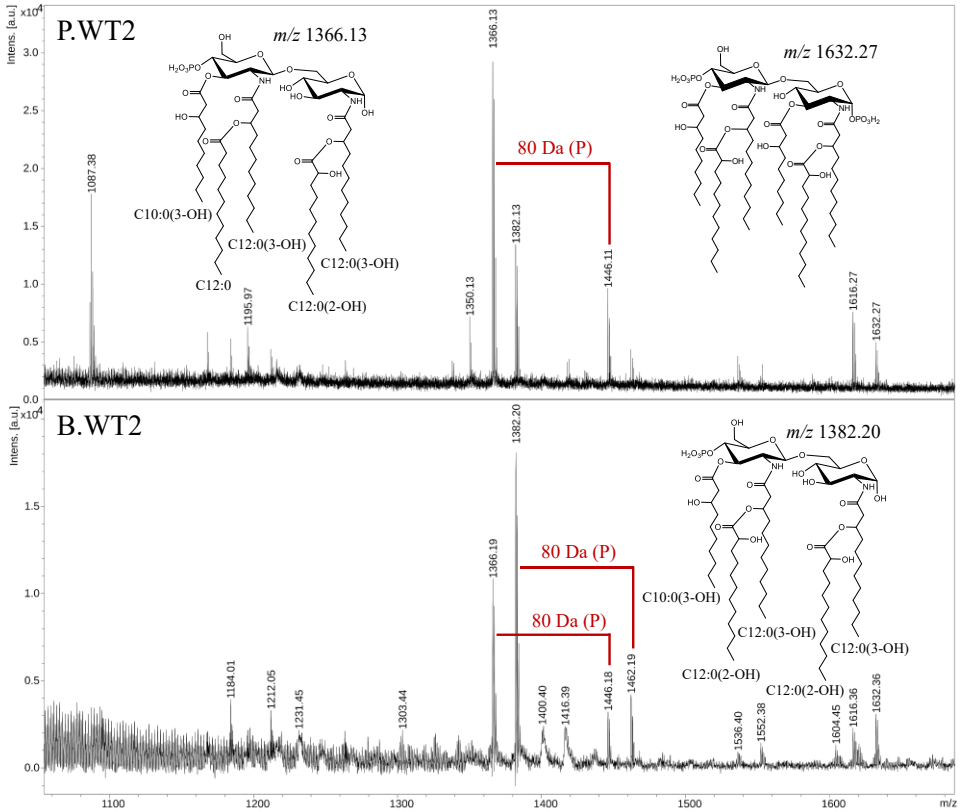


**Fig. 3.13** Negative-ion mode MALDI-TOF mass spectra of lipid A from LPS of *Pseudomonas aeruginosa* WT2. Lipid A from planktonic cells (P.WT2) is shown in the upper panel, whereas the lower panel depicts lipid A from cells grown as biofilm communities (B.WT2). The structures corresponding to the major molecular species at *m/z* 1366.13, *m/z* 1382.20 and *m/z* 1632.27 are included.

In *P. aeruginosa* MDR1 strain grown under planktonic conditions, the most abundant ion was observed at *m/z* 1366.16. Additional species differing by ±16.0 Da were also observed, consistent with hydroxylation/dehydroxylation variants. As in the WT2 strain, the bis-phosphorylated species at *m/z* 1446.19 was also detected. The most acylated form identified under planktonic conditions was observed at *m/z* 1537.33 and assigned to the composition $GlcN_2P[(C12:0(OH)]_2$ $[(C12:0(OH)][C12:0][C10:0(3\text{-}OH)_2]$.

In *P. aeruginosa* MDR1 strain grown as biofilm communities, the most abundant species was observed at *m/z* 1382.24. The bis-phosphorylated species at *m/z* 1462.23 was also observed. Finally, hexa-acylated species were detected at *m/z* 1616.40 and *m/z* 1632.40 (the latter assigned to $GlcN_2P_2$[(C12:0(3-OH)]$_2$[(C12:0(2-OH)]$_2$[C10:0(3-OH)]$_2$ (**Fig 3.14**).

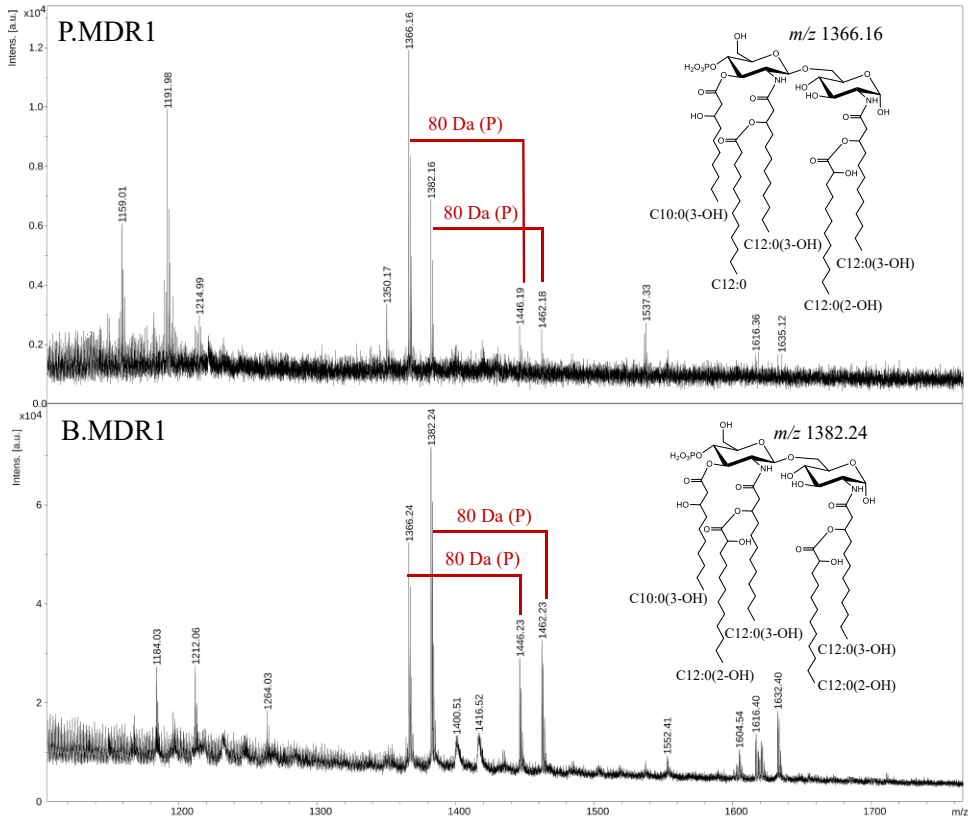


**Fig. 3.14** Negative-ion mode MALDI-TOF mass spectra of lipid A from LPS of Pseudomonas aeruginosa MDR1. Lipid A from planktonic cells (P.MDR1) is shown in the upper panel, whereas the lower panel depicts lipid A from cells grown as biofilm communities (B.MDR1). The structures corresponding to the major molecular species at *m/z* 1366.13 and *m/z* 1382.24 are included.

In *P. aeruginosa* MDR5 strain grown under planktonic conditions, the most intense species was observed at *m/z* 1366.15, together with the corresponding bis-phosphorylated species, assigned to the composition

$GlcN_2P_2[C12:0(OH)]_2[C12:0(2\text{-}OH)][C12:0][C10:0(3\text{-}OH)]$. Additional species differing by ±16.0 Da $[M\text{-}H]^-$ ions were also observed, consistent with hydroxylation/dehydroxylation variants. As in the MDR1 strain under planktonic growth, the hexa-acylated species at *m/z* 1553.31was also observed. Moreover, hexa-acylated species at *m/z* 1616.32 and *m/z* 1633.35 were also detected, as previously described in *P. aeruginosa* WT2 and MDR1.
Similarly to *P. aeruginosa* MDR1 strain, MDR5 grown as biofilm communities showed the most abundant signal at *m/z* 1382.23 $[M\text{-}H]^-$ (corresponding to *m/z* 1366.22 + 16.0 Da), along with their bis-phosphorylated form. Nevertheless, $[M\text{-}H]^-$ ion signals at *m/z* 1366.22 and *m/z* 1446.22 (±16.0 Da variants) were also observed. In addition, hexa-acylated species were detected at *m/z* 1536.43, *m/z* 1552.40, *m/z* 1616.38, and *m/z* 1632.38. Similar to the WT2 and MDR1 strains grown as biofilm communities, it also shows the ion at *m/z* 1184.04 corresponding to the monophosphorylated tetra-acyl species (**Fig. 3.15**).

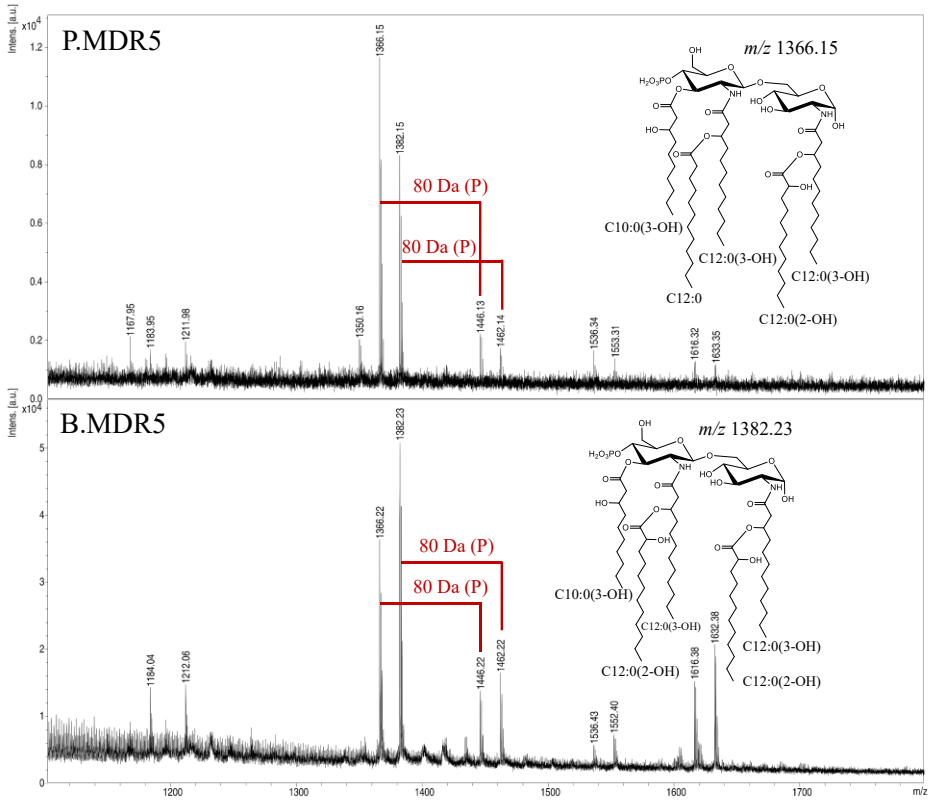


**Fig. 3.15** Negative-ion mode MALDI-TOF mass spectra of lipid A from LPS of Pseudomonas aeruginosa MDR5. Lipid A from planktonic cells (P.MDR5) is shown in the upper panel, whereas the lower panel depicts lipid A from cells grown as biofilm communities (B.MDR5).

The structures corresponding to the major molecular species at *m/z* 1366.15 and *m/z* 1382.23 are included.

The lipid A of the *P. aeruginosa* pan-drug-resistant strain (PDR5) grown under planktonic conditions and as biofilm communities was also analyzed

In *P. aeruginosa* PDR5 strain grown under planktonic conditions, the most abundant species was observed at *m/z* 1366.17, corresponding to the composition $GlcN_2P[(C12:0(OH)]_2$ [(C12:0(OH)][C12:0][C10:0(3-OH)]. This feature was shared by all *P. aeruginosa* strains analyzed in this study under planktonic conditions.

Variations due to phosphate substitution (+80.0 Da) were evident, as demonstrated by the presence of the species at *m/z* 1446.17. In addition, a single hexa-acylated species was observed at *m/z* 1616.29 corresponding to the composition $GlcN_2P_2[(C12:0(3\text{-}OH)]_2[(C12:0(2\text{-}OH)][C12:0][C\text{-}10:0(3\text{-}OH)]_2$ (**Fig 3.16**).

In *P. aeruginosa* PDR5 strain grown as biofilm communities, the most abundant species was not only that at *m/z* 1382.22, but also its corresponding bis-phosphorylated species (*m/z* 1462.21). For both species, variants differing by -16.0 Da were clearly observed. The spectrum also showed hexa-acylated species at *m/z* 1616.38 and *m/z* 1632.38. A characteristic of PDR5 biofilm cells was the presence of an additional bisphosphorylated hexa-acylated species at *m/z* 1700.49. The lipid A structure consists of a bis-phosphorylated glucosamine disaccharide backbone, with phosphate groups located at positions 1 and 4′. Primary acylation involves 3-hydroxy dodecanoic acid at positions 2 and 2′, each of which is further substituted with a secondary 2-hydroxy dodecanoic acid. At position 3′, a 3-hydroxy decanoic acid is linked, which in turn carries a secondary palmitic acid (C16:0). An additional ion at *m/z* 1684.49 was also detected, differing by -16 Da from the main species, which lacks a hydroxyl group from the C12:0(2-OH) linked to the C12:0(3-OH) at position 2′. Structural elucidation was performed based on experimental data and previously reported literature (Knirel et al., 2006). As in all lipid A samples from strains grown as biofilm communities, the monophosphorylated tetra-acyl species at *m/z* 1184.00, corresponding to $GlcN_2P[C12:0(3\text{-}OH)]_2[C12:0(2\text{-}OH)][C10:0(3\text{-}OH)]$ (Calculated Mass $[M–H]^-$ 1183.73), was detected, as well as the species at *m/z* 1196.05, as described for the lipid A of the WT2 strain grown under planktonic conditions.

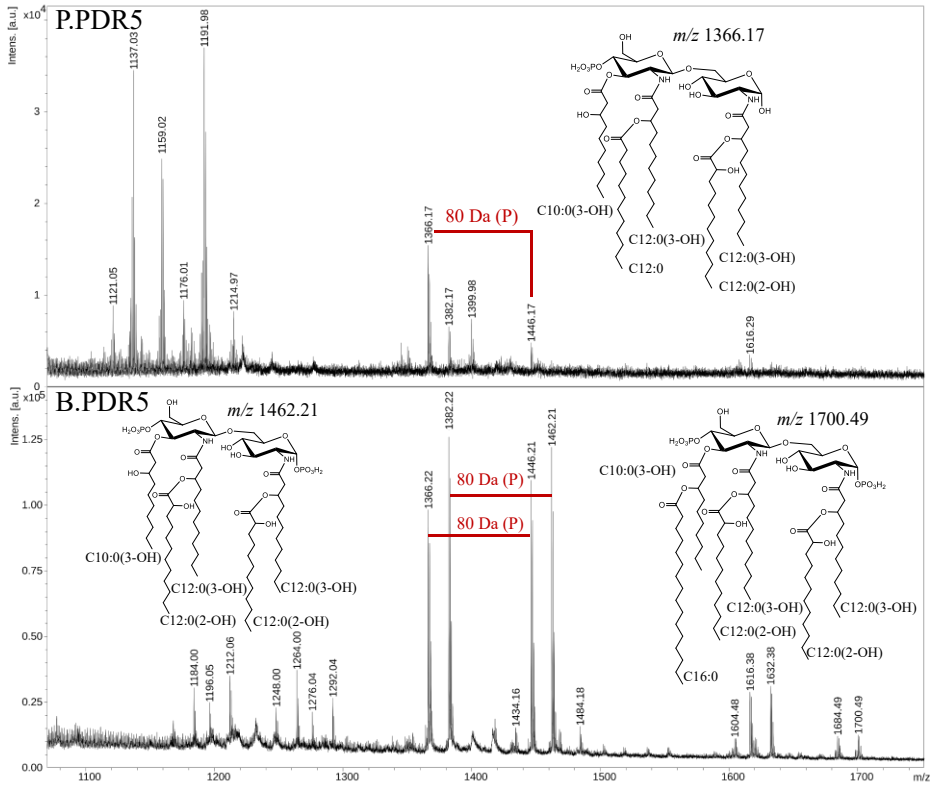


**Fig. 3.16** Negative-ion mode MALDI-TOF mass spectra of lipid A from LPS of *Pseudomonas aeruginosa* PDR1. Lipid A from planktonic cells (P.PDR1) is shown in the upper panel, whereas the lower panel depicts lipid A from cells grown as biofilm communities (B.PDR1). The structures corresponding to the major molecular species at *m/z* 1366.17, *m/z* 1462.21, and *m/z* 1700.49 are included.

In the glycoforms identified in the *P. aeruginosa* susceptible WT2 strain, in the multidrug-resistant strains MDR1 and MDR5, as well as in the pan-drug-resistant strain PDR5, slight variations were observed compared with the glycoforms described by Knirel et al. (Knirel et al., 2006). Such differences, however, may contribute to antibiotic resistance and to the inflammatory process.

Overall, MALDI-TOF mass spectra revealed consistent patterns across all lipid A samples from the analyzed *P. aeruginosa* strains. Under planktonic conditions, the dominant signal was invariably the penta-acylated monophosphorylated species at *m/z* $[M–H]^-$ theoretical 1365.91, accompanied by its bis-phosphorylated counterpart at *m/z* $[M–H]^-$ theoretical 1445.87 and by hexa-acylated variants, notably at *m/z* $[M-H]^-$ theoretical 1536.04 and

1616.00. In contrast, when the bacterium was grown as biofilm communities, lipid A was characterized by a shift toward the hydroxylated form of the secondary C12:0 on the distal glucosamine at *m/z* $[M-H]^-$ theoretical 1381.90 as the most abundant species, often accompanied by its bis-phosphorylated analogue at *m/z* $[M-H]^-$ theoretical 1461.90 and by a broader distribution of hexa-acylated species, including *m/z* $[M-H]^-$ theoretical 1616.00 and 1632.01. Notably, the *P. aeruginosa* PDR5 strain grown as biofilm communities displayed additional hexa-acylated glycoforms at *m/z* $[M-H]^-$ theoretical 1684.01 and 1700.01, which were absent in the other strains.

### 3.12 ESI-MS$^n$ analysis of lipid A from *P. aeruginosa* PDR5

Lipid A from *P. aeruginosa* PDR5 grown under planktonic conditions and as biofilm communities exhibited high structural heterogeneity, as previously observed by MALDI-TOF mass spectrometry. These samples were subjected to electrospray ionization mass spectrometry (ESI-MS) in negative ion mode in order to confirm the distribution of fatty acids, determine the position of the phosphate group in monophosphorylated species, and detect new glycoforms not observed by MALDI-TOF MS. Prior to analysis, lipid A samples were desalted and solubilized in methanol/chloroform (1:1, v/v) at a concentration of 1.0 mg/mL, following the procedure reported by Lukasiewicz et al. (Lukasiewicz et al., 2006).

#### 3.12.1 *P. aeruginosa* PDR5 planktonic

The ESI mass spectrum recorded in negative ion mode for lipid A extracted from *P. aeruginosa* PDR5 grown in planktonic conditions revealed reduced heterogeneity. The most abundant ion was detected at *m/z* 1366.04, corresponding to the monophosphorylated, penta-acylated glycoform ($GlcN_2P$(4')[C12:0(3-OH)]$_2$[C12:0(2-OH)][C12:0][C10:0 (3-OH)]). Glycoforms differing by ±16.0 Da were also evident. Mass differences of 80.0 Da indicated the presence of bisphosphorylated species, although these represented only a minor fraction. Among the hexa-acylated glycoforms, the most prominent was observed at *m/z* 1536.13, consistent with the addition of one C10:0(3-OH) to the *m/z* 1366.04 species (Δ 170.0 Da). Another hexa-acylated species was visible at *m/z* 1604.23, corresponding to the addition of one C16:0 to the *m/z* 1366.0 species (Δ 238.0 Da) (**Fig 3.17**).

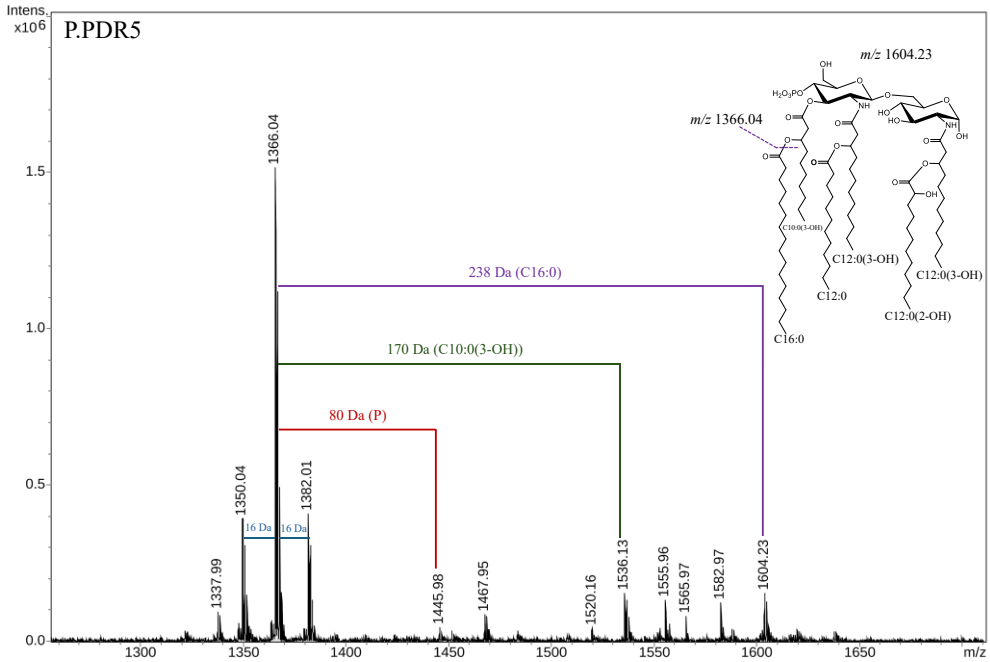


**Fig. 3.17** ESI-MS spectrum of lipid A from *P. aeruginosa* PDR5 grown under planktonic conditions (P.PDR5). The most intense glycoform corresponds to the monophosphorylated penta-acylated species at *m/z* 1366.04. Mass differences of +16 Da (hydroxyl group), +170 Da (C10:0(3-OH)), and +238 Da (C16:0) are highlighted, indicating structural variations in the acylation pattern of the lipid A molecules. The structure of the glycoform at *m/z* 1604.23 is also reported.

The nomenclature of fragment ions, including inter-residue ions such as $^{2,5}A_2$, follows the system proposed by Domon and Costello (Domon & Costello, 1988).

To determine the fatty acid distribution within the different lipid A glycoforms of *P. aeruginosa*, multi-stage ESI mass spectrometry (ESI-MS$^n$) analyses were performed on isolated ions at *m/z* 1366.04 and *m/z* 1177.87. The interpretation of the resulting spectra was carried out according to previously described fragmentation rules for glycolipids, phospholipids, and lipid A (Casillo et al., 2017; Corsaro et al., 2002; Kussak & Weintraub, 2002; C. Lee et al., 2004).

Ions arising from the cleavage of acyl groups bound at N-2 and N-2′ were of low intensity, reflecting the high stability of amide-linked fatty acids (Chan & Reinhold, 1994). The most abundant product ions were attributed to the loss of primary or secondary ester-linked fatty acids. During ESI-MS$^n$, both “charge-remote” and “charge-driven” mechanisms of fatty acid elimination are known to occur, with charge-remote fragmentation predominating (Hsu & Turk, 2000). This pathway leads to the loss of free fatty acids and the formation of a

double bond at the substitution site. Moreover, the phosphate group at O-4′ of the distal GlcN promoted the elimination of acyl groups as neutral ketene derivatives by a charge-driven mechanism, leaving a hydroxyl group at O-3′ of the nonreducing GlcN.

To elucidate the structure corresponding to the ion at *m/z* 1366.04, this precursor ion was subjected to $MS^2$ analysis. Based on chemical analysis and in accordance with previously published data (Knirel et al., 2006), the ion was assigned to a monophosphorylated, penta-acylated lipid A species bearing a C12:0(3-OH) at positions 2 and 2′, a C12:0(2-OH) as a secondary substituent on the 2-position primary chain, a C12:0 as a secondary fatty acid linked to the 3-hydroxy group of the 2′-position primary chain, and a C10:0(3-OH) at position 3′. The phosphate group is located at position 4′.

The product ion at *m/z* 1195.86 corresponded to the neutral loss of the ester-linked C10:0(3-OH) located at the 3′ position of the distal GlcN, consistent with a charge-remote process (elimination as a free fatty acid).

A further ion at *m/z* 1177.86 was attributed to dehydration (neutral loss of 18.0 Da) of the *m/z* 1195.86 species.

Another significant product ion was detected at *m/z* 910.63, identified as the diagnostic $^{2,5}A_2$ cross-ring cleavage ion derived from the precursor at *m/z* 1366.04. This fragment is highly informative, as it confirms the presence of a C10:0(3-OH) at position 3′, a C12:0(3-OH) at position 2′, a C12:0 as a secondary fatty acid linked to the 3-hydroxy group of the 2′-position primary chain, and a phosphate group at the 4′ position of GlcN II.

Notably, other significant product ions were observed at *m/z* 740.48 and *m/z* 722.48, corresponding to the $^{2,5}A_2$ ion and its dehydrated form (neutral loss of 18.0 Da), respectively. These ions further support the presence of a C12:0(3-OH) at position 2′ and a C12:0 as a secondary substituent at the same position.

Finally, the abundant ion at *m/z* 1177.86 generated at the $MS^2$ stage was selected for $MS^3$ analysis to further confirm the distribution of fatty acids. Consistent with the previous observations, the most intense fragment in the $MS^3$ spectrum was the ion at *m/z* 722.44 ($^{2,5}A_2$), originating from the precursor at *m/z* 1177.86. In addition, a significant ion at *m/z* 961.64 was detected, corresponding to the loss of the secondary C12:0(2-OH) linked to the 2-position primary acyl chain, followed by dehydration. These fragmentation events provide further structural evidence supporting the proposed structure of the parent ion at *m/z* 1366.04 (**Fig. 3.18**).

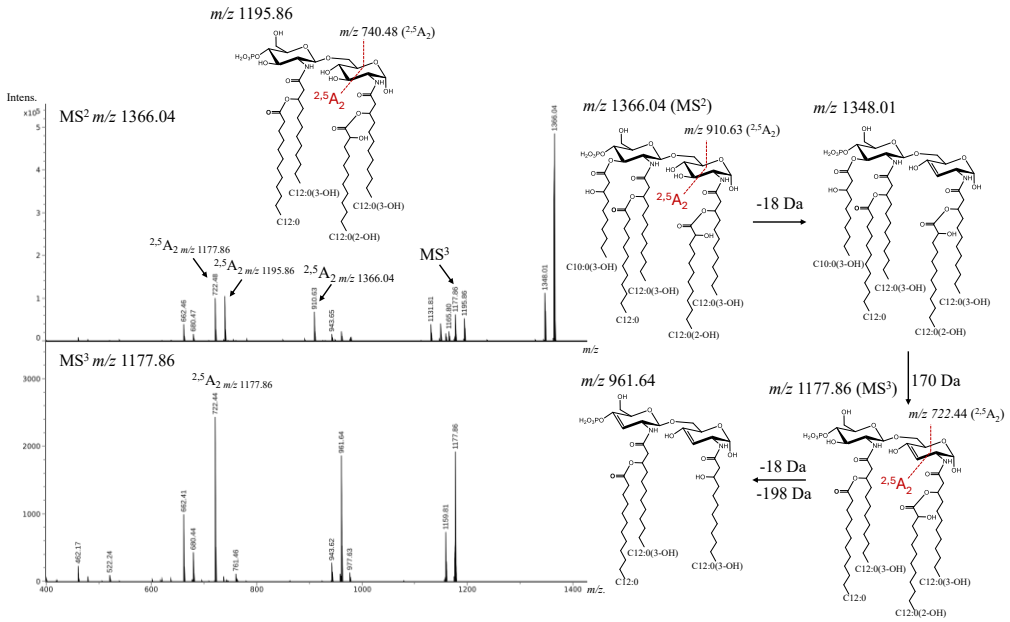


**Fig. 3.18** Negative-ion ESI-MS$^n$ spectrum of lipid A isolated from *P. aeruginosa* strain PDR5 grown under planktonic conditions (P.PDR5). The MS² spectrum of the ion at *m/z* 1366.04 and the MS³ spectrum of the fragment ion at *m/z* 1177.86 show the diagnostic fragment ions characteristic of lipid A structure. The interpretation of the main fragment ions is illustrated in the inset schemes, according to the Domon and Costello nomenclature (e.g., $^{2,5}A_2$) (Domon & Costello, 1988).

### 3.12.2 *P. aeruginosa* PDR5 biofilm

The ESI mass spectrum recorded in negative ion mode for lipid A isolated from *P. aeruginosa* PDR5 strain grown as biofilm communities revealed that the most abundant ion was detected at *m/z* 1382.05, corresponding to the monophosphorylated, penta-acylated glycoform. This species is characterized by a phosphate group at position 4′, a C12:0(3-OH) at positions 2 and 2′ each substituted with a secondary C12:0(2-OH), and a C10:0(3-OH) at position 3′. In addition, a prominent ion at *m/z* 1620.25 was assigned to the monophosphorylated, hexa-acylated glycoform, resulting from the addition of a C16:0 fatty acid (+238 Da) as a secondary substituent on the C10:0 (3-OH) at position 3′. A less intense peak at *m/z* 1552.16 was also observed, corresponding to a hexa-acylated glycoform generated by the addition of an extra C10:0 (3-OH) to the *m/z* 1382.05 species. It should be noted that the spectrum also showed the presence of glycoforms exhibiting a -16 Da mass

shift, corresponding to the lipid A species previously identified in the planktonic PDR5 strain (**Fig. 3.19**).

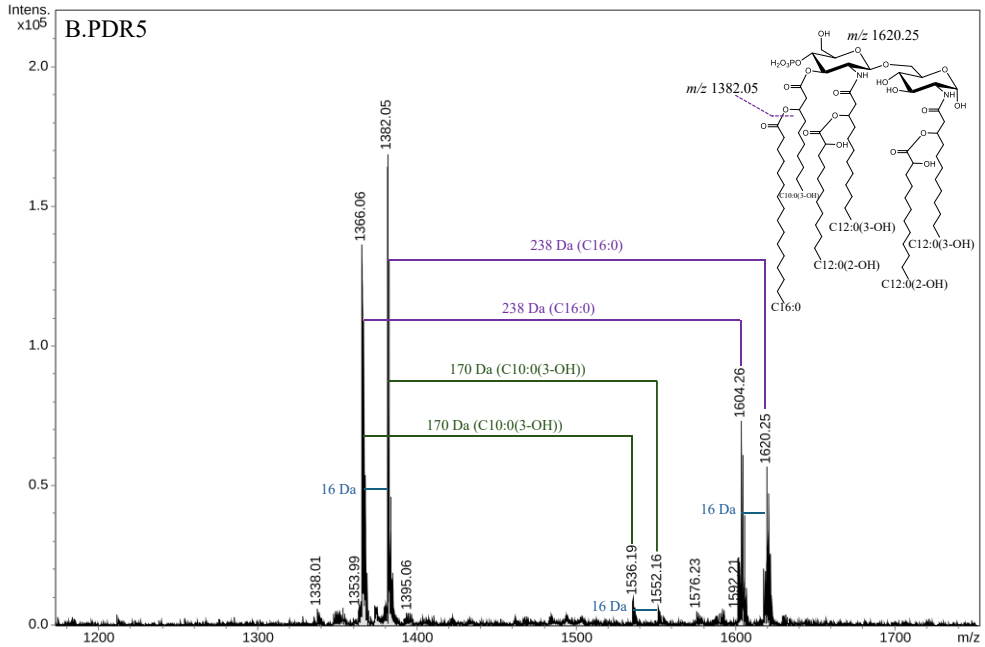


**Fig. 3.19** ESI-MS spectrum of lipid A from *P. aeruginosa* PDR5 grown under biofilm conditions (B.PDR5). The most intense glycoform corresponds to the monophosphorylated penta-acylated species at *m/z* 1382.05. Mass differences of +16 Da (hydroxyl group), +170 Da (C10:0(3-OH)), and +238 Da (C16:0) are highlighted, indicating structural variations in the acylation pattern of the lipid A molecules. The structure of the glycoform at *m/z* 1620.25 is also reported.

The monophosphorylated, hexa-acylated lipid A species detected at *m/z* 1620.25 was subjected to $MS^2$ analysis. The most intense product ion was observed at *m/z* 1364.03, corresponding to the neutral loss of a C16:0 fatty acid followed by dehydration. Additional product ions of lower intensity were detected at *m/z* 1193.86, arising from the subsequent loss of a C10:0(3-OH) fatty acid residue from the *m/z* 1364.03 intermediate. Diagnostic cross-ring cleavage ions were also identified. In particular, the $^{2,5}A_2$ ion at *m/z* 756.48 (Δ 170.0 Da) is consistent with a symmetrical acylation pattern, as both GlcNI and GlcNII carry the same acyloxyacyl substituent at positions 2 and 2′, composed of a primary C12:0(3-OH) linked to a secondary C12:0(2-OH). This ion also confirmed the presence of a phosphate group at O-4′ of GlcNII. An additional $^{2,5}A_2$ ion was detected at *m/z* 738.47, corresponding to the neutral loss of 18.0 Da relative to the *m/z* 756.48 ion.

The monophosphorylated, penta-acylated species at *m/z* 1382.05 was also analyzed by MS². A prominent fragment ion at *m/z* 1193.86 was detected, matching that observed in the MS² spectrum of the *m/z* 1620.25 precursor. Cross-ring cleavage ions were again present. The $^{2,5}A_2$ ion at *m/z* 926.62 confirmed that N-2′ of GlcNII carries an acyloxyacyl substituent consisting of an amide-linked C12:0 (3-OH) bearing a secondary C12:0(2-OH), while C-3′ is substituted with C10:0(3-OH). The $^{2,5}A_2$ ions at *m/z* 756.49 and 738.48 were also evident, as already described in the MS² spectrum of the *m/z* 1620.25 ion (**Fig. 3.20**).

MS³ fragmentation analyses yielded spectra consistent with those obtained in MS², further supporting the proposed structural assignment (data not shown). The MS² spectra of the ions at *m/z* 1604.26 and 1366.06 exhibited the same fragmentation pattern previously described for the lipid A of the PDR5 strain grown under planktonic conditions.

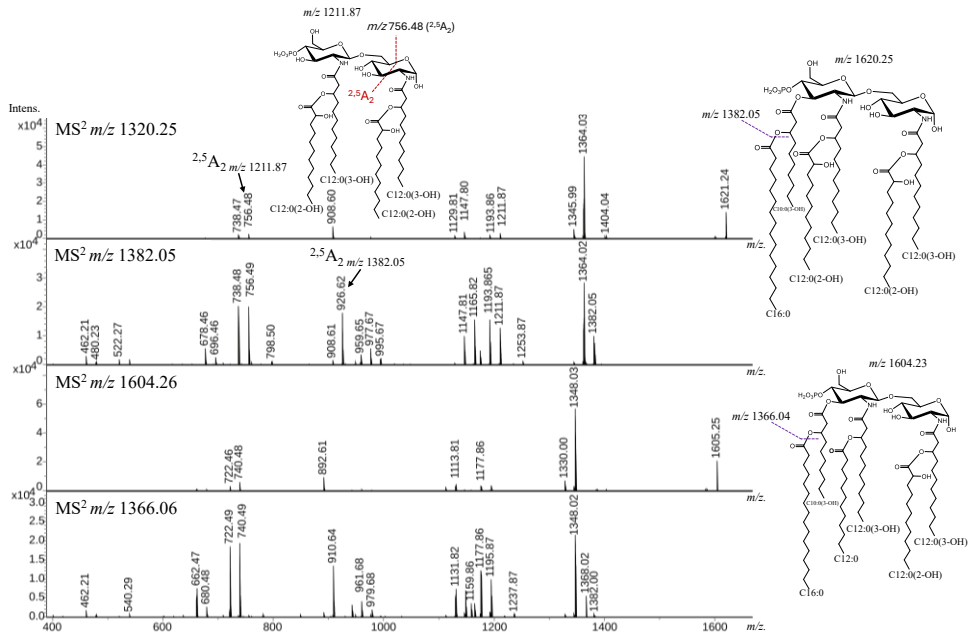


**Fig. 3.20** Negative-ion ESI-MSⁿ spectrum of lipid A isolated from *P. aeruginosa* strain PDR5 grown under biofilm conditions (B.PDR5). The MS² spectra of the ions at *m/z* 1366.06, *m/z* 1604.26, *m/z* 1383.05, and *m/z* 1620.25 show the diagnostic fragment ions characteristic of lipid A. The interpretation of the main fragment ions is illustrated in the inset schemes, according to the Domon and Costello nomenclature (e.g., $^{2,5}A_2$) (Domon & Costello, 1988).

In summary, the structural analysis of lipid A from *P. aeruginosa* PDR5 grown under planktonic (P.PDR5) and biofilm (B.PDR5) conditions revealed that the predominant species in both conditions are penta-acylated. The major ions were detected at *m/z* 1366.04 in planktonic cells and at *m/z* 1382.05 in biofilm cells. The corresponding hexa-acylated forms at *m/z* 1604.23 and 1620.25, carrying C16:0, were present at lower abundance. These species correspond to the monophosphorylated forms of the bis-phosphorylated species with *m/z* $[M-H]^-$ theoretical 1684.01 and 1700.01, highlighted in the MALDI-TOF spectrum. The 16 Da mass shift between the planktonic and biofilm penta-acylated species reflects an increased hydroxylation at position 2′, where the secondary C12:0 is replaced by a C12:0(2-OH) in biofilm cells. Despite these differences, $MS^2$ and $MS^3$ analyses confirmed the conservation of the overall acylation pattern, including symmetrical substitution at positions 2 and 2′ and the presence of a phosphate group at O-4′. Overall, biofilm growth promotes the formation of more hydroxylated lipid A species while maintaining its basic structural architecture. These conclusions were drawn by integrating the experimental data with previously reported structural analyses of *P. aeruginosa* lipid A (Knirel et al., 2006).

### 3.13 Discussion and conclusion

The persistence of *Pseudomonas aeruginosa* in hard-to-eradicate clinical settings is tightly linked to its ability to adapt to adverse environmental conditions and to remodel its molecular architecture in response to multiple selective pressures. A key determinant of this adaptive phenotype is the transition toward a biofilm-associated mode of growth, which entails profound physiological and structural changes. This lifestyle is particularly relevant in the context of cystic fibrosis (CF)-associated lung infections, where biofilms represent the prevalent bacterial organization and constitute one of the major obstacles to therapeutic eradication and infection control (Govan & Deretic, 1996; Pai et al., 2023; Uruén et al., 2020).

Within this framework, lipid A, the endotoxic component and the most conserved portion of the LPS structure, plays a central role as a modulator of host-pathogen interaction and a determinant of outer membrane integrity. Despite its typically conserved nature, our data show that biofilm growth triggers significant structural remodelling of this molecule.

MALDI-TOF and ESI-MS analyses of the WT2, MDR1, MDR5, and PDR5 strains revealed a shift of the major lipid A species from a monophosphorylated

penta-acylated structure (*m/z* $[M-H]^-$ theoretical 1365.91) in planktonic cells to its hydroxylated analogue (*m/z* $[M-H]^-$ theoretical 1381.90) under biofilm conditions, along with increased acyl heterogeneity and the emergence of hexa-acylated glycoforms. In the PDR5 strain, characterized by a pan-resistant phenotype, additional high-mass species (*m/z* $[M-H]^-$ theoretical 1700.10) carrying C16:0 acyl chains were also detected. These modifications occur while preserving the canonical diglucosamine-phosphate backbone, demonstrating a functional plasticity within a region traditionally considered structurally conserved.

From a biological and pathogenic perspective, this lipid A remodelling is highly relevant. Enhanced hydroxylation and acylation diversity can modulate TLR4/MD-2 recognition, potentially altering the magnitude and quality of the host inflammatory response. Such modulation may contribute to establishing a low-grade, persistent inflammatory state characteristic of chronic *P. aeruginosa* infections. At the same time, enrichment in acyl content is expected to reinforce the outer membrane barrier, promoting antibiotic tolerance and resistance (Michaelis & Grohmann, 2023; Parsek & Singh, 2003; Shaikh et al., 2022).

Overall, these findings highlight lipid A structural plasticity as a key adaptive mechanism employed by *P. aeruginosa* in the biofilm lifestyle. This plasticity may play a crucial role in both the establishment of chronic inflammation and the development of antimicrobial resistance. The hypotheses generated by this structural analysis will be further explored through ongoing biological assays aimed at assessing the inflammatory potential of the different lipid A structures identified.

### 3.14 Comparative monosaccharide profile of extracellular polysaccharides from planktonic and biofilm *Pseudomonas aeruginosa.*

Extracellular polysaccharides (EPSs) represent key structural and functional components of the biofilm matrix in *Pseudomonas aeruginosa*, playing a crucial role in surface adhesion, protection against environmental stresses, and persistence within the host. To investigate how EPS composition varies according to the bacterial growth mode, the production and structural features of EPS were analyzed in strains grown under planktonic and biofilm conditions. This comparative approach aimed to identify qualitative and quantitative differences in the polysaccharide fraction, providing insights into biofilm-specific adaptations and their potential impact on bacterial physiology and virulence (Colvin et al., 2012; Jennings et al., 2021).

Following the growth of *P. aeruginosa* strains PA14, WT2, WT4, MDR1, MDR5, PDR5, and PDR7 under planktonic and biofilm conditions, the culture supernatants were separated from the bacterial cells by centrifugation. The resulting pellets and supernatants were collected, and the latter were subsequently lyophilized to concentrate the extracellular material, including EPS. This preparation step was carried out for each strain and growth condition to enable downstream analyses of EPS composition and properties.

Given the pivotal role of exopolysaccharides (EPS) in biofilm organization and stability, the initial focus was placed on cultures grown under biofilm-forming conditions. To determine whether EPS release differs between planktonic and sessile lifestyles, the monosaccharide composition of the corresponding supernatants was compared. Monosaccharides were converted into acetylated methyl glycosides (AMG) and analyzed by GC-MS, with compound identification based on mass spectra and retention times relative to authentic standards.

Across all strains grown in planktonic conditions, GC-MS profiling confirmed galactose as the most abundant monosaccharide, representing 33-46% of the total sugar content depending on the strain. This trend is largely conserved under biofilm conditions, particularly in strains SB.WT2, SB.WT4 and SB.PDR7, where galactose remains the dominant sugar (43-46%).

Notable lifestyle-dependent differences emerged in specific strains. In biofilm-derived supernatants of PA14 and MDR5 (SB.PA14 and SB.MDR5), glucose becomes the predominant sugar, accounting for 50.76% and 37.38%, respectively, substantially higher than in their planktonic counterparts. These

changes suggest a marked restructuring of EPS composition during biofilm development in these strains.

A further element of variability concerns rhamnose, whose abundance differs markedly among strains and between lifestyles. Under planktonic conditions its levels range from 0% to 14.33%, while in biofilm-grown cultures it spans 0-5%. This broad variability, with some strains entirely lacking rhamnose, suggests that its incorporation into the secreted carbohydrate fraction is highly strain-dependent and not tightly linked to lifestyle, possibly reflecting differences in LPS or rhamnolipid biosynthesis or in the extent to which these components are released into the supernatant.

In addition to neutral sugars, the amino sugar glucosamine (GlcN) was detected exclusively in strain PDR5 under biofilm conditions (SB.PDR5), where it represents 1.12% of the total monosaccharide content, indicating a strain-specific modification of EPS or cell wall-derived components during sessile growth (**Table 3.8**).

Overall, the comparative analysis highlights both conserved features, such as the dominance of galactose, and strain-specific alterations, including changes in glucose enrichment during biofilm growth and pronounced variability in rhamnose content among *P. aeruginosa* strains.

**Table 3.8** Relative monosaccharide composition of strains grown in planktonic conditions and as biofilm communities. Values are expressed as mean ± standard deviation (SD) from three independent measurements. Percentages were calculated from GC-MS peak areas of methyl glycoside acetylates and normalized to the total monosaccharide content of each sample. N.D. indicates values not detected (0.00%).

| ***Strain*** | ***Rha*** | ***Rib*** | ***Man*** | ***Gal*** | ***Glc*** | ***Ino*** | ***GlcN*** |
|---|---|---|---|---|---|---|---|
| | **Molar ratio (%)** | | | | | | |
| ***Strains grown in planktonic conditions*** | | | | | | | |
| *SP.PA14* | 3.89 ± 0.25 | 8.42 ± 0.31 | 14.15 ± 0.42 | 36.28 ± 1.12 | 27.75 ± 0.87 | 9.50 ± 0.28 | N.D. |
| *SP.WT2* | 7.17 ± 0.33 | 7.65 ± 0.29 | 10.93 ± 0.35 | 37.12 ± 1.05 | 28.78 ± 0.82 | 8.35 ± 0.26 | N.D. |
| *SP.WT4* | 14.33 ± 0.52 | 7.28 ± 0.28 | 11.46 ± 0.41 | 33.10 ± 0.98 | 26.41 ± 0.79 | 7.41 ± 0.23 | N.D. |
| *SP.MDR1* | 4.73 ± 0.21 | 1.35 ± 0.10 | 15.29 ± 0.46 | 39.18 ± 1.15 | 30.69 ± 0.93 | 8.76 ± 0.27 | N.D. |

| | | | | | | | |
|---|---|---|---|---|---|---|---|
| *SP.MDR5* | N.D. | 2.61 ± 0.20 | 13.84 ± 0.39 | 41.86 ± 1.22 | 30.89 ± 0.92 | 10.79 ± 0.33 | N.D. |
| *SP.PDR5* | N.D. | N.D | 15.42 ± 0.48 | 46.16 ± 1.30 | 30.66 ± 0.91 | 7.75 ± 0.24 | N.D. |
| *SP.PDR7* | N.D. | 1.99 ± 0.15 | 12.22 ± 0.36 | 39.02 ± 1.10 | 37.78 ± 1.13 | 8.99 ± 0.27 | N.D. |
| ***Strains grown as biofilm communities*** | | | | | | | |
| *SB.PA14* | 2.72 ± 0.18 | 0.79 ± 0.07 | 8.84 ± 0.28 | 31.14 ± 0.94 | 50.76 ± 1.52 | 5.74 ± 0.17 | N.D. |
| *SB.WT2* | 3.85 ± 0.22 | 1.69 ± 0.12 | 15.28 ± 0.46 | 42.93 ± 1.29 | 33.17 ± 0.95 | 3.08 ± 0.15 | N.D. |
| *SB.WT4* | 3.96 ± 0.23 | 2.35 ± 0.16 | 13.09 ± 0.39 | 45.34 ± 1.36 | 29.47 ± 0.88 | 5.77 ± 0.18 | N.D. |
| *SB.MDR1* | 3.90 ± 0.22 | N.D. | 15.80 ± 0.47 | 39.97 ± 1.20 | 34.82 ± 1.00 | 5.48 ± 0.17 | N.D. |
| *SB.MDR5* | 2.17 ± 0.15 | 1.85 ± 0.14 | 18.15 ± 0.54 | 34.35 ± 1.03 | 37.38 ± 1.12 | 6.09 ± 0.19 | N.D. |
| *SB.PDR5* | 5.07 ± 0.27 | N.D. | 13.31 ± 0.40 | 39.06 ± 1.17 | 32.60 ± 0.97 | 8.83 ± 0.26 | 1.12 ± 0.09 |
| *SB.PDR7* | N.D. | N.D. | 12.60 ± 0.38 | 45.77 ± 1.30 | 37.76 ± 1.13 | 3.87 ± 0.16 | N.D. |

### 3.15 EPS extraction from *Pseudomonas aeruginosa* PDR5 cultivated in planktonic and biofilm growth modes

Acetic acid-mediated hydrolysis was selectively applied to the multidrug-resistant *Pseudomonas aeruginosa* strain PDR5 to recover extracellular polysaccharides (EPS) and remove residual lipopolysaccharide (LPS) contaminants. Culture supernatants from planktonic (P.PDR5) and biofilm (B.PDR5) growth conditions were treated under controlled parameters, then clarified by centrifugation to obtain a soluble fraction and an insoluble pellet. The soluble fraction was lyophilized and fractionated by size-exclusion chromatography to isolate high-molecular-weight components. These fractions were analyzed by $^{1}$H-NMR spectroscopy to determine their chemical composition. The EPS fraction displayed a profile consistent with typical

extracellular polysaccharides, with clear differences between planktonic and biofilm cultures (**Fig. 3.21**).

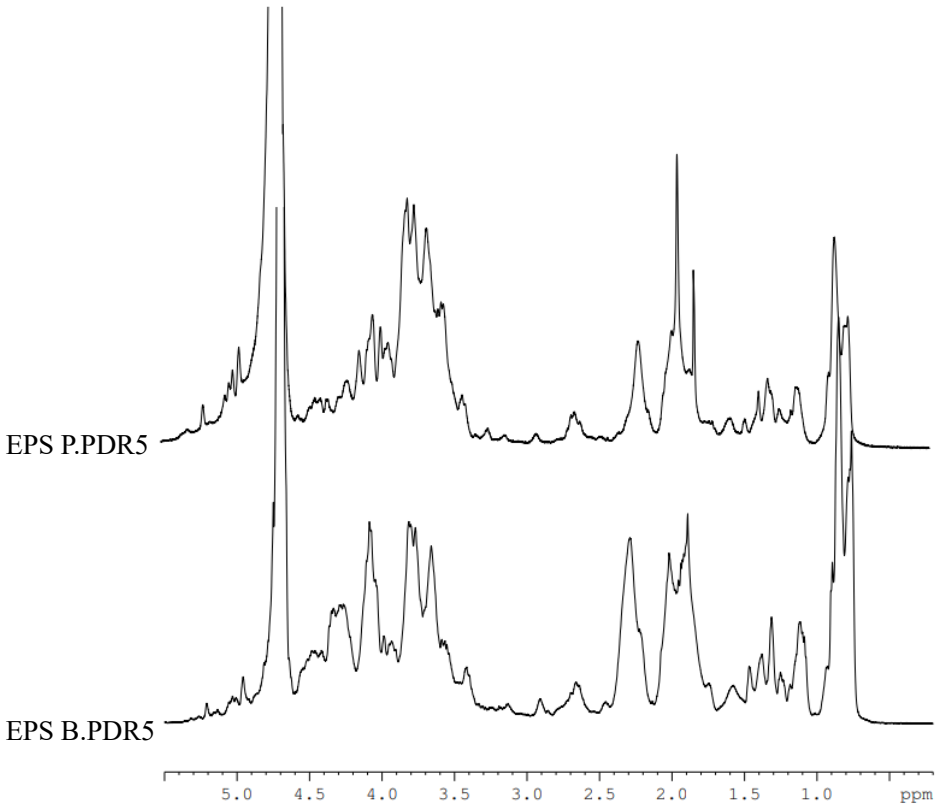


**Fig. 3.21** $^{1}$H NMR spectra of the high-molecular-weight exopolysaccharide (EPS) fraction. The upper spectrum corresponds to EPS produced by *Pseudomonas aeruginosa* PDR5 grown under planktonic conditions, while the lower spectrum corresponds to EPS from the same strain grown under biofilm conditions. Measurements were performed in $D_2O$ at 298 K using a 600 MHz spectrometer.

EPS fractions were further derivatized to acetylated methyl glycosides (AMG) and analyzed by GC-MS. The monosaccharide composition of the two samples was qualitatively similar; however, the relative abundances of individual sugars differed. Notably, fucosamine was detected exclusively in the EPS fraction derived from B.PDR5 (**Fig. 3.22**).

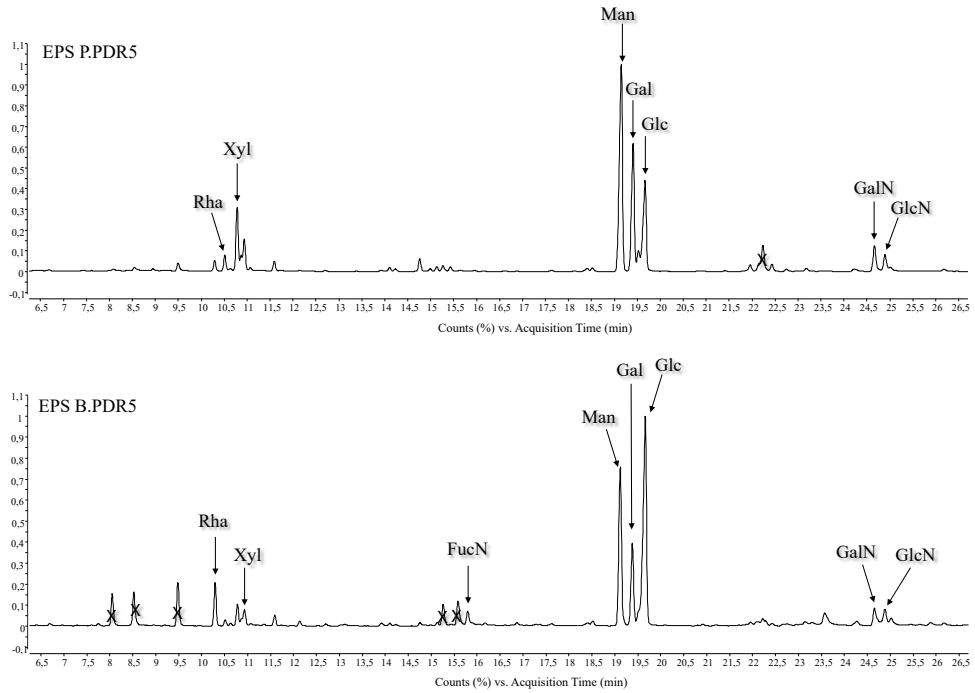


**Fig. 3.22** GC-MS chromatograms of the exopolysaccharides (EPS) produced by *Pseudomonas aeruginosa* PDR5 grown under planktonic (P.PDR5) and biofilm (B.PDR5) conditions. Detected peaks correspond to rhamnose (Rha), xylose (Xyl), fucosamine (FucN), mannose (Man), galactose (Gal), glucose (Glc), galactosamine (GalN), and glucosamine (GlcN). The X marks in the chromatograms indicate peaks corresponding to impurities

This finding suggests that sessile growth may influence the composition and structural features of EPS, potentially reflecting biofilm-specific adaptations. These observations represent a preliminary stage of the study, and further investigations will be required to achieve a more comprehensive structural and functional characterization of the EPS.

## 3.16 Discussion and conclusion

The analysis of extracellular polysaccharides (EPS) extracted from *Pseudomonas aeruginosa* PDR5 revealed clear differences between planktonic and biofilm growth conditions. Acetic acid-mediated hydrolysis combined with chromatographic purification enabled the recovery of high-molecular-weight polysaccharides largely devoid of LPS contamination, suitable for structural characterization.

$^{1}$H-NMR spectra of the isolated fractions confirmed the polysaccharidic nature of the material and highlighted distinct spectral profiles associated with each growth condition. Complementary GC-MS analyses further demonstrated that, while the monosaccharide repertoire of the EPS was qualitatively similar between planktonic and biofilm cultures, the relative sugar composition varied. Notably, fucosamine was detected exclusively in the biofilm-derived EPS, suggesting the presence of biofilm-specific structural features.

These observations point to a growth mode-dependent remodelling of EPS composition, consistent with the notion that *P. aeruginosa* modulates its extracellular matrix to adapt to environmental and physiological constraints in the biofilm state. Such modifications may influence matrix architecture, cell-cell interactions, and host-pathogen dynamics, ultimately contributing to biofilm stability, persistence, and immune evasion.

Future work will focus on a more comprehensive structural elucidation of these EPS fractions and on defining their functional roles in biofilm-associated phenotypes, including inflammatory responses and antimicrobial tolerance.

# Chapter VI

## *Analysis of glycans from the cold-adapted bacterium Psychrobacter* sp. *TAE2020*

### 4.1 Capsular polysaccharide isolation and purification

*Psychrobacter* sp. TAE2020 was grown in planktonic conditions at 15 °C, and the presence of a capsular structure around the cells was detected by transmission electron microscopy. In addition, the TEM image indicated the production of extracellular membrane vesicles (EMVs) by a blebbing mechanism (Schwechheimer & Kuehn, 2015) (**Fig. 4.1**).

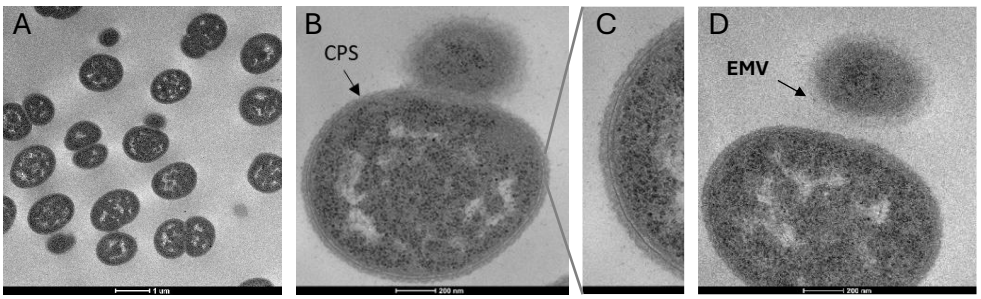


**Fig. 4.1** Transmission Electron Microscopy (TEM) analysis of *Psychrobacter* sp. TAE2020. (A) TEM micrograph of whole bacterial cells at low magnification (scale bar: 1 µm). (B) High-magnification TEM image (scale bar: 200 nm) showing the early stage of extracellular membrane vesicle (EMV) formation. (C) High-resolution TEM image of a thin section of *Psychrobacter* sp. TAE2020, highlighting the capsular polysaccharide (CPS) layer. (D) TEM micrograph (scale bar: 200 nm) displaying a cell after EMV release.

The CPS was isolated from the dried cells after PCP and phenol/water extractions (Westphal, 1965). The aqueous extract, purified from nucleic acids and proteins, was analysed by 14% DOC-PAGE (Fig. 2.1.2). Staining revealed low-molecular-weight bands corresponding to LPS and high-molecular-weight bands associated with CPS in the phenol/water extract (Lane C). The CPS was purified from LPS by mild hydrolysis followed by gel-filtration chromatography (**Fig. 4.2**).

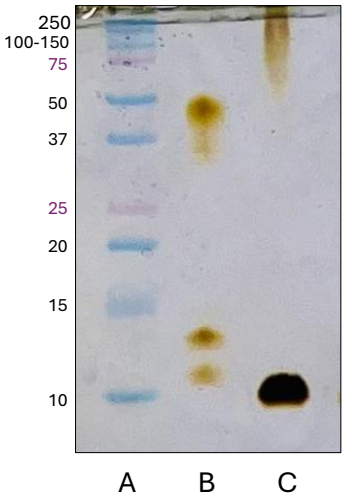


**Fig. 4.2** 14% DOC-PAGE analysis of *Psychrobacter* sp. TAE 2020 extracts, stained with Alcian blue and silver nitrate. (A) Precision Plus protein standards: (B) LPS from *Escherichia coli* O127:B8; (C) Purified aqueous phase of P/W extract.

## 4.2 Structural characterization of CPS

The GC-MS glycosyl analysis of the purified CPS disclosed the presence of 2-amino-2-deoxy-galactose (GalN) and 2,4-diamino-2,4-dideoxy-quinovose (QuiN4N, bacillosamine). In addition, the GC-MS chromatogram and the mass spectra analyses (**Fig. 4.3**) revealed another amino-sugar functionalised with pyruvic acid, also identified by NMR as a gulosamine (GulN).

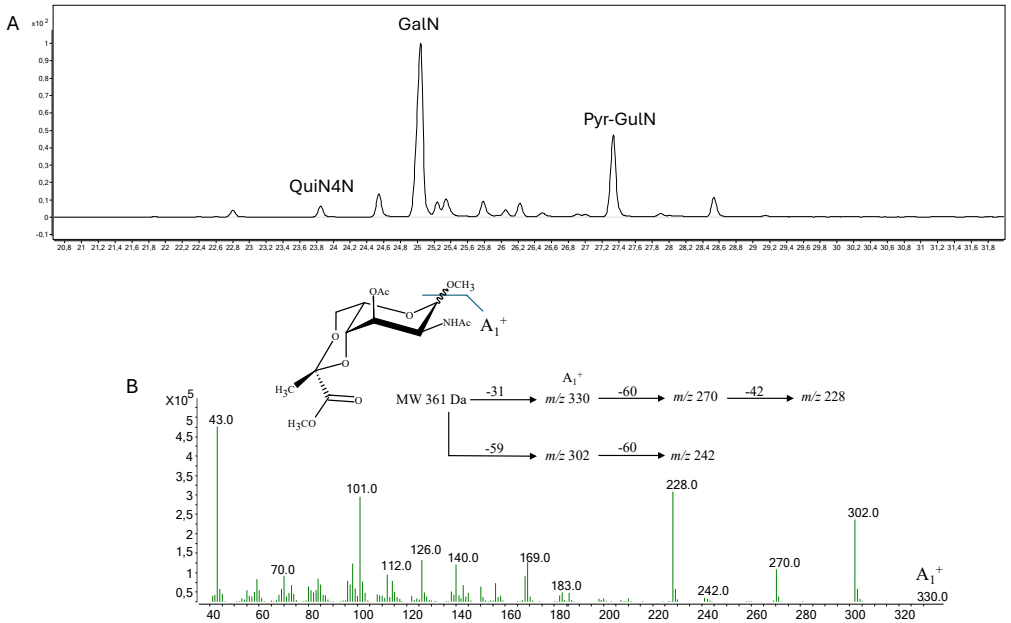


**Fig. 4.3** A) GC-MS chromatogram of AMG of CPS from *Psychrobacter* sp. TAE2020, and B) EI mass spectrum of the Pyr-gulosamine.

Preliminary inspection of NMR spectra confirmed the data obtained by GC-MS. Indeed, in the $^{1}$H-NMR spectrum (**Fig. 4.4**), four anomeric proton signals were detected in the region between δ 5.50 and δ 4.80. Furthermore, five signals of acetyl groups between 1.90 and 2.20 ppm, a pyruvic acid methyl (1.48 ppm), and a C-6 methyl of the deoxy-sugar (QuiN4N) (1.09 ppm) were identified. Finally, the presence of an unusual monosaccharide was also suggested due to its peculiar nitrogen bearing $^{13}$C carbon chemical shift at δ 47.6 ppm.

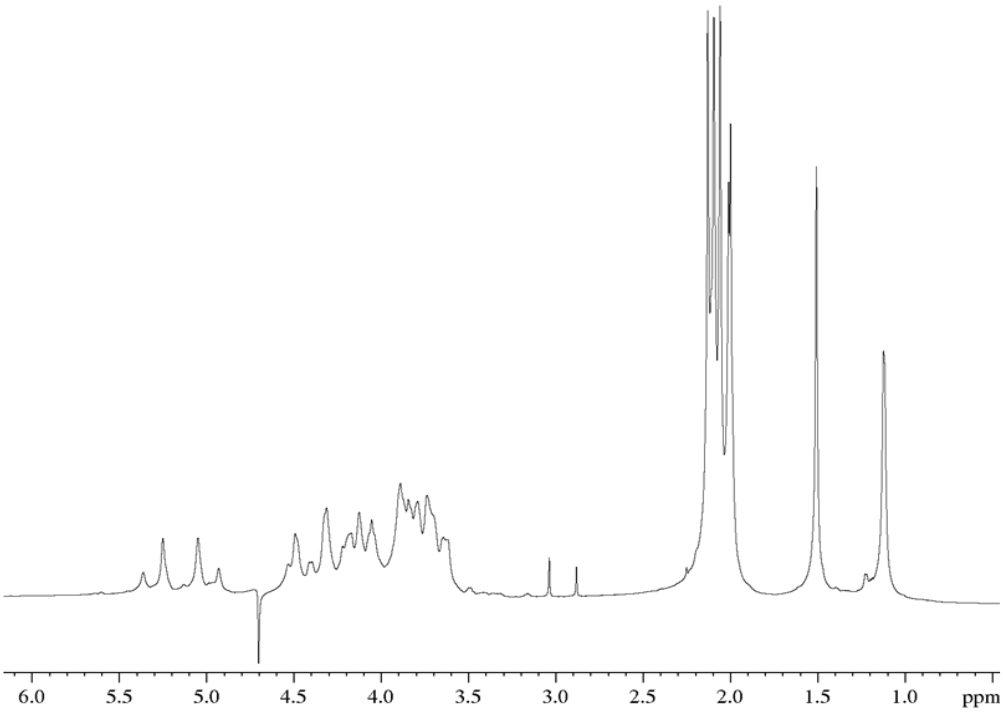


**Fig. 4.4**. $^{1}$H NMR spectrum recorded in $D_2O$ at 307 K (600 MHz) of the CPS from *Psychrobacter* sp. TAE2020.

To identify the unknown monosaccharide, the CPS was hydrolysed by triflic acid. The reaction products were desalted and then fractionated by a reversed-phase HPLC column. $^{1}$H-NMR and $^{1}$H-$^{13}$C DEPT-HSQC experiments of the obtained fractions confirmed the GalNAc and QuiNAc4NAc, as well as allowed us to identify the presence of gulosamine (GulNAc) (Zhu et al., 2006). The chemical shifts of the protons and carbons of GulNAc are shown in the **Table 4.1**.

**Table 4.1** $^{1}H$ and $^{13}C$ NMR chemical shift (ppm) assignments of α-GulNAc. Spectra were acquired in $D_2O$ solution at 307 K (600 MHz).

| | **H1**<br>**C1** | **H2**<br>**C2** | **H3**<br>**C3** | **H4**<br>**C4** | **H5**<br>**C5** | **H6**<br>**C6** |
|---|---|---|---|---|---|---|
| **α-GulNAc** | 5.06<br>97.2 | 4.22<br>45.7 | 3.73<br>68.8 | 3.75<br>68.3 | 3.98<br>68.2 | 3.69<br>60.5 |

To the best of our knowledge, this monosaccharide has never been found in natural polysaccharides.

The chemical shifts of the $^{1}H$ and $^{13}C$ NMR resonances of the sugar residues were assigned by 2D NMR experiments. The $^{1}J_{C1,\,H1}$ coupling constant values were measured with the 2D F*2*-coupled HSQC of the CPS (**Table 4.2**) and indicated that all the residues were α-configured (Bock & Pedersen, 1985).

Residue **A** with H-1/C-1 signals at δ 5.34/93.0 ppm was identified as 4-α-GalNAc. The H-2 signal correlated in the $^{1}H$-$^{13}C$ DEPT-HSQC spectrum with a nitrogen-bearing carbon at 49.5 ppm (**Fig. 4.5 B**). The H-2 proton was also shifted downfield, indicating the presence of an acyl substituent on the amino group, identified as an *N*-acetyl group. The downfield chemical shift displacement of the C-4 resonance at δ 76.8 ppm identified its substitution position (**Fig. 4.5 B**) (Bock & Pedersen, 1983; Jansson et al., 1989).

Residue **B**, with H-1/C-1 signals at δ 5.22/97.9, was identified as a 3-α-GulNAc residue. The *gulo*-configuration was suggested by the occurrence of cross-peaks from H-1 to H-3 in the TOCSY spectrum. In the COSY spectrum, starting from the H-1 at δ 5.22 ppm, the H-2 proton at δ 4.46 ppm was identified; this latter was correlated in the DEPT-HSQC experiment with a C-2 resonance at δ 47.6 ppm, typical for a *gulo*-configured residue (Kondakova et al., 2012). As for the resonances of H4/C4, H5/C5, and H6/C6, unusual values were found (**Table 4.2**). By comparing these values with those reported for the free monosaccharide (**Table 4.1**), we suggested that the values of chemical shifts fitted with the occurrence of a pyruvic acid cyclic acetal linking O-4 and O-6 of the residue (Garegg et al., 1979; Zhu et al., 2006). This finding was confirmed by the *long-range* correlation in the HMBC spectrum between the C-2 of the pyruvic acid at 100.7 ppm and the proton H-6 at δ 3.99 ppm. Furthermore, the proton methyl signal of the pyruvic acid (δ 1.48 ppm) correlated in the HMBC spectrum with its C-2 chemical shift at δ 100.7 ppm

and the C-1 carboxyl group at δ 175.0 ppm. Finally, the *(R)* absolute configuration of the pyruvic acid was identified by comparing methyl group chemical shifts with those reported by Garegg et al. (Garegg et al., 1979).
Residue **C** with H-1/C-1 signals at δ 5.02/98.3 ppm was identified as 4-α-GalNAc, as indicated by the correlation of H-2 with C-2 nitrogen at 50.1 ppm (**Fig. 4.5 B**), and the downfield chemical shift displacement of the C-4 resonance at 76.7 ppm (**Fig. 4.5 B**) (Bock & Pedersen, 1983; Jansson et al., 1989).

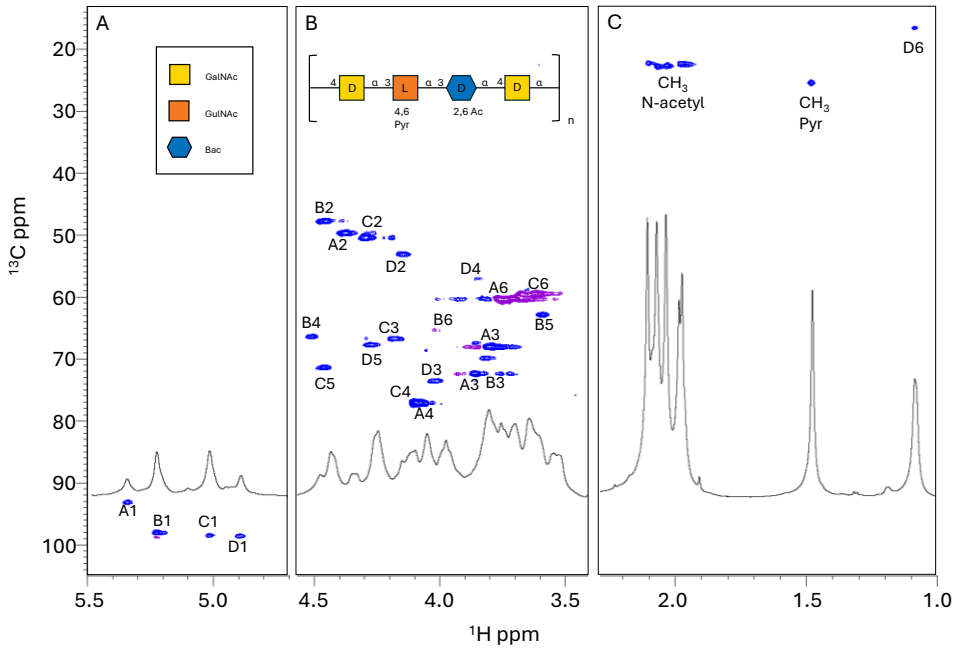


**Fig. 4.5** $^{1}H$ NMR spectrum overlayed with $^{1}H$,$^{13}C$ DEPT-HSQC (blue and purple) of A) anomeric, B) carbinolic, and C) methyl regions of CPS from *Psychrobacter* sp. TAE2020. The spectrum was recorded in $D_2O$ at 307 K at 600 MHz. The letters refer to residues as described in Table 2.1.2.

Finally, the correlations identified in COSY and TOCSY spectra suggested the *gluco* configuration for residue **D**. In detail, residue **D** with H-1/C-1 signals at δ 4.90/98.6 ppm was assigned to 2,4-diacetamido-2,4-dideoxy-quinovose (QuiNAc4NAc), since in the $^{1}H$, $^{13}C$ DEPT-HSQC spectrum H-2 and H-4 signals correlated with nitrogen-bearing carbons at δ 52.7 and 56.8 ppm, respectively, and a methyl group was found at δ 1.09/16.2 ppm (H-6/C-6) (**Fig. 4.5 C**). The downfield chemical shift displacement of the C-3 values at 73.3

ppm identified its substitution position (**Fig. 4.5 B**) (Corsaro et al., 1999). The D-configuration for GalNAc (residues **A** and **C**) and L-configuration for GulNAc (residue **B**) was obtained by GC-MS analysis of the acetylated 2-octyl glycosides. The L-configuration of GulNAc was identified using the standard L-GulNA (L-gulaminuronic acid), which was previously reduced to GulN. Finally, the D-configuration of the α-QuiNAc4NAc (residue **D**) was established based on the glycosylation effect of the $^{13}C$ NMR chemical shift values, knowing the absolute configuration of α-GulNAc and α-GalNAc) (Lipkind et al., 1988; Söderman, 1998).

**Table 4.2** $^{1}H$ and $^{13}C$ NMR chemical shifts (ppm) of CPS from *Psychrobacter* sp. TAE2020. Spectra were recorded in $D_2O$ solution at 307 K (600 MHz).

| **Residue** | **H-1**<br>**C-1**<br>**$^{1}J_{CH}$** | **H-2**<br>**C-2** | **H-3**<br>**C-3** | **H-4**<br>**C-4** | **H-5**<br>**C-5** | **H-6a,b**<br>**C-6** |
|---|---|---|---|---|---|---|
| **A** 4-α-D-GalNAc | 5.34<br>93.0<br>(180 Hz) | 4.38<br>49.5 | 3.80<br>67.8 | 4.10<br>76.8 | 3.87<br>72.0 | 3.76<br>60.3 |
| **B** 3-α-L-GulNAc4,6(*R*-Pyr) | 5.22<br>97.9<br>(180 Hz) | 4.46<br>47.6 | 3.83<br>69.3 | 4.51<br>66.1 | 3.58<br>62.6 | 4.03, 3.99<br>65.2 |
| **C** 4-α-D-GalNAc | 5.02<br>98.3<br>(176 Hz) | 4.29<br>50.1 | 4.18<br>66.4 | 4.09<br>76.7 | 4.47<br>71.2 | 3.61, 3.66<br>59.5 |
| **D** 3-α-D-QuiNAc4NAc | 4.90<br>98.6<br>(170 Hz) | 4.15<br>52.7 | 4.02<br>73.3 | 3.86<br>56.8 | 4.27<br>67.4 | 1.09<br>16.2 |
| (*R*)-Pyr | -<br>175.0 | -<br>100.7 | 1.48<br>25.2 | | | |

Acetyl groups ($CH_3$/$CH_3$/COOH): δ 2.12/22.0/174.7 ppm; δ 2.09/22.5/174.6 ppm; δ 2.06/22.4/174.9 ppm; δ 2.00/22.2/173.8 ppm.

The sequence of residues was obtained by analysing long-range scalar correlations and NOE contacts in $^{1}H$,$^{13}C$ HMBC and $^{1}H$,$^{1}H$ NOESY spectra, respectively (**Table 4.3** and **Fig. 4.6**).

**Table 4.3.** Correlations observed in the HMBC and NOESY spectra and used to determine the sequence of the residues in the CPS structure. Chemical shift values (in ppm) are reported for each interacting proton or carbon atom.

| Atom in residue | NOESY | HMBC |
|---|---|---|
| H-1 **A** (δ 5.34 ppm) | H-4 **B** (δ 4.51 ppm) | C-3 **B** (δ 69.3 ppm) |
| H-1 **B** (δ 5.22 ppm) | H-3 **D** (δ 4.02 ppm) | |
| H-1 **C** (δ 5.02 ppm) | H-4 **A** (δ 4.10 ppm) | C-4 **A** (δ 76.8 ppm) |
| C-1 **D** (δ 98.6 ppm) | | H-4 **C** (δ 4.09 ppm) |
| H-1 **D** (δ 4.90 ppm) | H-4 **C** (δ 4.09 ppm) | |

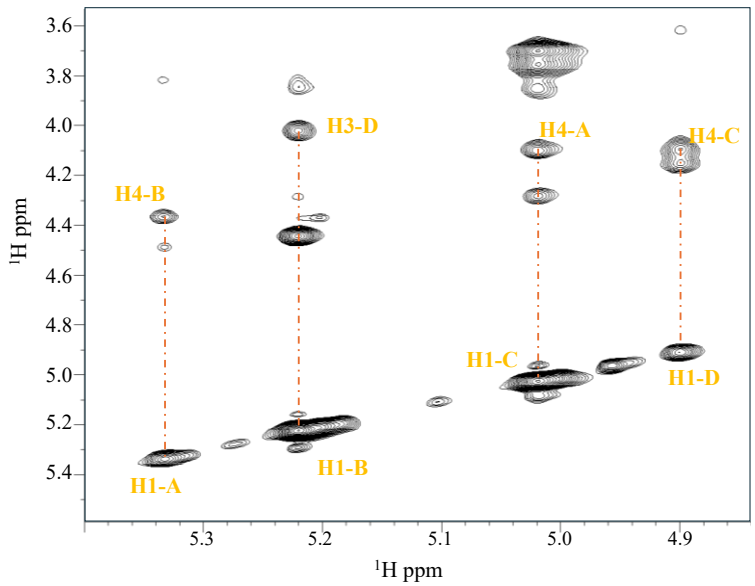


**Fig. 4.6** Selected regions of $^{1}$H,$^{1}$H NOESY NMR spectrum of the CPS from *Psychrobacter* sp. TAE2020.

The sequence of the monosaccharides in the repeating unit is **-**[**A-B-D-C**]-, and the complete structure of the CPS from *Psychrobacter* sp. TAE2020 is reported below (**Fig. 4.7**).

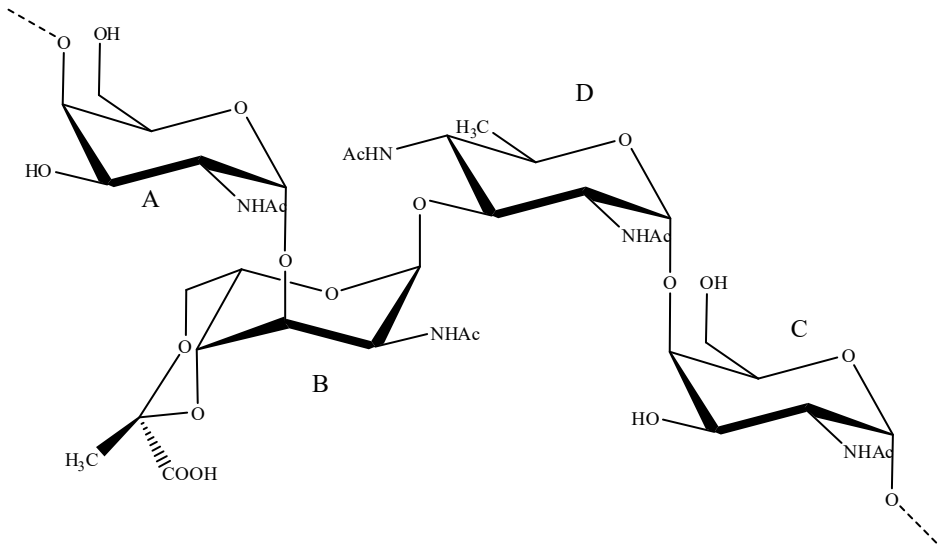


**Fig. 4.7** Repeating tetrasaccharide unit of the CPS from *Psychrobacter* sp. TAE2020.

→4)-α-D-GalNAc-(1→3)-α-L-GulNAc4,6(*R*-Pyr)-(1→3)-α-D-QuiNAc4NAc-(1→4)-α-D-GalNAc-(1→

### 4.3 CATASAN Polysaccharide Exhibits the Same Structure as CPS

The comparison of data obtained by chemical analyses and NMR spectroscopy on both CPS and the polysaccharide composing the CATASAN allowed us to assess that they share the same primary structure. Consequently, CATASAN is composed of the capsular polysaccharide (CPS), the lipopolysaccharide (LPS), and the protein *Psy*Omp38. Therefore, the definition of the structure of the CPS lays the foundation for determining how and whether the polysaccharide contributes to the biological activities of CATASAN.

The primary structure of the *Psychrobacter* sp. TAE2020 CPS is peculiar and shares the presence of the bacillosamine and the pyruvic acid with the only other CPS characterised from a *Psychrobacter* species (Kokoulin et al., 2021). The bacillosamine has also been found in another polysaccharide isolated from *Psychrobacter maritimus* 3pS (Kondakova et al., 2012), even if, in this case, a capsule identification has not been confirmed. Instead, the occurrence of the GulNAc is an intriguing feature. This monosaccharide has been chemically synthesised (Zhu et al., 2006) but, up to now, has never been found in a polysaccharide structure, unlike the corresponding uronic acid, the gulaminuronic acid (Di Guida et al., 2020). Interestingly, D-gulosamine was only found attached to a lactam ring in streptothricin antibiotics (Gan et al., 2011).

### 4.4 Dimension and molecular mass

The physico-chemical properties of the CPS in aqueous solution were thoroughly investigated by means of Dynamic Light Scattering (DLS) and Static Light Scattering (SLS) analyses in order to obtain detailed information on its molecular organization and aggregation behavior. DLS measurements revealed that at a CPS concentration of 1.8 mg/mL, the hydrodynamic radius (Rh) of the system was approximately 5.6 nm, with a polydispersity index (PDI) close to 0.5, indicating a rather homogeneous size distribution. The weight-average molecular mass was calculated to be around $3.16 \times 10^4$ g/mol (**Fig. 4.8 A**), a value that is fully consistent with those previously reported for the capsular polysaccharide of *Shewanella vesiculosa* (Casillo et al., 2022) as well as for Mannan (Casillo et al., 2021). These results strongly support the hypothesis that, at this concentration, the CPS mainly exists in solution as isolated polymer chains in a non-aggregated state, confirming the absence of significant supramolecular organization under these conditions.

Further structural insights were obtained through SLS experiments, which allowed us to evaluate the molecular weight and second virial coefficient of a distinct macromolecular population present in the system. Specifically, light scattering data revealed the occurrence of an aggregate species characterized by a significantly larger hydrodynamic radius of about 360 nm (PDI = 1.6) (**Fig. 4.8 B**). By carefully measuring the scattering intensity of the sample, the solvent, and an appropriate reference, and subsequently generating the corresponding Zimm plot (**Fig. 4.8 C**) (Perfetti et al., 2020a), the weight-average molecular mass of this aggregate population was determined to be $(2.22 \pm 0.03) \times 10^7$ g/mol. This value corresponds to approximately $2.66 \times 10^5$ individual CPS chains. The second virial coefficient was measured as $(2.78 \pm 0.02)$ cm³/g. The positive sign of this coefficient clearly indicates favorable interactions between the polysaccharide and the solvent, reflecting good hydration and non-ideal but repulsive behavior of the macromolecules in solution. Overall, the obtained results are in excellent agreement with those typically acquired through SEC-MALLS analysis (Macarie et al., 2017), confirming both the reliability of the experimental approach and the intrinsic solution properties of the CPS.

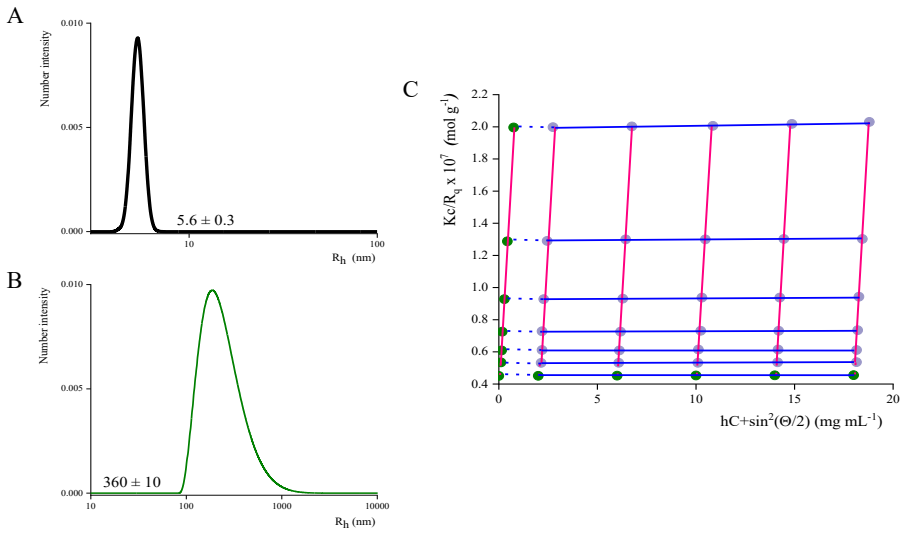


**Fig. 4.8** (A) Number hydrodynamic radius distribution of a single chain of CPS, (B) number of hydrodynamic radius distribution of CPS aggregate, and (C) Zimm plot of CPS aggregate.

### 4.5 Anti-adhesive and antibiofilm activity against *S. epidermidis* strains

As mentioned above, *Psychrobacter* sp. TAE2020 produces bioactive compounds with both anti-adhesive and antibiofilm properties, which are effective against two different *Staphylococcus epidermidis* strains. Subsequent studies identified the CATASAN complex as the main active component responsible for this effect. In particular, CATASAN was shown to interfere with all critical stages of staphylococcal biofilm development, including initial attachment, biofilm maturation, and stabilization of the extracellular matrix (D'Angelo et al., 2022). This observation suggested that specific structural components of the CATASAN complex might play distinct and measurable roles in its overall biological activity.

To investigate the contribution of the capsular polysaccharide (CPS) within the CATASAN complex, both purified CPS and the CPS–LPS mixture were systematically evaluated for their anti-adhesive and antibiofilm effects against *S. epidermidis* RP62A and *S. epidermidis* O-47. These strains were selected as representative models for staphylococcal biofilm formation due to their well-characterized phenotypic profiles and relevance in medical device-associated infections.

A surface coating assay was employed to assess the ability of CPS and CPS–LPS to reduce bacterial attachment to abiotic surfaces (**Fig. 4.9 A**). In this experimental setup, the test compounds were applied as coatings before bacterial exposure, thereby enabling the evaluation of their impact on the initial adhesion phase. In parallel, the potential of the same fractions to inhibit biofilm formation was investigated by adding CPS or CPS–LPS to the staphylococcal growth medium at the beginning of the incubation period, followed by quantification of the biofilm formed after cultivation (**Fig. 4.9 B**). This approach allowed us to assess the capacity of these polysaccharidic

components to disrupt biofilm development during the earliest stages of colonization and matrix establishment.

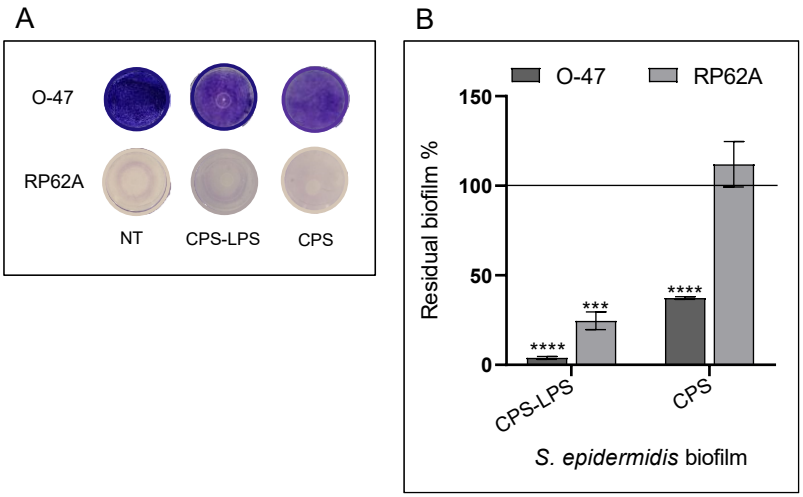


**Fig. 4.9** (A) Biofilm formation by *S. epidermidis* O-47 and *S. epidermidis* RP62A in polystyrene 24-well microtiter plates coated with CPS-LPS, and CPS (tested at 1 mg/mL). (B) Effect of CPS-LPS, and CPS (0.5 mg/mL) on biofilm formation. Each data point represents the mean ± SD of six independent samples. The results are presented as the percentage of biofilm formed in the presence of CPS-LPS, and CPS compared to untreated bacteria (100%). Biofilm formation was considered unaffected within the range of 90–100%. Differences in mean absorbance were compared to the untreated control and considered significant when $p < 0.05$ (*** $p < 0.001$, **** $p < 0.0001$) according to ANOVA.

As reported in **Fig. 4.9 A**, the CPS did not exhibit anti-adhesive properties against *S. epidermidis* strains but effectively inhibited biofilm formation (**Fig. 4.9 B**). Notably, the CPS demonstrated strain-specific antibiofilm activity, effectively inhibiting biofilm formation for the *S. epidermidis* O-47 strain (**Fig. 4.9 B**). Interestingly, the antibiofilm activity is strongest in the case of CPS-LPS. To further investigate the structure-activity relationship of the capsular polysaccharide, its antibiofilm activity was evaluated after treatment with hydrochloric acid (HCl). The results revealed that hydrochloric acid treatment, which caused partial CPS depolymerisation, significantly impaired the capsular antibiofilm activity (**Table 4.4**). The presence of a polydispersed system in solution, with evidence of two populations having a $R_h$ of approximately 9 and 110 nm, respectively, from which it is possible to

determine the molecular weight ($M_w$) relative to that of the CPS before HCl treatment, could justify the partial CPS depolymerisation.

**Table 4.4** Structure-activity relationships of capsular polysaccharides from *Psychrobacter* sp. TAE2020.

| Samples | | $M_w$ (g/mol) | $R_h$ (nm) | PDI | Emulsifier activity (%) | Biofilm reduction (%) |
|---|---|---|---|---|---|---|
| **CPS** | | (2220 ± 300) x $10^4$ | 360 ± 10 | 1.6 | 66% | 63% |
| **CPS (HCl)[a]** | * | (5.25 ± 0.06) x $10^4$ | 9 ± 2 | 0.4 | <5% | <10% |
| | ** | (678 ± 50) x $10^4$ | 110 ± 5 | 1.8 | | |

[a]After treatment with HCl, the suspension system was found to be polydisperse, with two populations indicated with * and **, respectively.

This suggests that the structural integrity of CPS is crucial for its antibiofilm function. Then, the effect of the CPS on *S. epidermidis* O-47 biofilms was further analysed using CLSM to examine biofilm structure and cell integrity with the LIVE/DEAD® Biofilm Viability Kit (**Fig. 4.10 A**). By this assay, the viable cells appear green, and dead (cell membrane-damaged) bacteria appear red (**Fig. 4.10 A**). CLSM analysis demonstrated that CPS reduces *S. epidermidis* biofilm formation, and no dead cell zones were observed. Furthermore, COMSTAT analysis suggested that the biomass and average thickness of biofilms treated with CPS were lower compared to untreated samples (**Fig. 4.10 B-C**). Conversely, an increased roughness coefficient was observed in treated biofilms, indicating that the treatment led to a more unstructured and heterogeneous biofilm (**Fig. 4.10 D**).

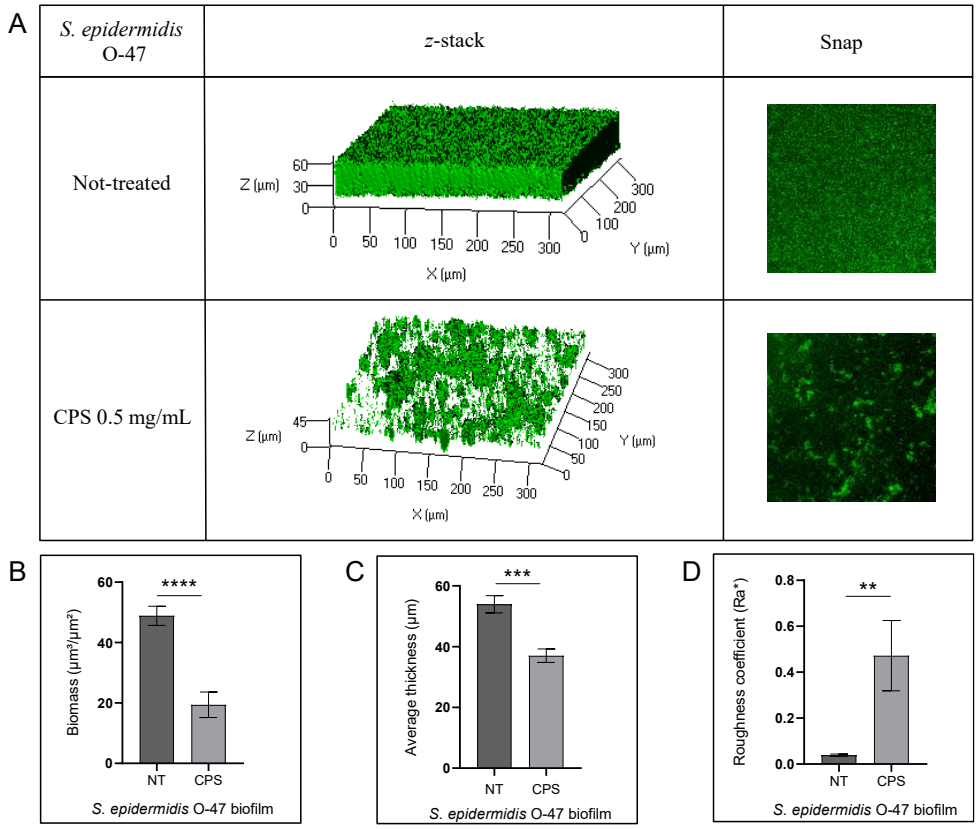


**Fig. 4.10** (A) CLSM analysis of biofilms formed in the absence and presence (0.5 mg/mL) of CPS. (B-C) COMSTAT quantitative analysis of biomass and average thickness of treated (CPS) and untreated (NT) biofilms. (D) COMSTAT quantitative analysis of the roughness coefficient of treated and untreated (NT) biofilms. Bi-dimensional (SNAP) and Three-dimensional (*z*-stack) biofilm structures were obtained using the LIVE/DEAD® Biofilm Viability Kit. Differences in mean absorbance were compared to the untreated control and considered significant when $p < 0.05$ (** $p < 0.01$, *** $p < 0.001$, **** $p < 0.0001$) according to the Student's t-test.

## 4.6 Characterisation of bio-emulsifier properties

D'Angelo et al. previously demonstrated that the emulsifying ability of *Psychrobacter* sp. TAE2020 was associated with the CATASAN complex. To assess if this emulsifying capacity was related to the polysaccharides, the emulsifier ability of the purified CPS and CPS-LPS fractions was evaluated. The samples were tested with Dectol, and the emulsification index ($E_{24}$) measured after 24 hours suggested that both CPS-LPS and CPS exhibit emulsifying activity (**Table 4.4**, **Fig. 4.11**).

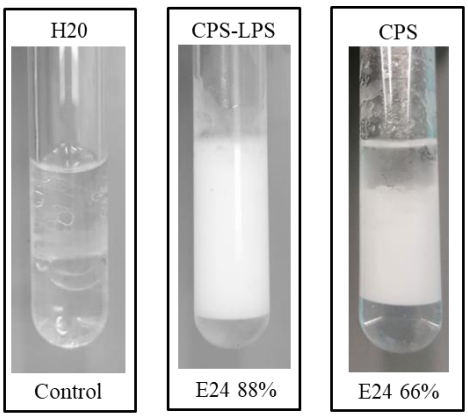


**Fig. 4.11** Emulsification index ($E_{24}$) of capsular in combination with lipopolysaccharides (CPS-LPS) and purified capsular (CPS) (tested 1 mg/mL). Dectol emulsion with water is reported as the negative control. The solutions were mixed with Dectol (1:2 v/v) and analyzed after 24 h.

In particular, the CPS-LPS emulsion remained stable for over 6 months at room temperature (data not shown), while the CPS emulsion remained stable for more than 1 month under the same conditions (data not shown). This result demonstrates that the emulsifying properties attributed to the CATASAN complex are mainly due to the capsular polysaccharide and the LPS present in the complex. Finally, as for anti-biofilm activity, the depolymerisation determined the lack of activity (**Table 4.4**).
Future studies will be dedicated to further investigating the emulsifying properties of the CPS-LPS sample to explore possible applications.

## 4.7 Adhesion Properties and antibiofilm ability of prepared CPS-coated liposomes

Recent studies have shown that polysaccharide coatings on liposomes, such as hyaluronic acid and chitosan, can prolong liposome circulation time in the bloodstream and reduce their biodegradability (Li et al., 2017; Peng et al., 2023; Yu et al., 2021). Moreover, the intrinsic mucoadhesive properties of these polymers increase the residence time of the formulations (Choi et al., 2012; Karn et al., 2011).

The capacity of capsular polysaccharides to adhere to inorganic and organic surfaces, including polystyrene and liposomal membranes, has been previously demonstrated for *Shewanella vesiculosa* (Casillo et al., 2022). Based on this evidence, the interaction between the anti-biofilm CPS from *Psychrobacter* sp. TAE2020 and lipid vesicles was assessed using SAXS measurements. This technique allows the determination of the preferential localization of the polysaccharide at the hydrophobic or hydrophilic interface of the vesicles through the analysis of the pair distance distribution function P(r) derived from experimental SAXS data.

SAXS analyses were performed by gradually increasing the amount of CPS applied to the lipid membrane (5, 10, 15, 20, 25, 30, and 35 µg) (**Fig. 4.12**). The progressive addition of CPS enabled the evaluation of its binding capacity and the identification of structural changes in the liposome organization upon polysaccharide association.

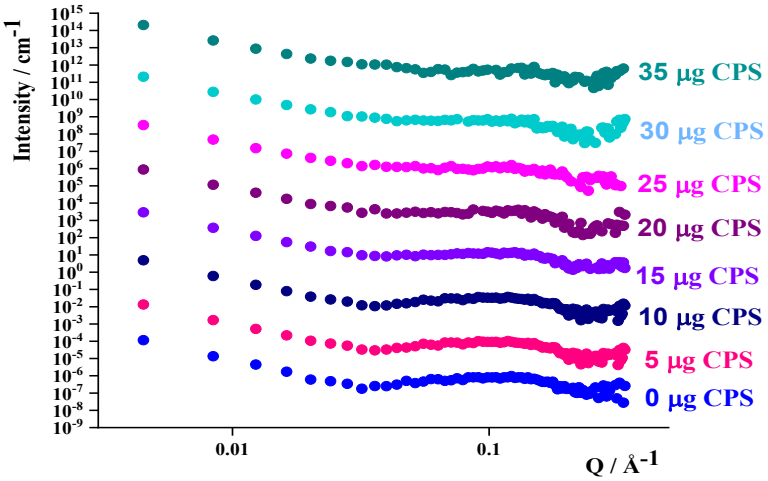


**Fig. 4.12** SAXS measurements of lung surfactant lipid vesicles with increasing CPS amount.

All scattering profiles obtained were consistent with lamellar vesicle structures (Ober et al., 2022). The distribution curve of the lipid vesicles displayed the typical behaviour of a unilamellar organization, showing a head-to-head

distance of approximately 45 Å (**Fig. 4.13 A**, blue curve), in agreement with the expected phospholipid bilayer arrangement (Vitiello et al., 2024). This head-to-head distance remained constant across all systems analysed. Upon CPS addition, however, new peaks at high *q* values appeared, corresponding to the surface decoration of the vesicles with CPS sugar moieties. The formation of this corona led to a shift in the head-to-head distance, increasing from 45 Å at 5 μg of added CPS to values exceeding 100 Å at higher concentrations (**Fig. 4.13 A-B**). The emergence of multiple maxima in the distribution curves and the marked increase in head-to-head distances provide clear evidence of the CPS adhering to the membrane surface and promoting the formation of multilayered structures.

Moreover, as the CPS concentration increased, the experimental SAXS profiles exhibited a less pronounced minimum, which is indicative of a direct interaction between the polysaccharide and the hydrophobic region of the lipid bilayers (**Fig. 4.13 A-B**).

Finally, ζ-potential measurements were performed to assess whether membrane–CPS interactions are mainly driven by electrostatic forces. As shown in Fig. 2.1.13C, both the membrane, which mimics lung surfactant, and the CPS exhibit negative surface charges, with values of −62.1 ± 0.7 mV and −34 ± 2 mV, respectively. Despite their similar net charge, interactions between negatively charged systems have already been documented, for example, between superparamagnetic nanoparticles and albumin (Russo Krauss et al., 2020) and between *S. vesiculosa* CPS and negatively charged liposomes (Casillo et al., 2022). In line with these findings, the ζ-potential became progressively less negative with increasing CPS concentration, shifting from approximately −61 mV (similar to the vesicle alone) to around −49 mV. This trend suggests that CPS adhesion to the liposomal surface is likely mediated by hydrogen bond formation.

Overall, the results obtained from *Psychrobacter* sp. TAE2020 CPS and CPS-coated vesicles support the hypothesis that the negative charge density of polysaccharides plays a crucial role in modulating biophysical interactions. This property may contribute to the broad-spectrum antimicrobial activity of such molecules, as also proposed by Joaquín Bernal-Bayard and co-authors (Bernal-Bayard et al., 2023).

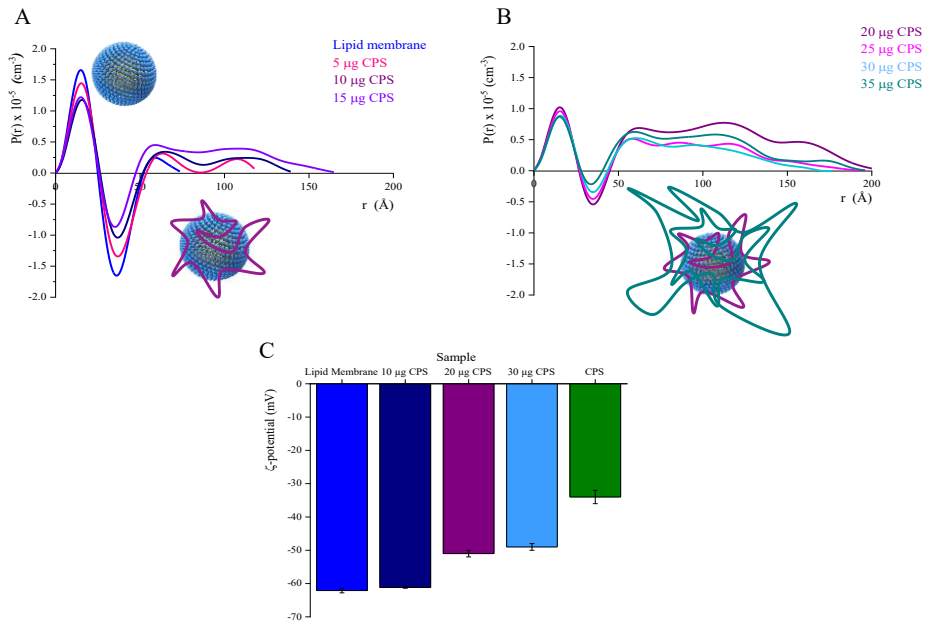


**Fig. 4.13** (A - B) P(r) curve with vesicle, and vesicles with 10 and 35 µg of CPS cartoon, and (C) ζ-potential of lung surfactant lipid vesicles with increasing CPS amount.

Since CPS shows the ability to adhere to liposomes, the antibiofilm activity of uncoated liposomes and CPS-coated liposomes against two *S. epidermidis* strains was evaluated (**Fig. 4.14**). As shown in **Fig. 4.14 A**, plain liposomes can impair biofilm formation by *S. epidermidis* O-47. Notably, CPS-coated liposomes (referred to as CPS-liposomes) exhibited enhanced antibiofilm activity against strains. The ability of CPS-liposomes to significantly reduce biofilm formation by *S. epidermidis* O-47 reveals their potential as a functional component in the development of CPS-based drug delivery systems.

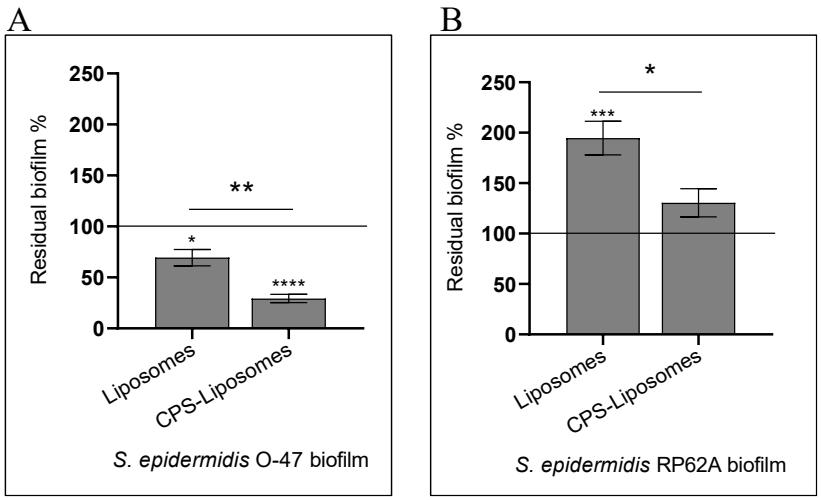


**Fig. 4.14** (A) Biofilm formation by *S. epidermidis* O-47 and (B) *S. epidermidis* RP62A in 24-well polystyrene plates coated with liposomes or CPS-coated liposomes (0.25 mg/mL, normalized for liposome content). Data are expressed as the percentage of residual biofilm compared with untreated bacteria (100%). Each bar represents the mean ± SD of four independent experiments. Statistical significance was determined by ANOVA for comparisons with untreated control (*$p < 0.05$, ***$p < 0.001$, ****$p < 0.0001$; indicated above the bars) and by Student's t-test for comparisons between liposomes and CPS-liposomes (*$p < 0.05$, **$p < 0.01$; indicated by horizontal lines).

## 4.8 Purification of EMVs from *Psychrobacter* sp. TAE2020

TEM image indicated the production of extracellular membrane vesicles (EMVs) by a blebbing mechanism (**Fig. 4.15**).

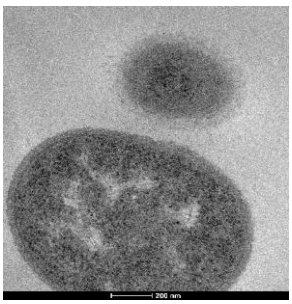

**Fig. 4.15** High-magnification TEM image (scale bar: 200 nm) showing the release of extracellular membrane vesicles (EMVs) from the bacterial surface

*Psychrobacter* sp. TAE 2020 was grown in planktonic conditions for different times of growth (24-72 hours). To isolate the vesicles, the cells were precipitated by cultures and the supernatants filtered through a

polyvinylidene difluoride filter. The supernatants, collected after 24, 48, and 72 hours of bacterial growth, were centrifuged to sediment the vesicular fraction into a pellet suspended in PBS to give the crude vesicles. DLS measurements revealed that the main population showed a hydrodynamic radius for the purified EMVs ranging from 170 to 80 nm.

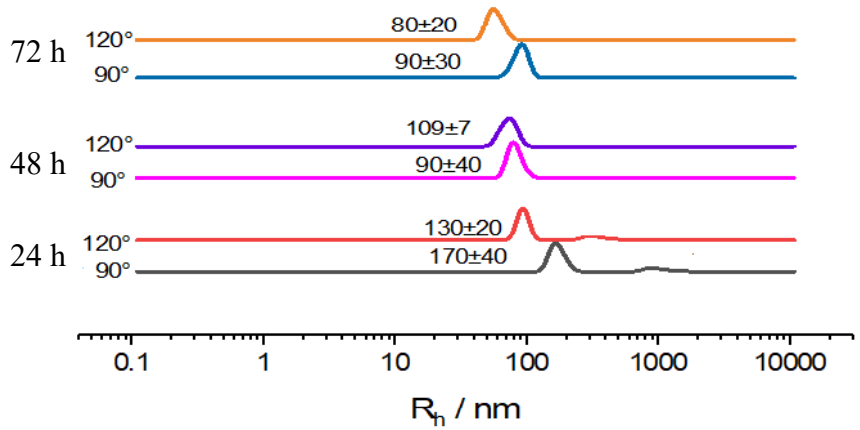


**Fig. 4.16** Hydrodynamic radii distribution measured by DLS of purified EMV at 24, 48, and 72 hours.

The surface glycans of EMVs will be extracted and characterized to confirm that the CPS surrounding the EMVs share the same structure of that found on cells. Simultaneously, since CPS isolated from *Psychrobacter* sp. TAE showed interesting anti-biofilm activity (see paragraph 6.7), the isolated EMVs will be tested for anti-biofilm activity against *S. epidermidis* O47.

## 4.9 Discussion and conclusion

A novel capsular polysaccharide (CPS) has been isolated from the cells of *Psychrobacter* sp. TAE2020 and structurally characterized. The repeating unit consists exclusively of aminosugars with hydrophobic substituents, with the exception of pyruvic acid, which carries a negative charge. The high degree of acetylation, together with the low number of free hydroxyl groups, is likely responsible for the strong intermolecular aggregation of the polysaccharide chains and their ability to adhere to liposomal membranes.

Notably, this study provides the first evidence that the capsular polysaccharide, in combination with lipopolysaccharide (LPS), plays a crucial role in the emulsifying activity of the CATASAN complex. Further investigation will focus on defining the relative contribution of each component to this activity.

The ability of CPS to interfere with *Staphylococcus epidermidis* biofilm formation may be linked to its emulsification capacity. This is further supported by the CPS-LPS preparation, which shows enhanced emulsifying properties and greater antibiofilm activity. CLSM analyses of *S. epidermidis* biofilms treated with CPS revealed not only a reduction in biofilm biomass but also a clear alteration of biofilm architecture, without affecting bacterial cell viability. Finally, the strong adhesion of CPS to liposomes highlights a promising strategy for the development of anti-biofilm delivery systems based on this polymer. Moreover, the recent observation of extracellular membrane vesicle (EMV) release by *Psychrobacter* sp. TAE2020 opens a new line of investigation aimed at evaluating the potential role of these vesicles in biological and antibiofilm activities, as well as their possible application as a drug delivery system.

## 4.10 Isolation and purification of the lipopolysaccharide from *Psychrobacter* sp. TAE2020

Extraction of dried bacterial cells using the PCP method (Galanos et al., 1969) yielded 43 mg of lipopolysaccharide (LPS), corresponding to 1.2% of the dry biomass. The purified LPS was analyzed by PAGE according to the Laemmli system (Laemmli, 1970), using sodium deoxycholate (DOC) as detergent, as previously described (Carillo et al., 2015). Silver staining, performed following the procedure of (Tsai & Frasch, 1982a), revealed the presence of a rough-type LPS profile (**Fig. 4.2**).

## 4.12 Sugar composition

GC-MS analysis of acetylated methyl glycoside (AMG) derivatives allowed the identification of the monosaccharide composition of the LPS. The results indicated glucose (Glc) as the major sugar component, along with detectable amounts of glucosamine (GlcN) and 3-deoxy-D-manno-oct-2-ulosonic acid (Kdo), the latter being a distinctive feature of bacterial LPS (**Fig 4.17**).

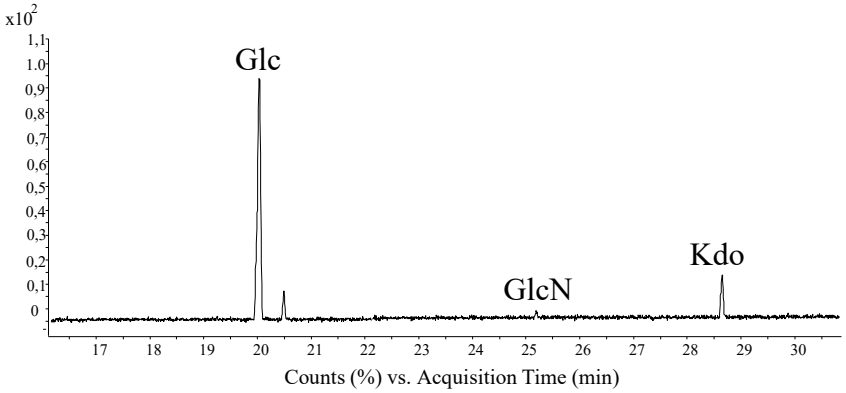


**Fig. 4.17** GC chromatogram of the acetylated methyl glycosides (AMG) derived from LPS. Peaks corresponding to Rha (rhamnose), Glc (glucose), GlcN (glucosamine), and Kdo (3-deoxy-D-*manno*-oct-2-ulosonic acid) are highlighted.

## 4.13 Lipid A

The lipopolysaccharide fraction was subjected to mild acid hydrolysis with 1% aqueous acetic acid. Following centrifugation of the reaction mixture, lipid A was recovered as the insoluble fraction, subsequently washed twice with water,

and freeze-dried. The resulting material was further purified by passage through a Celite column, yielding the final lipid A preparation**.**

Analysis of the sugar composition of lipid A revealed the presence of glucosamine as the only monosaccharide. GC-MS analysis of fatty acid methyl ester derivatives detected decanoic acid C10:0, significant amounts of 3-hydroxydodecanoic acid C12:0 (3-OH) and 3-hydroxytetradecanoic acid C14:0 (3-OH) (**Fig. 4.18**).

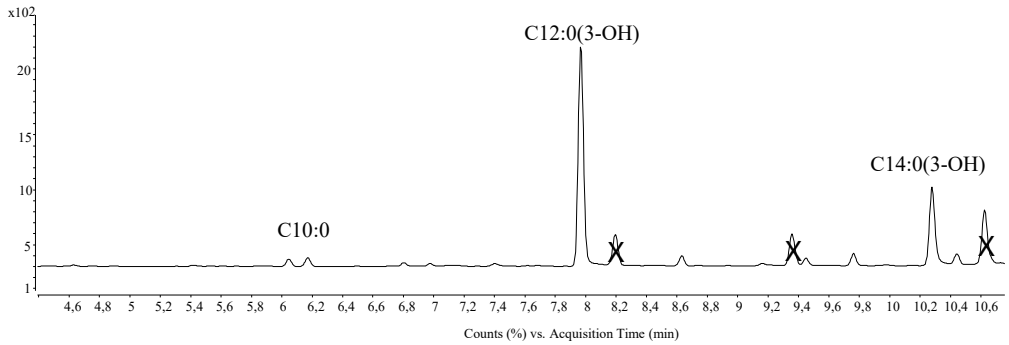


**Fig. 4.18** GC-MS chromatogram of LPS fatty acid methyl esters (FAMEs). The analysis highlights the presence of decanoic acid (C10:0), 3-hydroxydodecanoic acid (C12:0(3-OH)), and 3-hydroxytetradecanoic acid (C14:0(3-OH)). The X marks in the chromatograms indicate peaks corresponding to impurities.

## 4.14 MALDI-TOF mass spectrometry analysis of lipid A

The MALDI-TOF mass spectrum acquired in reflectron negative ion mode revealed a complex pattern of signal clusters corresponding to distinct glycoforms (**Table 4.5**). Four main species (**M1**-**M4**) were identified, representing tri-, tetra-, hexa-, and hepta-acylated lipid A forms.

The heterogeneity within each cluster is mainly due to variations in fatty acid chain length, with systematic differences of ±28 Da attributable to the replacement of C14:0(3-OH) with C12:0(3-OH). Additional heterogeneity is observed in the form of mono- versus bisphosphorylated species (±80 Da) (**Fig. 4.19**).

The tri-acylated monophosphorylated species **M1** was observed at *m/z* 969.55 (Calculated Mass $[M-H]^-$ 969.58 Da), and assigned the composition $GlcN_2P[C12:0(3\text{-}OH)]_2[C10:0]$.

The tetra-acylated monophosphorylated species **M2** was observed at *m/z*

1195.75 (Calculated Mass $[M-H]^-$ 1195.77 Da), with the composition $GlcN_2P[C14:0(3\text{-}OH)][C12:0(3\text{-}OH)]_2[C10:0]$. Its bisphosphorylated analogue was detected at *m/z* 1275.75 (+80 Da).
The hexa-acylated bisphosphorylated species **M3** was detected at *m/z* 1599.95, consistent with the composition $GlcN_2P_2[C12:0(3\text{-}OH)]_4[C10:0]_2$. Variants differing by -28 Da were assigned to substitution of C14:0(3-OH) with C12:0(3-OH). The monophosphorylated form was also observed at *m/z* 1519.95 (-80 Da).
Finally, the hepta-acylated bisphosphorylated species **M4** was detected at *m/z* 1754.14, corresponding to the addition of a C10:0 fatty acid relative to **M3**.

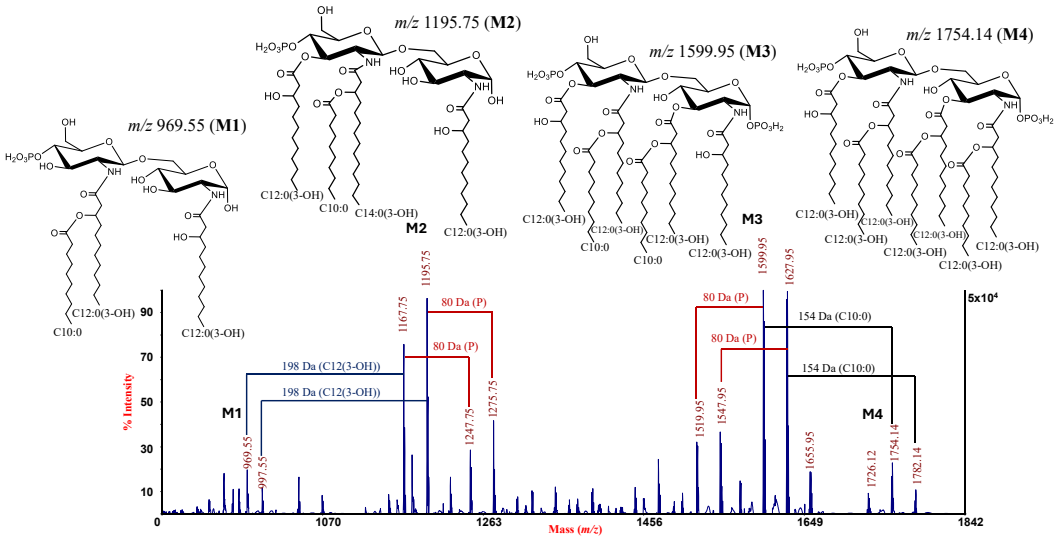


**Fig. 4.19** MALDI-TOF mass spectrum in reflectron negative-ion mode of Lipid A from *Psychrobacter* TAE2020.

**Table 4.5.** Summary of lipid A species identified by MALDI-TOF MS in reflectron negative ion mode. Observed signals correspond to $[M-H]^-$ ions.

| Species | Mass $[M-H]^-$ obs | Mass $[M-H]^-$ calc | Composition |
|---|---|---|---|
| **M1** | 969.55 | 969.58 | $GlcN_2P[C12:0(3\text{-}OH)]_2[C10:0]$ |
| **M2** | 1195.75 | 1195.77 | $GlcN_2P[C14:0(3\text{-}OH)][C12:0(3\text{-}OH)]_2[C10:0]$ |
| **M3** | 1599.95 | 1600.01 | $GlcN_2P_2[C12:0(3\text{-}OH)]_4[C10:0]_2$ |
| **M4** | 1754.14 | 1754.15 | $GlcN_2P_2[C12:0(3\text{-}OH)]_4[C10:0]_3$ |

### 4.15 MALDI-TOF analysis of hydrolyzed lipid A

The distribution of secondary fatty acids in lipid A from *Psychrobacter* sp. TAE2020 was investigated by alkaline hydrolysis with concentrated ammonium hydroxide, as reported by Casillo et al. (Casillo et al., 2018). This treatment selectively hydrolyzed acyl and acyloxyacyl esters while leaving acyl and acyloxyacyl amides intact. MALDI-TOF mass spectrometry of the hydrolyzed sample provided insights into the acylation pattern of lipid A (**Fig. 4.20**).

The MALDI-TOF spectrum, acquired in reflectron negative ion mode on lipid $A_{NH_4OH}$ from *Psychrobacter* sp. TAE2020, displayed five main signal clusters corresponding to species **K1-K5** (**Fig. 4.20**). Less abundant signals were also observed at higher (+28 Da) and lower (-28 Da) *m/z* values, which were attributed to the substitution of C12:0(3-OH) with C14:0(3-OH).

The most intense peak corresponded to species **K4** at *m/z* 1049.51 (Calculated Mass $[M-H]^-$ 1049.54 Da), consistent with the composition $GlcN_2P_2$[C12:0(3-OH)]$_2$[C10:0]. Upon addition of another C10:0 residue, species **K5** appeared at *m/z* 1203.71 (Calculated Mass $[M-H]^-$ 1203.68 Da). Species **K3** at *m/z* 969.61 displays one less phosphate group (-80 Da) compared to the species at *m/z* 1049.51.

Species **K2** at *m/z* 923.42 (Calculated Mass $[M-H]^-$ 923.43 Da, $GlcN_2P_2$[C14:0(3-OH)][C12:0(3-OH)])) corresponds to the species at *m/z* 1077.55 (**K4** + 28 Da) lacking one C10:0 residue

Finally, species **K1** was observed, showing a mass difference of 154 Da compared to the ion at *m/z* 997.58 (**K3** +28 Da), and a difference of 80 Da with respect to species **K2** (**Table 4.6**).

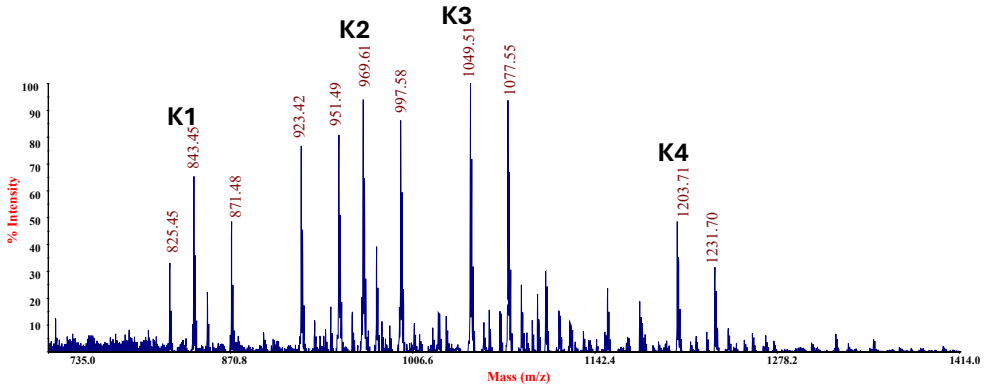


**Fig. 4.20** MALDI-TOF mass spectrum in reflectron negative-ion mode of Lipid A from *Psychrobacter* TAE2020 after $NH_4OH$ treatment.

**Table 4.6.** MALDI-TOF mass spectrometry analysis of lipid $A_{NH4OH}$ from *Psychrobacter* sp. TAE2020. The table shows the observed and calculated *m/z* values of the main ion clusters (**K1-K5**) and their proposed compositions.

| Species | Observed *m/z* | Calculated mass (Da) | Composition |
|---|---|---|---|
| **K1** | 843.45 | 843.46 | $GlcN_2P$[C14:0(3-OH)][C12:0(3-OH)] |
| **K2** | 923.42 | 923.43 | $GlcN_2P_2$[C14:0(3-OH)][C12:0(3-OH)] |
| **K3** | 969.61 | 969.67 | $GlcN_2P$[C12:0(3-OH)]$_2$[C10:0] |
| **K4** | 1049.51 | 1049.54 | $GlcN_2P_2$[C12:0(3-OH)]$_2$[C10:0] |
| **K5** | 1203.71 | 1203.68 | $GlcN_2P_2$[C12:0(3-OH)]$_2$[C10:0]$_2$ |

MS/MS analyses were required to establish whether C10:0 was linked to C12:0(3-OH) attached to the nitrogen of proximal glucosamine (GlcNI) or to C12:0(3-OH) bound to distal glucosamine (GlcNII). The experiments were performed on the most abundant signals of the mass spectrum at *m/z* 1049.52. The MS/MS analysis of the ion at *m/z* 1049.51 produced a spectrum that showed ions which could be readily attributed to the loss of 3-hydroxydecanoic acid (-198 Da) and a phosphate group (-80 Da). Additional ions were also observed, arising from inter-residue or intra-ring fragmentations. In particular, the ion at *m/z* 455.42, corresponding to the $\mathbf{Y_1}^-$ ion according to the nomenclature of Domon and Vath (Domon & Vath, 1990), was detected. This ion was particularly diagnostic, since it indicated that only one C12:0(3-OH) residue was linked to the proximal glucosamine through an amidic bond. The ion at *m/z* 692.71 was identified as the intra-ring fragmentation ion $^{2,5}\mathbf{A_2}$, which

in contrast demonstrated the presence of acyl and acyloxyacyl amides composed of C12:0(3-OH) and C10:0 (**Fig. 4.21**).
In conclusion, ammonium hydroxide hydrolysis combined with MALDI-TOF mass spectrometry allowed the identification of the precise distribution of fatty acids in the lipid A of *Psychrobacter* sp. TAE2020.

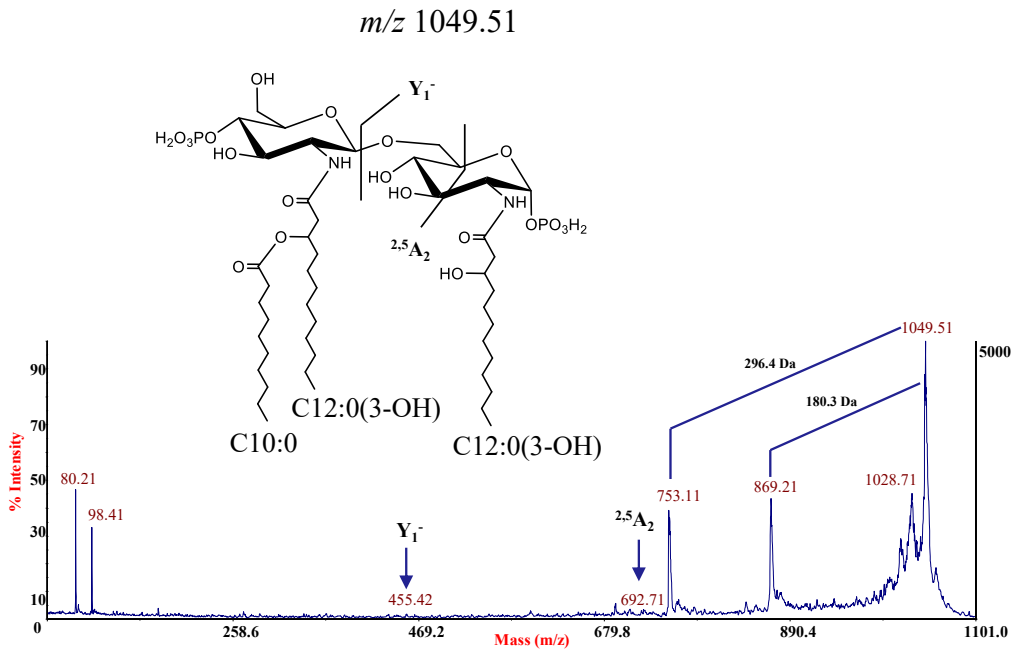


**Fig. 4.21** MALDI-TOF MS/MS spectrum of the precursor ion at *m/z* 1049.5, showing the characteristic fragmentation pattern with $Y_1^-$ and $^{2,5}A_2$ ions highlighted according to the Domon and Vath nomenclature (Domon & Vath, 1990) .

## 4.16 Structural analysis of the saccharide component of the LPS from *Psychrobacter* sp. TAE2020

The rough-type LPS (LOS) from *Psychrobacter* sp. TAE2020 was subjected to sequential deacylation with hydrazine and KOH to remove all fatty acid substituents and isolate the saccharidic portion. Hydrazine treatment cleaved ester-linked acyl chains, while KOH hydrolysis removed the remaining amide-linked and acyloxyacyl groups, leaving the oligosaccharide backbone intact (Holst, 2000).

The completely deacylated LOS was then converted into partially methylated alditol acetates to identify the linkage pattern. The corresponding analytical data are reported in the **Table 4.7**.

**Table 4.7** Methylation analysis of the fully deacylated LOS from *Psychrobacter* sp. TAE2020.

| **PMMA** | **tructural feature** |
|---|---|
| 2,3,4,6-tetra-O-methyl-glucose | Terminal Glc |
| 2,3,6-tri-O-methyl-glucose | 1,4-linked-Glc |
| 2,3,4-tri-O-methyl-glucose | 1,6-linked Glc |
| 2,3-di-O-methyl-glucose | 1,4,6-linked Glc |

The resulting deacylated LOS was subsequently analyzed by mono- and bidimensional NMR experiments for structural characterization.
The $^{1}H$ and $^{1}H,^{13}C$ DEPT-HSQC spectra are presented below. The structural elucidation of the saccharidic portion is currently underway.

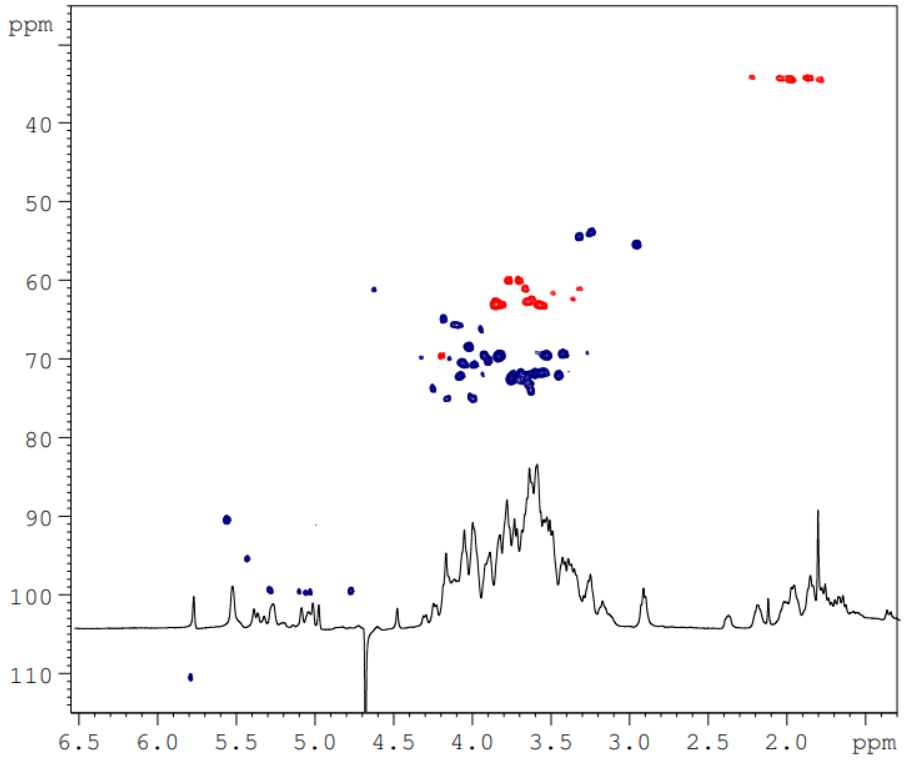


**Fig. 4.22** $^{1}$H NMR spectrum overlaid with $^{1}$H,$^{13}$C DEPT-HSQC (blue and red) of completely deacylated LPS from *Psychrobacter* sp. TAE2020. The spectrum was recorded in $D_2O$ at 298 K on a 600 MHz spectrometer.

## 4.17 Discussion and conclusion

The structural analysis of the LPS from *Psychrobacter* sp. TAE2020 revealed a rough-type LPS, characterized by a heterogeneous population of lipid A species differing in acylation pattern and phosphorylation state. This variability is consistent with what has been reported for other cold-adapted Gram-negative bacteria, in which lipid A structural plasticity contributes to maintaining membrane properties under low-temperature conditions .(Casillo et al., 2017, 2018; Sweet et al., 2015).

This study primarily focused on the structural characterization of the lipid A moiety, using chemical treatments combined with high-resolution mass spectrometry. The resulting profile showed short-chain 3-hydroxy fatty acids (C10-C14) and extensive glycoform heterogeneity, closely resembling the lipid A structures described in other *Psychrobacter* strains and Antarctic isolates. These findings support the existence of shared structural traits among psychrophilic bacteria.

In parallel, complete deacylation of the LOS was performed to enable the targeted study of its saccharidic domain, whose structural elucidation is currently in progress.

Overall, the structural characterization of the LOS, integrated with the previously available information on the CPS of *Psychrobacter* sp. TAE2020, will allow for a more comprehensive definition of the glycan repertoire of this microorganism, expanding our understanding of its surface architecture and laying the foundation for future studies aimed at exploring the ecological and functional implications of these structures in polar environments.

# *Materials and Methods*

# Chapter V:
## *Materials, Methods and Experimental Procedures*

### 5.1 Ethics approval and informed consent

Clinical isolates of *Pseudomonas aeruginosa* were obtained under the approval of the Ethical Committee of the Pediatric Hospital and Institute of Research Bambino Gesù (OPBG), Rome, Italy (No. 1437_OPBG_2017, July 2017). The study complied with the principles of the Declaration of Helsinki, and written informed consent was obtained from all participants and their legal guardians.

### 5.2 Bacterial strains and growth conditions

The bacterial strains analyzed in the present PhD thesis were obtained through the kind contribution of external collaborators.

The cultivation of the *Pseudomonas aeruginosa* strains was performed by Prof. Rosanna Papa (Sapienza University of Rome), whereas the cultivation of the *Psychrobacter* sp. TAE2020 strain was carried out by Prof. Ermenelgida Parrilli (University of Naples Federico II).

Six clinical strains of *P. aeruginosa* (WT2, WT4, MDR1, MDR5, PDR5, PDR7), isolated from respiratory specimens of cystic fibrosis (CF) patients during follow-up at Pediatric Hospital Bambino Gesù (OPBG) in Rome, were used (Papa et al., 2023). Additionally, *P. aeruginosa* PA14 was utilized as a reference strain for studies on pathogenesis and biofilm formation. According to The European Committee on Antimicrobial Susceptibility Testing (http://www.eucast.org), antibiotic-sensitive wild-type (WT) strains are defined as sensitive to all antimicrobials, while pan-drug-resistant (PDR) strains are resistant to all antibiotics in all classes (**Table. 5.1**).

This study specifically considered two PDR and two MDR non-mucoid strains isolated from the airways of CF patients with chronic colonization (4-15 years), two WT strains isolated from the airways of CF patients with recent infection (<12 months), and the reference strain PA14.

Bacteria were grown in Brain Heart Infusion broth (BHI, Oxoid, Basingstoke, UK). Planktonic condition was performed in flasks at 37 °C under orbital shaking (180 rpm), while biofilm formation was performed in 6-well at 37 °C in static conditions. Bacteria grew 24 h. For planktonic growth, cells were separated from the supernatants by centrifugation (4000 rpm, 15 min at 4 °C). The resulting pellet was frozen at -80 °C and subsequently dried.

Cells deriving from sessile growth were scraped from the bottom of the 6-well plate and the resulting mixture was centrifuged at 4000 rpm for 15 min at 4 °C. The derived bacterial pellet was frozen at -80 °C and dried.

**Table 5.1.** Antibiotic susceptibility profiles of selected *Pseudomonas aeruginosa* strains. Abbreviations: S, susceptible (standard dosing regimen); I, susceptible (increased exposure); R, resistant; X, not tested. Susceptibility testing was performed according to EUCAST Clinical Breakpoint Tables v. 13.0 (valid from 1 January 2023) (Papa et al., 2023).

| | Group MDR | | Group PDR | | Group WT | |
|---|---|---|---|---|---|---|
| **Antibiotics** | **MDR1** | **MDR5** | **PDR5** | **PDR7** | **WT2** | **WT4** |
| Ciprofloxacin | R | R | R | R | I | I |
| Levofloxacin | R | R | R | R | I | I |
| Piperacillin–tazobactam | R | R | R | R | I | X |
| Aztreonam | R | R | R | R | I | I |
| Ceftazidime | R | R | R | R | I | I |
| Cefepime | R | R | R | R | I | I |
| Amikacin | R | R | R | R | S | S |
| Tobramycin | R | R | R | R | S | S |
| Imipenem | R | R | R | R | I | I |
| Meropenem | R | R | R | R | S | S |
| Colistin | S | S | R | R | S | X |
| Ceftazidime–avibactam | R | S | R | R | X | S |
| Ceftolozane–tazobactam | R | S | R | R | X | S |

*Psychrobacter* sp. TAE2020 was collected in 1992 from seawater near the French Antarctic Station Dumont d'Urville, Terre Adélie (66°40' S; 140°10' E). *Staphylococcus epidermidis* O-47, isolated from a case of septic arthritis, was kindly provided by Prof. Götz (Heilmann et al., 1996), while *S.*

*epidermidis* RP62A, a reference strain, was isolated from an infected catheter (ATCC 35984).
*Psychrobacter* sp. TAE2020 was grown in synthetic medium Gut (L-Glutamic acid 10 g/L, NaCl 10 g/L, $NH_4NO_3$ 1 g/L, $KH_2PO_4 \cdot 7H_2O$ 1 g/L, $MgSO_4 \cdot 7H_2O$ 200 mg/L, $FeSO_4 \cdot 7H_2O$ 5 mg/L, $CaCl_2 \cdot 2H_2O$ 5 mg/L) in planktonic conditions at 15°C under vigorous agitation (250 rpm) for 72 h.
Staphylococci were grown at 37°C in Brain Heart Infusion broth (BHI, Oxoid, UK). Biofilm formation was assessed in static conditions, while planktonic cultures were performed under agitation (180 rpm). All strains were maintained at -80°C in cryovials with 20% glycerol.
A summary of the genomic and environmental metadata of *Psychrobacter* sp. TAE2020 is reported in **Table 5.2**.

**Table 5.2.** MIxS (Minimum Information about any (x) Sequence) checklist summarizing the genomic, environmental and isolation metadata of *Psychrobacter* sp. TAE2020, a marine strain collected near the French Antarctic Station Dumont d'Urville (Terre Adélie) (Riccardi et al., 2022).

| Item | Description |
|---|---|
| **Organism / Strain** | *Psychrobacter* sp. TAE2020 |
| **Investigation type** | Bacteria_archaea |
| **Project name** | Transcriptional Regulatory Networks in Antarctic bacteria as a proxy for global warming effects on microbial life in the Polar Oceans |
| **Geographic location (latitude/longitude)** | 66°40′ S; 140°01′ E |
| **Geographic location (sea, region)** | French Antarctic station Dumont d'Urville, Terre Adélie |
| **Collection date** | 1994-09 |
| **Broad-scale environmental context** | Marine biome [ENVO:00000447] |
| **Environmental medium** | Terre Adélie [GAZ:00008877] |
| **Local environment context** | Coastal sea water [ENVO:00002150] |
| **Observed biotic relationship** | Free living |
| **Encoded traits** | Biosurfactants producer |
| **Relationship to oxygen** | Aerobe |
| **Sequencing method** | Illumina HiSeq 2500 |
| **Assembly software** | SPAdes; 3.12.0 |
| **Annotation** | Prokka; 1.12 |
| **Number of contigs** | 33 |
| **Feature prediction** | Prodigal; 2.6.3 |
| **16S recovered software** | Barrnap; 0.9 |
| **Number of standard tRNAs extracted** | 42 |
| **tRNA extraction software** | Prokka; 1.12 |

## 5.3 Preliminary investigation of glycans from bacterial cells

A preliminary check was performed by preparing and running a 14% DOC-PAGE gel of LPS after its selective extraction from a small aliquot of bacterial cells. Cells were lysed through enzymatic digestion with proteinase K (5 mg/mL) at 56 °C for 10 minutes in sample buffer 0.5 M Tris-HCl (pH 6.8), glycerol (20% v/v), mercaptoethanol (4% v/v), SDS (4% w/v), and

bromophenol blue (0.2% w/v). LPS was then visualized by 14% DOC-PAGE followed by silver nitrate staining (Abbass et al., 2010).

## 5.4 Glycan extraction

### 5.4.1 LPS isolation

Bacterial dried cells were extracted using the PCP (phenol/chloroform/petroleum ether, 2:5:8 v/v/v) method (Galanos et al., 1969). After removing chloroform and petroleum ether, the phenolic phases were dialyzed against water (cut-off 1000 Da) and freeze-dried ($LPS_{PCP}$). The cell debris was then extracted using the hot phenol-water method (Westphal, 1965). The obtained aqueous phase was purified from proteins and nucleic acids by treatment with DNase and RNase from bovine pancreas at 37°C for 16 h, followed by Proteinase K from *Streptomyces griseus* at 60 °C for 2 h (Nguyen et al., 2019). The mixture was dialyzed against water (cut-off 1000 Da) and freeze-dried ($LPS_{H2O}$).

The LPS samples were suspended in chloroform/methanol (1:2, v/v) to a concentration of 10 mg/mL and centrifuged to remove phospholipids (Bligh & Dyer, 1959).

Alternatively, LPS was isolated from lyophilized bacterial cells using the hot phenol-water extraction method described by Westphal et al. (Westphal, 1965). The aqueous phase was extensively dialyzed against deionized water for three days (ZelluTrans membrane, 30 kDa MWCO; Carl Roth GmbH + Co., Karlsruhe, Germany) and subsequently lyophilized. The resulting crude LPS was resuspended in ultrapure water, sonicated to ensure homogenization, and subjected to three consecutive ultracentrifugation steps (6h each, 105,000× g) using a Beckman Coulter centrifuge (Beckman Coulter Life Sciences Division, Indianapolis, IN, USA). The supernatant obtained after the first ultracentrifugation was lyophilized, while the pellet containing LPS was further purified as required (Lukasiewicz et al., 2006).

### 5.4.2 Extracellular polysaccharides (EPSs) extraction

Following cell cultivation, the culture supernatant was freeze-dried to concentrate the extracellular fraction. The lyophilized material was hydrolyzed with 1% (v/v) aqueous acetic acid at 100 °C for 3 h. The resulting suspension was centrifuged at 4 °C for 60 min to remove insoluble residues. The clarified supernatant was purified by size-exclusion chromatography on a Sephacryl S-

300HR column (Sigma; 110 × 0.75 cm) at a flow rate of 10.0 mL $h^{-1}$ with a fraction volume of 2.5 mL, using 0.05 M ammonium bicarbonate as the eluent. Elution was monitored with a refractive index detector (Knauer K-2301), and fractions containing homogeneous polysaccharides were pooled and lyophilized to obtain the final preparation (Drouillard et al., 2018; Kuschmierz et al., 2022).

### 5.4.3 Capsular polysaccharide (CPS) extraction

Capsular polysaccharides (CPS) were extracted from bacterial cells using a mild thermal-saline treatment, adapted from established protocols for the recovery of surface-associated polysaccharides. Lyophilized bacterial cells were suspended in a 1M NaCl solution at a ratio of approximately 10 mL of solution per gram of biomass. The suspension was incubated at 60 °C for 60 min under gentle agitation to promote capsule detachment from the cell surface without inducing cell lysis.

Following incubation, the suspension was centrifuged at 8,000 × *g* for 30 min at 4 °C to separate the cells from the soluble fraction. The extraction and centrifugation steps were repeated three times to maximize CPS recovery. The resulting supernatants, containing the released CPS, were pooled and lyophilized.

The residual bacterial pellet, previously extracted with NaCl, was also lyophilized and subjected to additional extractions using PCP and phenol/water (P/W) methods to recover any remaining capsular polysaccharide fractions associated with the cell surface.

## 5.5 CPS purification

The lyophilized aqueous phase obtained from the phenol/water (P/W) extraction was hydrolysed with 1% aqueous $CH_3COOH$ (15 mL, 100° C, 3 h). The resulting suspension was then centrifuged (4° C, 60min), and the supernatant portion was fractionated on a Sephacryl S-500HR (Sigma, 110 × 0.75 cm, flow rate 10.0 mL/h, fraction volume 2.5 mL), eluted with 0.05 M ammonium bicarbonate. The elution was monitored with a refractive index detector (Knauer K-2301). The fractions containing the same homogeneous polysaccharide were pooled and freeze-dried (Carillo et al., 2015).

### 5.6 CPS hydrolysis

CPS (30 mg) was solvolyzed in trifluoromethanesulfonic acid ($CF_3SO_3H$, 500 µL) at 25°C for 24 h. The reaction was neutralized with $NH_3$ on ice and the product freeze-dried (Knirel et al., 2019; Kocharova et al., 2001; Perepelov et al., 2000). The dried material was fractionated via BioGel-P2 chromatography (Biorad, 70 × 0.5 cm, $H_2O$ eluent, flow rate 7 mL/h), monitored with a refractive index detector (Knauer K-2301). Isolation of monosaccharides was achieved by reversed-phase column chromatography Synergi™ 4 µm Polar-RP 80 Å (4.6 mm I.D. x 250 mm, Phenomenex, Macclesfield, UK) on an Agilent HPLC instrument 1100 series, using $CH_3OH/H_20$ (4:6 *v/v*) as eluant.

CPS (30 mg) was incubated at 100 °C (1h) in 1 mL of 0.1 M hydrochloric acid (HCl), neutralised with NaOH (0.1M) and lyophilised. The sample was then purified by size-exclusion chromatography using a Sephacryl S-400 column (100 x 0.75 cm, flow rate 15.0 mL/h) eluted with 0.05 M ammonium bicarbonate. Chromatographic profile was monitored using an online refractive index detector (Knauer K-2301), and the occurrence of reaction was checked by $^1$H-NMR (D'Amico et al., 2025).

### 5.7 Deoxycholate-Polyacrylamide Gel Electrophoresis (DOC-PAGE)

Polyacrylamide gel electrophoresis (PAGE) was performed using the system of Laemmli and Favre (Laemmli & Favre, 1973) with sodium deoxycholate (DOC) as detergent, as already reported (Ricciardelli et al., 2019). CPS and LPS bands were visualised after Alcian blue and silver nitrate staining (Tsai & Frasch, 1982b).

### 5.8 Chemical analysis

#### 5.8.1 Acetylated O-methyl glycosides (AMG)

Monosaccharides were derivatized as acetylated methyl glycosides (AMGs) and analyzed by gas chromatography-mass spectrometry (GC-MS). Samples (1 mg) were methanolyzed in HCl/MeOH (1.25 M, 1 mL) at 80°C for 16 h (Abid et al., 2019), followed by hexane extraction. The hexane layer was directly analyzed for fatty acid methyl esters, while the methanol phase was dried and acetylated ($Ac_2O$/pyridine, 100°C, 30 min). GC-MS was conducted on an Agilent 7820A instrument with a 5977B MS detector and HP-5 capillary column (30 m × 0.25 mm i.d.; He, 1 mL/min) (Artini et al., 2019).

### 5.8.2 Acetylated Alditols (AA)

A portion of the freeze-dried material (1 mg) was subjected to hydrolysis with 2 M TFA at 120 °C for 2 h. The hydrolysate was evaporated under a gentle air stream, and the released monosaccharides were reduced in ethanol using $NaBH_4$ to generate alditols. These were subsequently acetylated with acetic anhydride (25 µL) in pyridine (25 µL) at 80 °C for 30 min. After removal of solvents under airflow, the acetylated alditols were resuspended in 100 µL of acetone and analyzed by GC-MS (Corsaro et al., 1997).

### 5.8.3 Partially Methylated Alditol Acetates (PMAA)

Linkage positions were determined after derivatization of the sample into partially methylated acetylated alditols. The sample was methylated with 100 µL of $CH_3I$ and subsequently hydrolyzed with 2 M TFA at 120 °C for 2 h. Following neutralization, the hydrolysate was reduced with $NaBD_4$, acetylated, and injected into the GC-MS system. Analyses were performed on an Agilent 7820A gas chromatograph coupled to a 5977B mass selective detector, equipped with an HP-5 capillary column (30 m × 0.25 mm i.d., Agilent). Helium was used as the carrier gas (flow rate: 1 mL/min). The temperature program for the analysis of methyl glycosides and partially methylated alditol acetates was as follows: 140 °C for 3 min; ramp 140 → 240 °C at 3 °C/min; hold at 240 °C; ramp 90 → 140 °C at 25 °C/min; ramp 140 → 200 °C at 5 °C/min; ramp 200 → 280 °C at 10 °C/min; final hold at 280 °C for 10 min (Ricciardelli et al., 2020).

### 5.8.4 Octyl-glycosides (OGA)

The absolute configuration of the sugars was determined by gas-chromatography analysis of their acetylated (-)-2-octyl glycosides (Leontein et al., 1978). Acetylated octyl glycosides were analysed on an Agilent Technologies gas chromatograph 7820A equipped with a mass selective detector 5977B and an HP-5 capillary column (Agilent, Milan, Italy; 30 m × 0.25 mm i.d., flow rate 1 mL/min, He as carrier gas) at 150 °C for 5 min, then 150°C-> 240° C at 6° C $min^{-1}$, and 240° C for 5 min. The diastereoisomeric octyl-glycosides obtained were deduced by comparison with authentic standards.

### 5.8.5 Dephosphorylation of LPS by hydrofluoric acid (HF) treatment prior to GC-MS analysis

LPS (1 mg) was treated with 100 µL of 48% aqueous hydrofluoric acid (HF) (Sigma Aldrich®, St. Louis, MO, USA) at 4 °C for 16 h to remove phosphate groups. The reaction mixture was kept in an ice bath throughout the treatment. After incubation, the HF was carefully evaporated to dryness under a fume hood at low temperature. The HF-treated residue was then dissolved in distilled water and lyophilized.

The resulting dephosphorylated sample was subsequently analyzed as acetylated methyl glycosides (AMG), following the procedure described in Section 2.8.1. This treatment enables the detection of phosphorylated Kdo and heptose residues by GC–MS, since HF cleavage efficiently removes phosphate groups without degrading the sugar backbone.

### 5.8.6 Gas Chromatography Mass Spectrometry (GC-MS)

All analyses were performed using an Agilent Technologies 7820A Gas Chromatograph equipped with a 5977B mass selective detector and an HP-5 capillary column (Agilent, Milan, Italy; 30 m × 0.25 mm). Helium was used as the carrier gas at a flow rate of 1 mL/min.

For AMG and OGA analysis, the temperature program was set as follows: initial temperature of 140 °C held for 3 min, followed by a ramp from 140 °C to 240 °C at 3 °C/min.

For PMAA analysis, the program was: 90 °C for 1 min, ramped from 90 °C to 140 °C at 25 °C/min, then from 140 °C to 200 °C at 5 °C/min, followed by an increase from 200 °C to 280 °C at 10 °C/min, with a final hold at 280 °C for 10 min.

For fatty acid analysis, the temperature program was: 150 °C for 5 min, ramped from 150 °C to 280 °C at 3 °C/min, with a final hold at 280 °C for 5 min.

## 5.9 Deacylation of the lipooligosaccharide (LOS)

During the structural analysis of the LPS core region, mild acid hydrolysis is commonly considered; however, this treatment leads to dehydration of Kdo, with the consequent formation of artifacts. These artifacts can significantly increase sample heterogeneity and complicate the interpretation of NMR spectra, as they may be present in non-negligible amounts. To overcome this problem, the lipooligosaccharide (LOS) is fully deacylated through a two-step procedure involving de-O-acylation followed by de-N-acylation (**Fig. 5.9**),

which allows the isolation of the entire glycosidic portion of the molecule (Holst, 2000).

In the first step, LOS (20 mg) is dried over phosphorus pentoxide under vacuum and subsequently treated with anhydrous hydrazine (5 mL) at 37 °C for 2 h. This mild alkaline treatment selectively removes the ester-linked fatty acids. Cold acetone is then added, and the resulting pellet is recovered by centrifugation at 7000 rpm and 4 °C for 30 min. After three washes with acetone, the pellet is suspended in water and lyophilized (Casillo, Parrilli, et al., 2017; Holst, 2000).

Complete deacylation is then achieved through a strong alkaline treatment with 4 M KOH at 120 °C for 16 h, which removes additional substituents such as acetyl and pyrophosphate groups while leaving the phosphate groups intact. The reaction mixture is neutralized with HCl, and the aqueous phase is extracted three times with $CHCl_3$. The combined aqueous layers are recovered and desalted using a Sephadex G-10 column (2.5 × 43 cm; flow rate 31 mL $h^{-1}$; fraction volume 2.5 mL; eluent: 10 mM $NH_4HCO_3$). The eluted oligosaccharide is finally lyophilized and analyzed by 1D and 2D NMR spectroscopy.

This strategy, by increasing the hydrophilic nature of the molecule and avoiding Kdo degradation, allows the structural characterization of the core region of R-LPS by NMR.

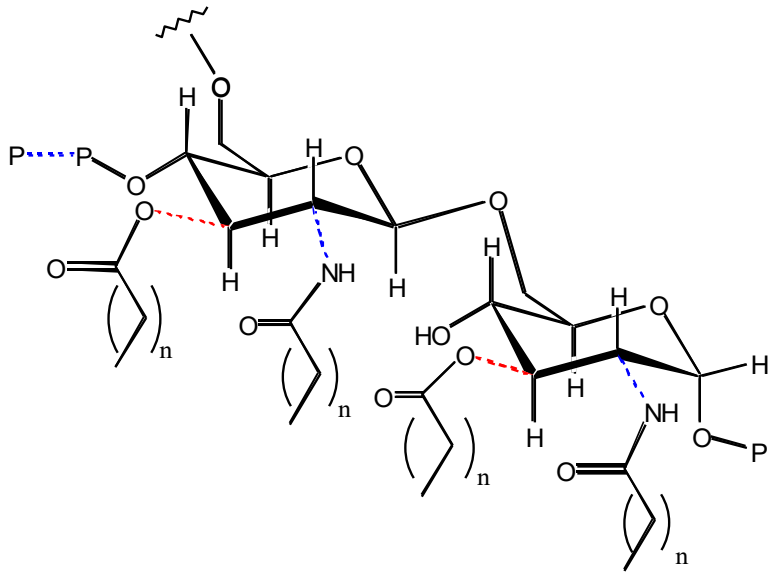


**Fig. 5.1** Schematic representation of lipid A. The red and blue dotted lines indicate the specific linkages cleaved upon treatment with hydrazine and KOH, respectively.

## 5.10 Isolation and purification of lipid A

LPS samples were subjected to mild acid hydrolysis by treatment with 1% aqueous acetic acid (100 °C, 3 h, 10 mg/mL), following the procedure described by Fresno et al. (2007) (Fresno et al., 2007). This method exploits the intrinsic acid lability of the ketosidic linkage between the 3-deoxy-D-manno-oct-2-ulosonic acid (Kdo) residue and the C6 position of the reducing glucosamine unit (GlcN I) of the lipid A backbone. This bond, formed between the anomeric C2 of Kdo and the C6 hydroxyl of GlcN I (2→6 linkage), is particularly sensitive to acid because of the combined effect of its ketosidic nature and the presence of a neighboring carboxyl group at C1, which destabilizes the anomeric center upon protonation. These structural features make the Kdo→GlcN I linkage inherently more prone to acid hydrolysis compared to typical aldohexosidic bonds.

As a result, mild acid treatment leads to the cleavage of the Kdo→GlcN I linkage and the release of the core oligosaccharide along with Kdo residues, while preserving the integrity of the lipid A disaccharide backbone and its acylation pattern (**Fig. 5.2**).

After hydrolysis, the resulting suspension was centrifuged (7000 rpm, 4 °C, 30 min) to separate the insoluble lipid A fraction (pellet) from the soluble

saccharide fraction (supernatant). The lipid A precipitate was washed twice with distilled water to remove residual acid and sugars, and subsequently freeze-dried.
Further purification of lipid A was performed by Celite chromatography using a chloroform/methanol (4:1, v/v) elution system to remove residual organic or saccharide contaminants. The absence of protein contamination was confirmed by the Lowry assay (Casillo et al., 2017).

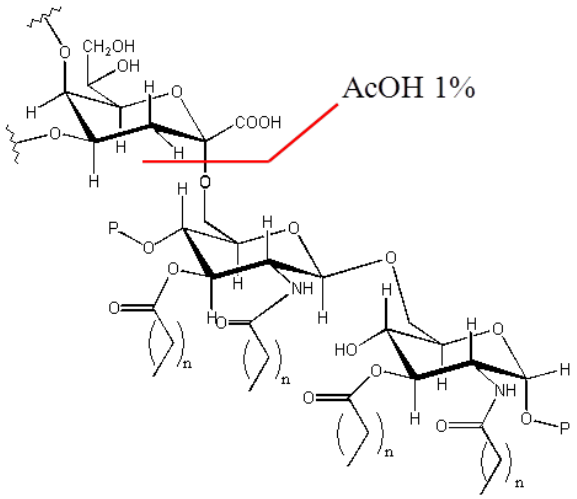


**Fig. 5.2** Schematic representation of the selective Kdo linkage cleavage occurring under mild acid conditions (1% AcOH).

### 5.10.1 $NH_4OH$ hydrolysis of lipid A

Lipid A (0.5 mg) was subjected to mild alkaline hydrolysis to selectively remove ester-linked fatty acids while preserving amide-linked acyl and acyloxyacyl chains. The sample was suspended in 200 µL of concentrated ammonium hydroxide ($NH_4OH$, 28-30%) and incubated in a tightly sealed reaction vial at 37 °C for 5 h under gentle agitation. Under these conditions, the ester bonds between the glucosamine backbone and the primary fatty acids are cleaved, whereas the amide-linked acyl chains at positions 2 and 2′ and the acyloxyacyl substituents remain intact.
After incubation, the reaction mixture was dried under a gentle stream of air to remove residual ammonia and water. The partially deacylated lipid A was then analyzed by MALDI-TOF mass spectrometry. This treatment simplifies the

mass spectrum, allowing the characterization of the lipid A acylation pattern through the selective removal of ester-linked fatty acids (Casillo et al., 2018).

### 5.10.2 $NH_2NH_2$ hydrolysis of lipid A

Lipid A was subjected to hydrazinolysis in order to selectively remove ester-linked fatty acids. Samples (20 mg) were dried over phosphorus pentoxide under vacuum and subsequently treated with hydrazine (5 mL) at 37 °C for 2 h. Under these conditions, hydrazine cleaves the ester bonds linking both primary and secondary fatty acids to the glucosamine backbone, while leaving the amide-linked acyl chains intact. Cold acetone was then added to the reaction mixture, and the resulting precipitate was recovered by centrifugation at 7000 rpm and 4 °C for 30 min. The pellet was washed three times with cold acetone to remove residual hydrazine and released fatty acids, then suspended in water and lyophilized to obtain the partially deacylated Lipid A (Holst, 2000).

The resulting Lipid A was subsequently analyzed by mass spectrometry to determine its acylation pattern and confirm the selective removal of ester-linked fatty acids.

## 5.11 Mass Spectrometry

### 5.11.1 Matrix-Assisted Laser Desorption/Ionization Time-of-Flight Mass Spectrometry (MALDI-TOF MS)

Mass spectrometry (MS) and tandem mass spectrometry (MS/MS or $MS^2$) are extensively used in the structural determination of lipopolysaccharides (LPS). Soft ionization techniques, such as Matrix-Assisted Laser Desorption/Ionization (MALDI), provide information about the molecular mass of intact molecules and allow the detection of different glycoforms that differ in the presence of glycidic or non-glycidic residues.

MALDI is based on the soft ionization of the sample, which is suspended in a specific matrix that assists analyte ionization upon laser irradiation. The matrix is typically composed of small organic molecules with strong absorption at the laser wavelength, protecting the sample from direct laser energy and ensuring soft ionization with the formation of singly charged ions. For carbohydrate analysis, MALDI spectra are usually acquired in negative ion mode due to the abundance of ionizable groups (e.g., hydroxyl and phosphate moieties). A

high-energy laser source can induce the cleavage of the labile linkage between Kdo and the glucosamine backbone of lipid A.

In the case of LOS, the resulting mass spectra generally display three main signal regions corresponding to lipid A, the core oligosaccharide, and the intact LOS. For LPS molecules bearing O-polysaccharides, information on the size of the repeating unit can also be deduced from the mass distribution. When higher laser intensity is applied, fragment ions can be generated directly in the flight tube, and if the mass spectrometer is equipped with a collision cell, tandem MS (MS/MS) experiments can be performed to select and fragment specific precursor ions. This approach allows the determination of monosaccharide sequences and the identification of branching points through the analysis of product ions arising from glycosidic bond cleavages.

The interpretation of carbohydrate fragmentation spectra is often complex, as fragmentation does not always occur at every glycosidic linkage and different fragment types can be produced. The nomenclature commonly used for oligosaccharide fragmentation was introduced by Domon and Costello (Domon & Costello, 1988). According to this system, fragment ions containing the non-reducing end are labeled A, B, and C, while those containing the reducing end or the aglycone are labeled X, Y, and Z (**Fig. 5.3**). Subscript numbers indicate the number of monosaccharide units present in the fragment. B, C, Y, and Z ions originate from glycosidic bond cleavages, with B and Y ions resulting from cleavages on the non-reducing side of the glycosidic oxygen, and C and Z ions on the reducing side. A and X ions derive from glycosidic ring cleavages and are labeled with superscripts corresponding to the broken ring bonds

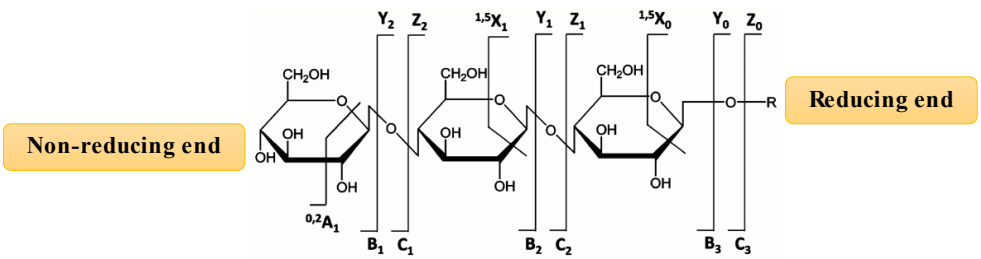


**Fig. 5.3** Schematic representation of the Domon and Costello nomenclature for glycoconjugate fragment ions generated by tandem MS/MS.

For the experimental analyses, MALDI-TOF mass spectra were acquired on two different instruments. The first set of measurements was performed on an AB SCIEX TOF/TOF™ 5800 mass spectrometer (AB SCIEX, Darmstadt, Germany) equipped with an Nd laser (λ = 345 nm, <500-ps pulse length, repetition rate up to 1000 Hz). Approximately 2000 laser shots were accumulated per spectrum. Mass calibration was carried out using a hyaluronan oligosaccharide mixture. As matrices, 2,5-dihydroxybenzoic acid (DHB) dissolved in 70% $CH_3CN$/30% TFA and 2,4,6-trihydroxyacetophenone (THAP) in MeOH/$H_2O$ (1:1) were used.
A second set of experiments was conducted on an UltrafleXtreme spectrometer (Bruker Daltonik GmbH, Bremen, Germany). External calibration was achieved using peptide or protein standards supplied by the manufacturer. Lipid A and oligosaccharides were mixed with THAP or DHB matrix solution (10 mg/mL), dried at room temperature, and analyzed. The obtained spectra were deconvoluted and processed using Data Analysis 4.0 or FlexAnalysis software (Bruker Daltonik GmbH). Fragmentation data were further interpreted using GlycoWorkbench and ChemSketch software.

### 5.11.2 Electrospray Ionization Mass Spectrometry (ESI-$MS^n$)

Negative-ion electrospray ionization mass spectrometry (ESI-$MS^n$) was carried out using an Esquire-LC ion trap mass spectrometer (Bruker Daltonics, Bremen, Germany). Prior to analysis, lipid A samples were desalted by extraction with chloroform/water (1:1, v/v) and subsequently dissolved in methanol/chloroform (1:1, v/v) at a concentration of 1.0 mg/mL. Samples were introduced by continuous infusion into the ion source at a flow rate of 2 µL/min using a linear syringe pump, with a capillary voltage of 4.0 kV. Spectra were acquired over the *m/z* 200-2000 range. For precursor ion selection, the mass isolation window was set to 4.0 Da in all $MS^n$ experiments (Gozdziewicz et al., 2021).

## 5.12 Transmission Electron Microscopy (TEM)

The samples were prepared for TEM observations as detailed in Escalera 2014 (Escalera et al., 2014). Briefly, specimens were fixed with 2.5% glutaraldehyde, post-fixed with 1% osmium tetroxide, dehydrated in a graded ethanol series further substituted by propylene oxide and embedded in Epon 812 (TAAB, TAAB Laboratories Equipment Ltd, Berkshire, UK). Ultrathin sections (60 nm thick) were collected on nickel grids and stained with uranyl

acetate and lead citrate and Transmission Electron Microscopy (TEM) images were acquired with a FEI TECNAI $G^2$ 200kV instrument.

## 5.13 Nuclear Magnetic Resonance spectroscopy (NMR)

### 5.13.1 NMR spectroscopy in solution

One- and two-dimensional $^{1}H$ and $^{13}C$ NMR spectra were recorded in deuterium oxide ($D_2O$) at pD 7.0. Experiments were performed at 298 K using a Bruker DRX-600 MHz spectrometer equipped with a cryoprobe, and at 307 K using a Bruker Avance 600 MHz instrument. $^{13}C$ NMR experiments were also carried out on a Bruker DRX-400 MHz spectrometer. Chemical shifts were calibrated using acetone as an internal reference ($\delta_H$ = 2.225 ppm; $\delta_C$ = 31.45 ppm).

A complete set of 2D NMR experiments was acquired to assign spin systems and establish connectivities. Homonuclear spectra included double-quantum-filtered correlation spectroscopy (DQF-COSY), total correlation spectroscopy (TOCSY), and Nuclear Overhauser enhancement spectroscopy (NOESY) or rotating frame Overhauser enhancement spectroscopy (ROESY). TOCSY experiments were acquired with mixing (spin-lock) times of 100 ms, while NOESY/ROESY experiments used mixing times ranging from 100 to 300 ms (typically 150 ms), acquiring 16 scans per increment.

Data sets ($t_1 \times t_2$) consisted of 4096 × 256 points for TOCSY and NOESY/ROESY, and 4096 × 512 points for DQF-COSY. The $t_1$ and $t_2$ time domains were converted by double Fourier transformation into the F1 (indirect) and F2 (direct) frequency axes, producing 2D spectra in which cross-peaks indicate correlations between nuclei. Homonuclear experiments (COSY, TOCSY) reveal scalar couplings, whereas NOESY and ROESY highlight through-space proximities. In NOESY/ROESY, the intensity of cross-peaks is inversely proportional to the sixth power of the internuclear distance:

$$I_{NOE} \propto \frac{1}{r^6}$$

This relationship provides qualitative distance information, which is particularly useful for mapping spatial proximities within the oligosaccharide structure.

The data matrix for all homonuclear experiments was zero-filled to 4K × 2K points and resolution-enhanced in both dimensions using a cosine-bell window function prior to Fourier transformation. Coupling constants were determined from phase-sensitive DQF-COSY spectra.
Heteronuclear experiments included $^{1}H$,$^{13}C$ HSQC and HMBC. HSQC spectra were recorded in phase-sensitive mode using echo/antiecho gradient selection and multiplicity editing during the selection step. HMBC experiments were optimized for long-range coupling constants and employed a low-pass J-filter to suppress one-bond correlations, using gradient pulses for selection. A 60 ms relay was used for the evolution of long-range correlations. Data sets for HSQC and HMBC consisted of 2048 × 256 points, with proton detection and broadband decoupling in the $^{13}C$ domain. DEPT-HSQC and F2-coupled HSQC were also acquired for improved assignment of proton–carbon connectivities.
All spectra were processed using standard Bruker software with zero-filling and apodization to enhance resolution. Experimental conditions and acquisition parameters were chosen according to established procedures.

### 5.13.2 High-Resolution Magic Angle Spinning NMR (HR-MAS NMR)

NMR analyses were performed using high-resolution magic angle spinning (HR-MAS) NMR spectroscopy on a Bruker Avance 600 MHz spectrometer equipped with a $^{1}H/^{13}C$ HR-MAS probe with z-gradients. This technique enables the acquisition of high-resolution spectra from heterogeneous biological samples, such as whole cells or partially soluble macromolecules, by spinning the sample at high speed (in the kHz range) at an angle of 54.7° relative to the static magnetic field. This condition, known as the magic angle, averages anisotropic interactions (dipolar couplings and chemical shift anisotropy), thereby improving spectral resolution while maintaining the samples under conditions close to their physiological state (**Fig. 5.4**).
Intact bacterial cells (4 mg) were analyzed, exchanged three times with 99.9% $D_2O$, suspended in $D_2O$, and directly loaded into $ZrO_2$ rotors to investigate the presence of O-specific polysaccharides of LPSs in their native environment.
Subsequently, purified LPSs were analyzed. For these experiments, 3-4 mg of LPS was exchanged three times with $D_2O$, suspended in 99.9% $D_2O$ (30 µL), and placed into $ZrO_2$ rotors. HR-MAS experiments were performed at a spinning rate of 4 kHz and at a temperature of 298 K, corresponding to the measured temperature of the bearing air used for sample spinning.
One-dimensional $^{1}H$ spectra were acquired using the Carr-Purcell-Meiboom-Gill (CPMG, 90°-(τ-180°-τ)n) pulse sequence, with a total delay time of 1.2

ms, applied as a $T_2$ filter to suppress broad signals arising from lipid components (Jachymek et al., 1999). In addition to 1D spectra, two-dimensional $^1$H-$^1$H COSY, $^1$H-$^1$H TOCSY, and $^1$H-$^{13}$C HSQC experiments were also recorded (Lukasiewicz et al., 2006).

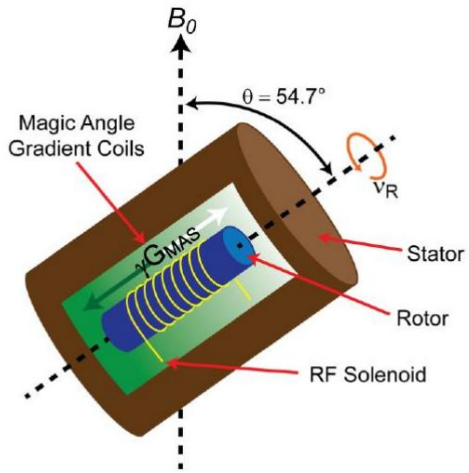


**Fig. 5.4** Figure X. *Schematic representation of the Magic Angle Spinning (MAS) NMR setup.* The rotor is oriented at 54.7° relative to the static magnetic field $B_0$, the so-called magic angle. Key components of the system are indicated, including the stator, rotor, RF coil and magic angle gradient coils. This configuration averages anisotropic interactions, enabling high-resolution spectra of semi-solid and heterogeneous samples. The gradient ($\gamma G_{\mathrm{MAS}}$) is applied along the rotor spinning axis. *Adapted from Alam and Jenkins, 2012.*(Alam & Jenkins, 2012)

## 5.14 CPS molecular weight determination, aggregation and adhesion properties

### 5.14.1 Dynamic and Static Light Scattering (DLS and SLS)

Static and Dynamic Light Scattering (SLS and DLS, respectively) measurements were performed using an LSI spectrometer (LS, Fribourg, Switzerland) composed of a fibre-coupled laser operating at 638 nm. The analyses were conducted at (25.0±0.1) °C using a thermostatic bath.

DLS measurements were carried out at 1.8 mg/mL CPS concentration (before and after HCl treatment) and a fixed scattering angle of 90°. The collected correlation functions were treated with the CORREN algorithm, and the diffusion coefficients were then employed to calculate hydrodynamic radii ($R_h$) through the Stokes-Einstein relation:

$$R_h = \frac{kT}{6\pi\eta\langle D\rangle} \tag{1}$$

where $k$ is the Boltzmann constant, $T$ is the absolute temperature, and $\eta$ is the medium viscosity, whose mean value was assumed to be 0.89 cP for each aqueous mixture, and $<D>$ is the diffusion coefficient.
For SLS, a concentration range between 0.2 and 1.8 mg/mL has been chosen, and the scattering intensity was measured at different scattering angles: 45°, 60°, 75°, 90°, 105°, and 120° (Perfetti et al., 2020b). The mass-average molecular weight $M_w$ and the second virial coefficient $A_2$ of each polysaccharide were determined employing Zimm plot analysis.

$$\frac{Kc}{R_\theta} = \frac{1}{M_W}\left[1 + \frac{q^2\langle R_g^2\rangle}{3} + 2A_2M_Wc\right] \tag{2}$$

where $c$ is the sample mass concentration, $K = \frac{4\pi^2 n_0^2 (dn/dc)^2}{N_A\lambda^4}$ with $n_0$ = 1.33 the refractive index of water, $dn/dc$ = 0.185 the refractive index increment with concentration (Laezza et al., 2017; Paduano et al., 1992), $N_A$ the Avogadro's number, $\lambda$ the laser wavelength in vacuum, $R_\theta$ the excess Rayleigh ratio at 90°. The value of $R_\theta$ was obtained from $R_\theta = (I_s - I_{s,0})/I_{s,R}(n_0^2/n_R^2)R_{\theta,R}$ where $I_s$ is the scattered intensity of the solution, $I_{s,0}$ is the scattered intensity of water, $I_{s,R}$ is the scattering intensity of toluene (the standard), and $n_R$ = 1.496 and $R_{\theta,R}$= 2.85 $10^{-5}$ $cm^{-1}$ are the refractive index and the Rayleigh ratio of toluene, respectively (Kaye & Havlik, 1973). The parameters $q$, and $R_g$ are the modulus

of the scattering vector and the radius of gyration, respectively. Therefore, plotting equation 2 as a function of $c$ and $q$, the so-called Zimm plot was obtained. The values of $Kc/R_\theta$ are extrapolated to zero concentration (equation 3) and angle (equation 4), allowing the obtainment of two datasets that, once fitted, provide the molecular weight, the second virial coefficient, and the gyration radius.

$$\frac{Kc}{R_\theta} = \frac{1}{M_W}\left[1 + \frac{\left\langle R_g^2 \right\rangle}{3} q^2\right] \quad \text{for } c=0 \tag{3}$$

$$\frac{Kc}{R_\theta} = \frac{1}{M_W} + 2A_2 c \quad \text{for } \theta=0 \tag{4}$$

### 5.14.2 Small-Angle X-ray Scattering (SAXS) and ζ-Potential Measurements

To elucidate the capability of CPS to adhere to natural membranes, Small-Angle X-ray Scattering (SAXS) analysis was performed at the beamline B21 of the Diamond Light Source (Didcot, UK).

The experiments were carried out at 25 °C. The beamline configuration had a beam energy of 13.1keV, and a sample-to-detector distance of 3.7 m. This configuration allowed us to collect the data for the scattering vector modulus $q = \frac{4\pi \sin(\theta/2)}{\lambda}$ in the range of values between 0.0026 Å$^{-1}$ and 0.34 Å$^{-1}$, where $\theta$ is the scattering angle. The raw data were corrected for background and empty capillary scattering. The obtained scattering intensity data, *I(q)*, were plotted as a function of $q$ (Gallucci et al., 2024).

From the experimental data, it was possible to calculate the *P(r)* function through the indirect Fourier transform:

$$P(r) = \frac{r^2}{2\pi^2}\int_0^\infty \frac{q^2 I(q) \sin(qr)}{qr} dq \tag{5}$$

*P(r)* represents the atomic distribution in space, which was used to determine the number of lamellae in the vesicles and how the interaction can affect their structure (Vitiello et al., 2024).
The surface charge (ζ-potential) of CPS, vesicle, and CPS/vesicle complex was evaluated by the electrophoretic light scattering using a Zetasaizer Nano ZSP (Malvern Instruments, UK). Each measurement was performed at 25 °C upon a 30 s equilibration time, and the average of three measurements at a stationary level was taken. The ζ-potential was calculated by applying the Smoluchowski model (Pota et al., 2023).
The vesicle used for SAXS and ζ-potential analyses mimicked the lipid composition of lung surfactant, namely DPPC:Chol:POPG:SM:POPS:POPE:PI 64.4:10:13:3.7:3.3:2.6:3 molar ratio (Gallucci et al., 2023). The liposomes, at a concentration of 1 mg/mL, were obtained by the thin-film technique already reported (Vaccaro et al., 2006; Vitiello et al., 2024).
Particularly, SAXS and ζ-potential analyses were performed to increase the amount of CPS (5, 10, 15, 20, 25, 30, and 35 μg) on the lipid membrane. CPS was dissolved in water at a specific concentration to have the desired mass increase.

### 5.15 Statistics and Reproducibility of Results

All statistical analyses were performed using GraphPad Prism 8. Data are presented as mean ± standard deviation (SD). The significance of differences between groups was assessed using a one-way analysis of variance (ANOVA). Additionally, Student's *t*-test (two-tailed) was used to compare two independent samples.

### 5.16 CPS Antiadhesive and Biofilm Inhibition Assays

The antiadhesive and antibiofilm activities of the capsular polysaccharide (CPS) were evaluated as previously described (D'Angelo et al., 2022). Biofilm formation was assessed following the method of Christensen et al., with minor modifications. Sterile 96-well flat-bottom polystyrene plates were inoculated with *S. epidermidis* RP62A (Gowrishankar & Pandian, 2017) or O-47 (Raue et al., 2020) at an initial $OD_{600}$ of ~0.1 and 0.001, respectively, in BHI medium. CPS, CPS-LPS complexes, or CPS pre-treated with HCl were added to the wells at a final concentration of 0.5 mg/mL. The plates were then incubated aerobically at 37 °C for 24 h.

Biofilm biomass was quantified using crystal violet staining. The bound dye was subsequently solubilized with a mixture of 20% glacial acetic acid and 80% ethanol, and absorbance was measured at 590 nm using a Benchmark Plus Microplate Spectrophotometer. Each condition was tested in six technical replicates and repeated in at least two independent experiments.
The effect of CPS on staphylococcal biofilms was further examined by Confocal Laser Scanning Microscopy (CLSM) as previously described ((D'Angelo et al., 2022). The collected CLSM Z-stack images (saved as OME-TIFF) were analyzed with COMSTAT software package a plugin (Comstat 2.1) to ImageJ. The COMSTAT software package was used to determine the different variables describing biofilm including the biovolume ($\mu m^3$ $\mu m^{-2}$), average thicknesses (µm), and roughness coefficient (Ra*).

### 5.17 Emulsifying Activity of CPS

The emulsifying activity (E24) of the capsular polysaccharide (CPS) was evaluated according to the method described by Blesic et al. (2018) (Blesic et al., 2018). Briefly, 2 mL of Dectol (a mixture of decane and toluene, 65:35 v/v) were added to 1 mL of the CPS solution in glass vials. The mixture was vortexed at maximum speed for 5 min using a Mix ARGOlab Vortex Mixer and then left to stand at room temperature for 24 h. The emulsification index after 24 h (E24) was calculated as the ratio between the height of the emulsified layer and the total height of the liquid column, multiplied by 100.

### 5.18 In vitro assays using LPS and Lipid A from *P. aeruginosa*

#### 5.18.1 Murine primary lung-derived fibroblasts *in vitro* culture

Murine primary lung-derived fibroblasts *in vitro* cultures were obtained by following experimental protocols reported by Vassallo et al. 2021 (Vassallo et al., 2021) with slight modifications. In detail, murine lungs were kindly provided upon the sacrifice of animals enrolled in an approved study on food supplements (no. 405/2021-PR, 07/06/2021). These latter were washed twice with Phosphate Buffered Saline (PBS), cut with a sterile scalpel (Fisher Scientific, Italy), and enzymatically digested by using a solution containing collagenase type I at 3 mg/mL (w/v) and dispase at 4 mg/mL (w/v) (Sigma-Aldrich, St-Louis, MO, USA) at 37 °C on a shaking plate for 1 h (Eppendorf, Italy). After that, the cellular suspension was filtered (70 µm), centrifuged at 1300 rpm for 10 min, washed with PBS, and re-centrifuged. The cells were re-

suspended in Dulbecco's Modified Eagle Medium/Nutrient Mixture F-12 (DMEM/F12) supplemented with 200 mM l-glutamine, 10% (v/v) fetal bovine serum (FBS), 1% (v/v) penicillin/streptomycin and 1% (v/v) amphotericin B and seeded on 25 $cm^2$ cell culture flasks (Fisher Scientific, Italy). Primary *in vitro* cell culturing was carried out at 37 °C in a humidified incubator with a 5% $CO_2$ atmosphere and the culture medium was changed every 48 h. All reagents for cell culturing were obtained by GIBCO (Thermo Fisher Scientific, Waltham, USA).

### 5.18.2 Cell viability assay

Murine fibroblasts were incubated in a culture medium (untreated cells, CTR) in the presence of LPS or Lipid A samples at three different concentrations (1, 10 and 100 µg/mL) in triplicate. Specifically, LPS and Lipid A powders were dissolved in 1 mL of PBS with 0.5% (v/v) dimethyl sulfoxide (DMSO) (Sigma-Aldrich, St-Louis, USA) and appropriately diluted in DMEM/F12 supplemented as previously described, to reach the desired concentrations. Cell viability was assayed after 24 and 48 h of incubation by performing tetrazolium dye 3-(4,5-dimethylthiazol-2-yl)-2,5-diphenyltetrazolium bromide (MTT) assay (Sigma-Aldrich, St-Louis, USA). Specifically, the MTT solution (0.5 mg/mL in DMEM without phenol red) was added to the untreated and treated fibroblasts. After 3 h, the insoluble purple formazan products were solubilized by using hydrochloric acid (HCl) 0.1 M in isopropanol (Sigma-Aldrich, St-Louis, USA). The optical densities were measured at 570 nm by Beckman DU 640 spectrometer (Beckman, Italy). The relative cell viability was calculated as reported in Eq.(1) :

$$Viability = \frac{mean\ OD_{570} treated\ cells}{mean\ OD_{570}\ controls} \times 100 \qquad (1)$$

The samples were considered cytotoxic for a reduced viability below 50% con the control, according to ISO 10993-5. Data are presented as mean± SD of three performed tests.

### 5.18.3 QUANTI-THP1-Blue assay

QUANTI-THP1-Blue assay was here performed following the protocol previously reported with slight modifications (Di Guida et al., 2022).

Specifically, the conditioned supernatants coming from the incubation of mice fibroblasts either with LPSs or Lipid As for 24 h were added to THP1-Blue™ ($5 \cdot 10^4$ cells/mL). The resulting supernatants were recovered after an overnight of incubation for NF-κB quantification (QUANTI-Blue reagent, InvivoGen, France). Specific luminescence intensity was measured at 655 nm through a Microplate Reader (Biorad Laboratories, Italy) to determine secreted embryonic alkaline phosphatase (SEAP) levels according to the manufacturer's instructions. Data are presented as mean± SD of three performed tests.

### 5.18.4 TLR-4, Collagen 1A1, IL-6 and gene expression evaluation through quantitative real-time PCR (qRT-PCR)

After 24 h treatment, the intracellular RNA was extracted by TRIzol® Reagent (Invitrogen, Italy). For each sample, 1 µg of RNA was reversely transcribed into cDNA (Reverse Transcription System Kit, Promega, Italy) and a quantitative real-time PCR was performed using the IQ™ SYBR® Green Supermix (BioRad Laboratories, Italy). The PCR reactions were run in triplicate and glyceraldehyde-3-phosphate dehydrogenase (GAPDH) housekeeping gene was used to normalize the mRNA expression of specific analyzed genes. The variation of gene expression was calculated by using the comparative threshold method (ΔΔCt = difference in ΔCt between LPS and Lipid A-treated cells and untreated cells) and the results are reported as the normalized fold expression through $2^{-\Delta\Delta Ct}$ quantification method by CFX Maestro™ Software, Version 2.3 (BioRad Laboratories, Italy). Primer sequences used in this experimental setup are reported in **Table 5.5**.

**Table 5.5** Oligonucleotide sequences used in this study.

| Gene Name (symbol) | PCR Primer Sequence 5′→ 3′ |
|---|---|
| Collagen 1A1 (COLI) | CCCTGAAGTCAGCTGCATACACAA<br>CCTACATCTTCTGAGTTTGGTGAT |
| Interleukin 6 (IL-6) | TCCATCCAGTTGCCTTCTTG<br>TTCCACGATTTCCCAGAGAAC |
| Toll-like receptor 4 (TLR-4) | ACACTTTATTCAGAGCCGTTGGT<br>CAGGTCCAAGTTGCCGTTTC |

Data are presented as mean± SD of three performed tests.

### 5.18.5 Collagen 1A1, NF-kB and caspase-4 protein expression evaluation through quantitative western blotting (WB).

The intracellular proteins were isolated (24 h incubation with LPSs or Lipids A) using a radio-immunoprecipitation assay (RIPA buffer, Thermo Fisher Scientific, Waltham, USA) and quantified using Bradford reagent (BioRad Laboratories, Milan, Italy). 20 µg of total proteins were separated by SDS-PAGE 10% polyacrylamide gel and transferred to a nitrocellulose membrane (GE Healthcare, Amersham, UK). This latter was fixed with 5% non-fat milk in Tris-buffered saline with 0.05% Tween-20 (TTBS) for 15 min and incubated with primary antibodies against NF-*k*B, Caspase-4 and COLI (Santa Cruz Biotechnology, Dallas, USA, diluted 1:250), overnight at 4 °C. The next day, the membrane was washed with TTBS and incubated with specific horseradish peroxidase-conjugated anti-mouse and anti-rabbit antibodies (Santa Cruz Biotechnology, Dallas, USA, diluted 1:10000) for 1 h at room temperature. Relative blots were developed via the ECL system (Elabscience, Huston, USA), and GAPDH antibody (Santa Cruz Biotechnology, Dallas, USA, diluted 1:2000) was here employed as a gel loading control. Finally, the semi-quantitative protein expression analysis was accomplished through Image J software 1.8.0. Data are presented as mean± SD of three performed tests

### 5.18.6 IL-6 protein evaluation by ELISA assay

IL-6 secretion was quantified by ELISA (Elabscience, Huston, USA). In detail, cellular supernatants, after 24 h of treatment, were centrifuged to discard eventually detached cells and/or debris (2000 rpm for 10 min at 4 °C). Each sample was loaded on the plate in triplicate, and the cytokine-specific absorbance was measured through a microplate reader (Biorad Laboratories, Italy). Relative analytic concentrations were derived via a standard curve following the manufacturer's instructions. Data are presented as mean± SD of three performed tests.

## Final remarks and future perspectives

The present work has provided an integrated overview of bacterial glycans, highlighting their structural diversity, functional roles, and potential applications. The parallel study of *Pseudomonas aeruginosa* and *Psychrobacter* sp. TAE2020 offered a complementary perspective on the dual nature of surface glycoconjugates: on the one hand, they act as mediators of pathogenicity in clinical contexts, and on the other, as adaptive or bioactive molecules in extremophilic environments.

For *P. aeruginosa*, the data clearly demonstrated a remodelling of lipid A structure as a function of both growth conditions and antibiotic resistance profiles. The transition from a planktonic to a biofilm lifestyle, combined with the selective pressure exerted by antimicrobial treatments, resulted in chemical modifications, particularly in phosphorylation and acylation patterns. These results highlight the plasticity of lipid A as a key element in modulating immune response and antibiotic tolerance in chronic infections. Although lipid A represents the most conserved portion of LPS, it still undergoes functional remodelling that promotes bacterial survival within the biofilm, one of the main causes of recurrence and therapeutic resistance in *P. aeruginosa* infections.

**Future studies** should extend structural analysis to the LPS core and O-antigen regions to achieve a more comprehensive understanding of the molecular determinants associated with resistance and persistence in cystic fibrosis-related infections.

In the case of *Psychrobacter* sp. TAE2020, the isolation and structural characterization of the capsular polysaccharide (CPS) revealed a unique architecture based on aminosugars with marked hydrophobic features, explaining its strong emulsifying and antibiofilm activity. In parallel, the study of the lipopolysaccharide (LPS) confirmed the presence of a rough-type structure characterized by heterogeneous lipid A species, typical of cold-adapted bacteria. These findings strengthen the idea that glycan structural plasticity contributes to environmental adaptation under extreme conditions.

**Future research** should complete the structural elucidation of the LPS saccharidic portion and quantify the relative abundance of CPS and LPS within the CATASAN complex. This information will be essential to define structure-activity relationships and clarify the cooperative mechanisms underlying their bioactivity.

Finally, the preliminary results obtained with CPS-coated liposomes, together with the observation and isolation of extracellular membrane vesicles (EMVs) produced by *Psychrobacter* sp. TAE2020, opens new perspectives for biotechnological applications. These natural vesicular systems represent promising candidates for the development of nanocarriers, thanks to their biocompatibility, stability, and intrinsic antibiofilm properties. **Future investigations** will focus on the complete molecular characterization of these vesicles and on the evaluation of their potential as novel drug delivery systems in biomedical applications.

In conclusion, the combined study of pathogenic and extremophilic bacteria highlights how the structural flexibility of surface glycans underlies both virulence and adaptive capabilities. Understanding these molecular mechanisms not only broadens fundamental knowledge in glycobiology but also paves the way for innovative glycan-based strategies for controlling biofilm-associated infections and for designing natural nanocarriers with therapeutic potential.

## References

Abbass, A., Sharifuzzaman, S. M., & Austin, B. (2010). Cellular components of probiotics control *Yersinia ruckeri* infection in rainbow trout, *Oncorhynchus mykiss* (Walbaum). *Journal of Fish Diseases*, *33*(1), 31–37. https://doi.org/10.1111/j.1365-2761.2009.01086.x

Abid, Y., Azabou, S., Joulak, I., Casillo, A., Lanzetta, R., Corsaro, M. M., Gharsallaoui, A., & Attia, H. (2019). Potential biotechnological properties of an exopolysaccharide produced by newly isolated Bacillus tequilensis-GM from spontaneously fermented goat milk. *LWT*, *105*, 135–141. https://doi.org/10.1016/j.lwt.2019.02.005

Alam, & Jenkins. (2012). HR-MAS NMR Spectroscopy in Material Science. In M. Akhyar Farrukh (A c. Di), *Advanced Aspects of Spectroscopy*. InTech. https://doi.org/10.5772/48340

Alexander & Rietschel. (2001). *Bacterial lipopolysaccharides and innate immunity*.

Arciola, C. R., Campoccia, D., & Montanaro, L. (2002). Detection of biofilm-forming strains of Staphylococcus epidermidis and S. aureus. *Expert Review of Molecular Diagnostics*, *2*(5), 478–484. https://doi.org/10.1586/14737159.2.5.478

Armbruster, C. R., Wolter, D. J., Mishra, M., Hayden, H. S., Radey, M. C., Merrihew, G., MacCoss, M. J., Burns, J., Wozniak, D. J., Parsek, M. R., & Hoffman, L. R. (2016). Staphylococcus aureus Protein A Mediates Interspecies Interactions at the Cell Surface of Pseudomonas aeruginosa. *mBio*, *7*(3), e00538-16. https://doi.org/10.1128/mBio.00538-16

Artini, M., Papa, R., Vrenna, G., Lauro, C., Ricciardelli, A., Casillo, A., Corsaro, M. M., Tutino, M. L., Parrilli, E., & Selan, L. (2019). Cold-Adapted Bacterial Extracts as a Source of Anti-Infective and Antimicrobial Compounds against *Staphylococcus*

*Aureus*. *Future Microbiology*, *14*(16), 1369–1382. https://doi.org/10.2217/fmb-2019-0147

Beaudoin, T., Yau, Y. C. W., Stapleton, P. J., Gong, Y., Wang, P. W., Guttman, D. S., & Waters, V. (2017). Staphylococcus aureus interaction with Pseudomonas aeruginosa biofilm enhances tobramycin resistance. *Npj Biofilms and Microbiomes*, *3*(1), 25. https://doi.org/10.1038/s41522-017-0035-0

Berk, V., Fong, J. C. N., Dempsey, G. T., Develioglu, O. N., Zhuang, X., Liphardt, J., Yildiz, F. H., & Chu, S. (2012). Molecular Architecture and Assembly Principles of *Vibrio cholerae* Biofilms. *Science*, *337*(6091), 236–239. https://doi.org/10.1126/science.1222981

Bernal-Bayard, J., Thiebaud, J., Brossaud, M., Beaussart, A., Caillet, C., Waldvogel, Y., Travier, L., Létoffé, S., Fontaine, T., Rokbi, B., Talaga, P., Beloin, C., Mistretta, N., Duval, J. F. L., & Ghigo, J.-M. (2023). Bacterial capsular polysaccharides with antibiofilm activity share common biophysical and electrokinetic properties. *Nature Communications*, *14*(1), 2553. https://doi.org/10.1038/s41467-023-37925-8

Beutler, B. (2000). Tlr4: Central component of the sole mammalian LPS sensor. *Current Opinion in Immunology*, *12*(1), 20–26. https://doi.org/10.1016/S0952-7915(99)00046-1

Bjarnsholt, T., Jensen, P. Ø., Fiandaca, M. J., Pedersen, J., Hansen, C. R., Andersen, C. B., Pressler, T., Givskov, M., & Høiby, N. (2009). *Pseudomonas aeruginosa* biofilms in the respiratory tract of cystic fibrosis patients. *Pediatric Pulmonology*, *44*(6), 547–558. https://doi.org/10.1002/ppul.21011

Blesic, M., Dichiarante, V., Milani, R., Linder, M., & Metrangolo, P. (2018). Evaluating the potential of natural surfactants in the petroleum industry: The case of hydrophobins.

*Pure and Applied Chemistry*, *90*(2), 305–314. https://doi.org/10.1515/pac-2017-0703

Bligh, E. G., & Dyer, W. J. (1959). A RAPID METHOD OF TOTAL LIPID EXTRACTION AND PURIFICATION. *Canadian Journal of Biochemistry and Physiology*, *37*(8), 911–917. https://doi.org/10.1139/o59-099

Bock, K., & Pedersen, C. (1983). Carbon-13 Nuclear Magnetic Resonance Spectroscopy of Monosaccharides. In *Advances in Carbohydrate Chemistry and Biochemistry* (Vol. 41, pp. 27–66). Elsevier. https://doi.org/10.1016/S0065-2318(08)60055-4

Bock, K., & Pedersen, C. (1985). Determination of one-bond carbon-proton coupling constants through 13C-satellites in 1H-n.m.r. Spectra. *Carbohydrate Research*, *145*(1), 135–140. https://doi.org/10.1016/S0008-6215(00)90420-8

Bucher, T., Oppenheimer-Shaanan, Y., Savidor, A., Bloom-Ackermann, Z., & Kolodkin-Gal, I. (2015). Disturbance of the bacterial cell wall specifically interferes with biofilm formation. *Environmental Microbiology Reports*, *7*(6), 990–1004. https://doi.org/10.1111/1758-2229.12346

Cámara, M., Green, W., MacPhee, C. E., Rakowska, P. D., Raval, R., Richardson, M. C., Slater-Jefferies, J., Steventon, K., & Webb, J. S. (2022). Economic significance of biofilms: A multidisciplinary and cross-sectoral challenge. *Npj Biofilms and Microbiomes*, *8*(1), 42. https://doi.org/10.1038/s41522-022-00306-y

Carillo, S., Casillo, A., Pieretti, G., Parrilli, E., Sannino, F., Bayer-Giraldi, M., Cosconati, S., Novellino, E., Ewert, M., Deming, J. W., Lanzetta, R., Marino, G., Parrilli, M., Randazzo, A., Tutino, M. L., & Corsaro, M. M. (2015). A Unique Capsular Polysaccharide Structure from the Psychrophilic Marine Bacterium *Colwellia*

*psychrerythraea* 34H That Mimics Antifreeze (Glyco)proteins. *Journal of the American Chemical Society*, *137*(1), 179–189. https://doi.org/10.1021/ja5075954

Casillo, A., D'Amico, R., Lanzetta, R., & Corsaro, M. M. (2024). Marine Delivery Vehicles: Molecular Components and Applications of Bacterial Extracellular Vesicles. *Marine Drugs*, *22*(8), 363. https://doi.org/10.3390/md22080363

Casillo, A., Di Guida, R., Cavasso, D., Stellavato, A., Rai, D., Yokoyama, F., Kamasaka, K., Kawamoto, J., Kurihara, T., Schiraldi, C., Kulkarni, S., Paduano, L., & Corsaro, M. M. (2022). Polysaccharide corona: The acetyl-rich envelope wraps the extracellular membrane vesicles and the cells of Shewanella vesiculosa providing adhesiveness. *Carbohydrate Polymers*, *297*, 120036. https://doi.org/10.1016/j.carbpol.2022.120036

Casillo, A., Fabozzi, A., Russo Krauss, I., Parrilli, E., Biggs, C. I., Gibson, M. I., Lanzetta, R., Appavou, M.-S., Radulescu, A., Tutino, M. L., Paduano, L., & Corsaro, M. M. (2021). Physicochemical Approach to Understanding the Structure, Conformation, and Activity of Mannan Polysaccharides. *Biomacromolecules*, *22*(4), 1445–1457. https://doi.org/10.1021/acs.biomac.0c01659

Casillo, A., Ziaco, M., Lindner, B., Parrilli, E., Schwudke, D., Holgado, A., Beyaert, R., Lanzetta, R., Tutino, M. L., & Corsaro, M. M. (2018). Lipid A structural characterization from the LPS of the Siberian psychro-tolerant Psychrobacter arcticus 273-4 grown at low temperature. *Extremophiles*, *22*(6), 955–963. https://doi.org/10.1007/s00792-018-1051-6

Casillo, A., Ziaco, M., Lindner, B., Parrilli, E., Schwudke, D., Holgado, A., Verstrepen, L., Sannino, F., Beyaert, R., Lanzetta, R., Tutino, M. L., & Corsaro, M. M. (2017). Unusual Lipid A from a Cold-Adapted Bacterium: Detailed Structural

Characterization. *ChemBioChem*, *18*(18), 1845–1854. https://doi.org/10.1002/cbic.201700287

Chalabaev, S., Chauhan, A., Novikov, A., Iyer, P., Szczesny, M., Beloin, C., Caroff, M., & Ghigo, J.-M. (2014). Biofilms Formed by Gram-Negative Bacteria Undergo Increased Lipid A Palmitoylation, Enhancing *In Vivo* Survival. *mBio*, *5*(4), e01116-14. https://doi.org/10.1128/mBio.01116-14

Chan, S., & Reinhold, V. N. (1994). Detailed Structural Characterization of Lipid A: Electrospray Ionization Coupled with Tandem Mass-Spectrometry. *Analytical Biochemistry*, *218*(1), 63–73. https://doi.org/10.1006/abio.1994.1141

Chmiel, J. F., Berger, M., & Konstan, M. W. (2002). The Role of Inflammation in the Pathophysiology of CF Lung Disease. *Clinical Reviews in Allergy & Immunology*, *23*(1), 005–028. https://doi.org/10.1385/CRIAI:23:1:005

Choi, K. Y., Saravanakumar, G., Park, J. H., & Park, K. (2012). Hyaluronic acid-based nanocarriers for intracellular targeting: Interfacial interactions with proteins in cancer. *Colloids and Surfaces B: Biointerfaces*, *99*, 82–94. https://doi.org/10.1016/j.colsurfb.2011.10.029

Colvin, K. M., Irie, Y., Tart, C. S., Urbano, R., Whitney, J. C., Ryder, C., Howell, P. L., Wozniak, D. J., & Parsek, M. R. (2012). The Pel and Psl polysaccharides provide *Pseudomonas aeruginosa* structural redundancy within the biofilm matrix. *Environmental Microbiology*, *14*(8), 1913–1928. https://doi.org/10.1111/j.1462-2920.2011.02657.x

Corsaro, M. M., De Castro, C., Evidente, A., Lanzetta, R., Lavermicocca, P., Molinaro, A., Sisto, A., Parrilli, M., & Surico, G. (1997). Lipopolysaccharides from three

phytopathogenic pseudomonads. *Phytochemistry*, *46*(2), 289–292. https://doi.org/10.1016/S0031-9422(97)00274-4

Corsaro, M. M., Grant, W. D., Grant, S., Marciano, C. E., & Parrilli, M. (1999). Structure determination of an exopolysaccharide from an alkaliphilic bacterium closely related to *Bacillus* spp. *European Journal of Biochemistry*, *264*(2), 554–561. https://doi.org/10.1046/j.1432-1327.1999.00672.x

Corsaro, M. M., Piaz, F. D., Lanzetta, R., & Parrilli, M. (2002). Lipid A structure of *Pseudoalteromonas haloplanktis* TAC 125: Use of electrospray ionization tandem mass spectrometry for the determination of fatty acid distribution. *Journal of Mass Spectrometry*, *37*(5), 481–488. https://doi.org/10.1002/jms.304

Costerton, J. W., Stewart, P. S., & Greenberg, E. P. (1999). Bacterial Biofilms: A Common Cause of Persistent Infections. *Science*, *284*(5418), 1318–1322. https://doi.org/10.1126/science.284.5418.1318

Coulon, C., Vinogradov, E., Filloux, A., & Sadovskaya, I. (2010). Chemical Analysis of Cellular and Extracellular Carbohydrates of a Biofilm-Forming Strain Pseudomonas aeruginosa PA14. *PLoS ONE*, *5*(12), e14220. https://doi.org/10.1371/journal.pone.0014220

Cramton, S. E., Gerke, C., Schnell, N. F., Nichols, W. W., & Götz, F. (1999). The Intercellular Adhesion ( *ica* ) Locus Is Present in *Staphylococcus aureus* and Is Required for Biofilm Formation. *Infection and Immunity*, *67*(10), 5427–5433. https://doi.org/10.1128/IAI.67.10.5427-5433.1999

D'Amico, R., Casillo, A., Olimpo, D., Gallucci, N., D'Angelo, C., Tutino, M. L., Paduano, L., Parrilli, E., & Corsaro, M. M. (2025). Capsular polysaccharide from Psychrobacter sp. TAE2020: An unusual amino sugar-enriched macromolecule with

anti-biofilm and emulsification activities. *Carbohydrate Polymers*, 124484. https://doi.org/10.1016/j.carbpol.2025.124484

Dams-Kozlowska, H., Mercaldi, M. P., Panilaitis, B. J., & Kaplan, D. L. (2008). Modifications and applications of the Acinetobacter venetianus RAG-1 exopolysaccharide, the emulsan complex and its components. *Applied Microbiology and Biotechnology*, *81*(2), 201–210. https://doi.org/10.1007/s00253-008-1664-2

D'Angelo, C., Casillo, A., Melchiorre, C., Lauro, C., Corsaro, M. M., Carpentieri, A., Tutino, M. L., & Parrilli, E. (2022). CATASAN Is a New Anti-Biofilm Agent Produced by the Marine Antarctic Bacterium Psychrobacter sp. TAE2020. *Marine Drugs*, *20*(12), 747. https://doi.org/10.3390/md20120747

De Maayer, P., Anderson, D., Cary, C., & Cowan, D. A. (2014). Some like it cold: Understanding the survival strategies of psychrophiles. *EMBO Reports*, *15*(5), 508–517. https://doi.org/10.1002/embr.201338170

Decho, A. W., & Gutierrez, T. (2017). Microbial Extracellular Polymeric Substances (EPSs) in Ocean Systems. *Frontiers in Microbiology*, *8*, 922. https://doi.org/10.3389/fmicb.2017.00922

Deming, J. W., Young, J. N., & Margesin, R. (2017). *From Biodiversity to Biotechnology* (2, A c. Di).

Di Guida, R., Casillo, A., & Corsaro, M. M. (2020). O-specific polysaccharide structure isolated from the LPS of the Antarctic bacterium Pseudomonas ANT_J38B. *Carbohydrate Research*, *497*, 108125. https://doi.org/10.1016/j.carres.2020.108125

Di Guida, R., Casillo, A., Stellavato, A., Kawai, S., Ogawa, T., Di Meo, C., Kawamoto, J., Kurihara, T., Schiraldi, C., & Corsaro, M. M. (2022). Capsular polysaccharide from a fish-gut bacterium induces/promotes apoptosis of colon cancer cells in vitro

through Caspases' pathway activation. *Carbohydrate Polymers*, *278*, 118908. https://doi.org/10.1016/j.carbpol.2021.118908

Domon, B., & Costello, C. E. (1988). A systematic nomenclature for carbohydrate fragmentations in FAB-MS/MS spectra of glycoconjugates. *Glycoconjugate Journal*, *5*(4), 397–409. https://doi.org/10.1007/BF01049915

Domon & Vath. (1990). [40] Tandem mass spectrometry of glycolipids. In *Methods in Enzymology* (Vol. 193, pp. 738–768). Elsevier. https://doi.org/10.1016/0076-6879(90)93448-T

Drouillard, S., Jeacomine, I., Buon, L., Boisset, C., Courtois, A., Thollas, B., Morvan, P.-Y., Vallée, R., & Helbert, W. (2018). Structure of the Exopolysaccharide Secreted by a Marine Strain Vibrio alginolyticus. *Marine Drugs*, *16*(5), 164. https://doi.org/10.3390/md16050164

Elborn, J. S., Ramsey, B. W., Boyle, M. P., Konstan, M. W., Huang, X., Marigowda, G., Waltz, D., & Wainwright, C. E. (2016). Efficacy and safety of lumacaftor/ivacaftor combination therapy in patients with cystic fibrosis homozygous for Phe508del CFTR by pulmonary function subgroup: A pooled analysis. *The Lancet Respiratory Medicine*, *4*(8), 617–626. https://doi.org/10.1016/S2213-2600(16)30121-7

Ernst, R. K., Moskowitz, S. M., Emerson, J. C., Kraig, G. M., Adams, K. N., Harvey, M. D., Ramsey, B., Speert, D. P., Burns, J. L., & Miller, S. I. (2007). Unique Lipid A Modifications in *Pseudomonas aeruginosa* Isolated from the Airways of Patients with Cystic Fibrosis. *The Journal of Infectious Diseases*, *196*(7), 1088–1092. https://doi.org/10.1086/521367

Escalera, L., Benvenuto, G., Scalco, E., Zingone, A., & Montresor, M. (2014). Ultrastructural Features of the Benthic Dinoflagellate Ostreopsis cf. Ovata (Dinophyceae). *Protist*, *165*(3), 260–274. https://doi.org/10.1016/j.protis.2014.03.001

Fedtke, I., Mader, D., Kohler, T., Moll, H., Nicholson, G., Biswas, R., Henseler, K., Götz, F., Zähringer, U., & Peschel, A. (2007). A *Staphylococcus aureus ypfP* mutant with strongly reduced lipoteichoic acid (LTA) content: LTA governs bacterial surface properties and autolysin activity. *Molecular Microbiology*, *65*(4), 1078–1091. https://doi.org/10.1111/j.1365-2958.2007.05854.x

Flemming, H.-C., Wingender, J., Szewzyk, U., Steinberg, P., Rice, S. A., & Kjelleberg, S. (2016). Biofilms: An emergent form of bacterial life. *Nature Reviews Microbiology*, *14*(9), 563–575. https://doi.org/10.1038/nrmicro.2016.94

Franklin, M. J., Nivens, D. E., Weadge, J. T., & Howell, P. L. (2011). Biosynthesis of the Pseudomonas aeruginosa Extracellular Polysaccharides, Alginate, Pel, and Psl. *Frontiers in Microbiology*, *2*. https://doi.org/10.3389/fmicb.2011.00167

Fresno, S., Jiménez, N., Canals, R., Merino, S., Corsaro, M. M., Lanzetta, R., Parrilli, M., Pieretti, G., Regué, M., & Tomás, J. M. (2007). A Second Galacturonic Acid Transferase Is Required for Core Lipopolysaccharide Biosynthesis and Complete Capsule Association with the Cell Surface in *Klebsiella pneumoniae*. *Journal of Bacteriology*, *189*(3), 1128–1137. https://doi.org/10.1128/JB.01489-06

Galanos, C., Lüderitz, O., & Westphal, O. (1969). A New Method for the Extraction of R Lipopolysaccharides. *European Journal of Biochemistry*, *9*(2), 245–249. https://doi.org/10.1111/j.1432-1033.1969.tb00601.x

Gallucci, N., Appavou, M.-S., Cowieson, N., D'Errico, G., Di Girolamo, R., Lettieri, S., Sica, F., Vitiello, G., & Paduano, L. (2024). Ordered hierarchical superlattice

amplifies coated-CeO2 nanoparticles luminescence. *Journal of Colloid and Interface Science*, *659*, 926–935. https://doi.org/10.1016/j.jcis.2024.01.029

Gallucci, N., Krauss, I. R., D'Errico, G., & Paduano, L. (2023). Pulmonary surfactant's interaction with nanocarriers: Nanoscale structural and functional effects. *Current Opinion in Colloid & Interface Science*, *67*, 101727. https://doi.org/10.1016/j.cocis.2023.101727

Gan, M., Zheng, X., Gan, L., Guan, Y., Hao, X., Liu, Y., Si, S., Zhang, Y., Yu, L., & Xiao, C. (2011). Streptothricin Derivatives from *Streptomyces* sp . I08A 1776. *Journal of Natural Products*, *74*(5), 1142–1147. https://doi.org/10.1021/np2000733

Garegg, P. J., Lindberg, B., & Kvarnström, I. (1979). Preparation and N.M.R. studies of pyruvic acid and related acetals of pyranosides: Configuration at the acetal carbon atoms. *Carbohydrate Research*, *77*(1), 71–78. https://doi.org/10.1016/S0008-6215(00)83794-5

Gellatly, S. L., & Hancock, R. E. W. (2013). *Pseudomonas aeruginosa*: New insights into pathogenesis and host defenses. *Pathogens and Disease*, *67*(3), 159–173. https://doi.org/10.1111/2049-632X.12033

Govan, J. R., & Deretic, V. (1996). Microbial pathogenesis in cystic fibrosis: Mucoid Pseudomonas aeruginosa and Burkholderia cepacia. *Microbiological Reviews*, *60*(3), 539–574. https://doi.org/10.1128/mr.60.3.539-574.1996

Gowrishankar, S., & Pandian, S. K. (2017). Modulation of Staphylococcus epidermidis (RP62A) extracellular polymeric layer by marine cyclic dipeptide-cyclo( l -leucyl- l -prolyl) thwarts biofilm formation. *Biochimica et Biophysica Acta (BBA) - Biomembranes*, *1859*(7), 1254–1262. https://doi.org/10.1016/j.bbamem.2017.04.009

Gozdziewicz, T. K., Maciejewska, A., Tsybulska, A., Lugowski, C., & Lukasiewicz, J. (2021). A New Look at the Enterobacterial Common Antigen Forms Obtained during Rough Lipopolysaccharides Purification. *International Journal of Molecular Sciences*, *22*(2), 701. https://doi.org/10.3390/ijms22020701

Hancock, R. E., Mutharia, L. M., Chan, L., Darveau, R. P., Speert, D. P., & Pier, G. B. (1983). Pseudomonas aeruginosa isolates from patients with cystic fibrosis: A class of serum-sensitive, nontypable strains deficient in lipopolysaccharide O side chains. *Infection and Immunity*, *42*(1), 170–177. https://doi.org/10.1128/iai.42.1.170-177.1983

Hauser, A. R., Jain, M., Bar-Meir, M., & McColley, S. A. (2011). Clinical Significance of Microbial Infection and Adaptation in Cystic Fibrosis. *Clinical Microbiology Reviews*, *24*(1), 29–70. https://doi.org/10.1128/CMR.00036-10

Heacock-Kang, Y., Zarzycki-Siek, J., Sun, Z., Poonsuk, K., Bluhm, A. P., Cabanas, D., Fogen, D., McMillan, I. A., Chuanchuen, R., & Hoang, T. T. (2018). Novel dual regulators of *Pseudomonas aeruginosa* essential for productive biofilms and virulence. *Molecular Microbiology*, *109*(3), 401–414. https://doi.org/10.1111/mmi.14063

Heilmann, C., Gerke, C., Perdreau-Remington, F., & Götz, F. (1996). Characterization of Tn917 insertion mutants of Staphylococcus epidermidis affected in biofilm formation. *Infection and Immunity*, *64*(1), 277–282. https://doi.org/10.1128/iai.64.1.277-282.1996

Holst, O. (2000). Deacylation of Lipopolysaccharides and Isolation of Oligosaccharide Phosphates. In O. Holst, *Bacterial Toxins* (Vol. 145, pp. 345–353). Humana Press. https://doi.org/10.1385/1-59259-052-7:345

Hsu, F.-F., & Turk, J. (2000). Charge-remote and charge-driven fragmentation processes in diacyl glycerophosphoethanolamine upon low-energy collisional activation: A mechanistic proposal. *Journal of the American Society for Mass Spectrometry*, *11*(10), 892–899. https://doi.org/10.1016/S1044-0305(00)00159-8

Jansson, P.-E., Kenne, L., & Widmalm, G. (1989). Computer-assisted structural analysis of polysaccharides with an extended version of casper using 1H- and 13C-n.m.r. Data. *Carbohydrate Research*, *188*, 169–191. https://doi.org/10.1016/0008-6215(89)84069-8

Jennings, L. K., Dreifus, J. E., Reichhardt, C., Storek, K. M., Secor, P. R., Wozniak, D. J., Hisert, K. B., & Parsek, M. R. (2021). Pseudomonas aeruginosa aggregates in cystic fibrosis sputum produce exopolysaccharides that likely impede current therapies. *Cell Reports*, *34*(8), 108782. https://doi.org/10.1016/j.celrep.2021.108782

Kaplan, J. B. (2010). Biofilm Dispersal: Mechanisms, Clinical Implications, and Potential Therapeutic Uses. *Journal of Dental Research*, *89*(3), 205–218. https://doi.org/10.1177/0022034509359403

Karn, P. R., Vanić, Z., Pepić, I., & Škalko-Basnet, N. (2011). Mucoadhesive liposomal delivery systems: The choice of coating material. *Drug Development and Industrial Pharmacy*, *37*(4), 482–488. https://doi.org/10.3109/03639045.2010.523425

Kaye, W., & Havlik, A. J. (1973). Low Angle Laser Light Scattering—Absolute Calibration. *Applied Optics*, *12*(3), 541. https://doi.org/10.1364/AO.12.000541

Knirel, Y. A., Bystrova, O. V., Kocharova, N. A., Zähringer, U., & Pier, G. B. (2006). Conserved and variable structural features in the lipopolysaccharide of <I>Pseudomonas aeruginosa</I>. *Journal of Endotoxin Research*, *12*(6), 324–336. https://doi.org/10.1179/096805106X118906

Knirel, Y. A., Naumenko, O. I., Senchenkova, S. N., & Perepelov, A. V. (2019). Chemical methods for selective cleavage of glycosidic bonds in the structural analysis of bacterial polysaccharides. *Russian Chemical Reviews*, *88*(4), 406–424. https://doi.org/10.1070/RCR4856

Kocharova, N. A., Perepelov, A. V., Zatonsky, G. V., Shashkov, A. S., Knirel, Y. A., Jansson, P.-E., & Weintraub, A. (2001). Structural studies of the O-specific polysaccharide of Vibriocholerae O8 using solvolysis with triflic acid. *Carbohydrate Research*, *330*(1), 83–92. https://doi.org/10.1016/S0008-6215(00)00271-8

Kokoulin, M. S., Kuzmich, A. S., Romanenko, L. A., & Chikalovets, I. V. (2021). Structure and in vitro antiproliferative activity of the acidic capsular polysaccharide from the deep-sea bacterium Psychrobacter submarinus KMM 225T. *Carbohydrate Polymers*, *262*, 117941. https://doi.org/10.1016/j.carbpol.2021.117941

Kondakova, A. N., Novototskaya-Vlasova, K. A., Drutskaya, M. S., Senchenkova, S. N., Shcherbakova, V. A., Shashkov, A. S., Gilichinsky, D. A., Nedospasov, S. A., & Knirel, Y. A. (2012). Structure of the O-polysaccharide chain of the lipopolysaccharide of Psychrobacter muricolla 2pST isolated from overcooled water brines within permafrost. *Carbohydrate Research*, *349*, 78–81. https://doi.org/10.1016/j.carres.2011.11.027

Kulp, A., & Kuehn, M. J. (2010). Biological Functions and Biogenesis of Secreted Bacterial Outer Membrane Vesicles. *Annual Review of Microbiology*, *64*(1), 163–184. https://doi.org/10.1146/annurev.micro.091208.073413

Kuschmierz, L., Meyer, M., Bräsen, C., Wingender, J., Schmitz, O. J., & Siebers, B. (2022). Exopolysaccharide composition and size in Sulfolobus acidocaldarius biofilms. *Frontiers in Microbiology*, *13*, 982745. https://doi.org/10.3389/fmicb.2022.982745

Kussak, A., & Weintraub, A. (2002). Quadrupole ion-trap mass spectrometry to locate fatty acids on lipid A from Gram-negative bacteria. *Analytical Biochemistry*, *307*(1), 131–137. https://doi.org/10.1016/S0003-2697(02)00004-0

Laemmli, U. K. (1970). Cleavage of Structural Proteins during the Assembly of the Head of Bacteriophage T4. *Nature*, *227*(5259), 680–685. https://doi.org/10.1038/227680a0

Laemmli, U. K., & Favre, M. (1973). Maturation of the head of bacteriophage T4. *Journal of Molecular Biology*, *80*(4), 575–599. https://doi.org/10.1016/0022-2836(73)90198-8

Laezza, A., Casillo, A., Cosconati, S., Biggs, C. I., Fabozzi, A., Paduano, L., Iadonisi, A., Novellino, E., Gibson, M. I., Randazzo, A., Corsaro, M. M., & Bedini, E. (2017). Decoration of Chondroitin Polysaccharide with Threonine: Synthesis, Conformational Study, and Ice-Recrystallization Inhibition Activity. *Biomacromolecules*, *18*(8), 2267–2276. https://doi.org/10.1021/acs.biomac.7b00326

Lee, C., Kim, Y., Joo, H., & Kim, B. (2004). Structural analysis of lipid A from *Escherichia coli* O157:H7:K$^{-}$ using thin-layer chromatography and ion-trap mass spectrometry. *Journal of Mass Spectrometry*, *39*(5), 514–525. https://doi.org/10.1002/jms.614

Lee, J., Jayaraman, A., & Wood, T. K. (2007). Indole is an inter-species biofilm signal mediated by SdiA. *BMC Microbiology*, *7*(1), 42. https://doi.org/10.1186/1471-2180-7-42

Leontein, K., Lindberg, B., & Lönngren, J. (1978). Assignment of absolute configuration of sugars by g.l.c. Of their acetylated glycosides formed from chiral alcohols. *Carbohydrate Research*, *62*(2), 359–362. https://doi.org/10.1016/S0008-6215(00)80882-4

Li, Z., Wang, L., Lin, X., Shen, L., & Feng, Y. (2017). Drug delivery for bioactive polysaccharides to improve their drug-like properties and curative efficacy. *Drug Delivery*, *24*(2), 70–80. https://doi.org/10.1080/10717544.2017.1396383

Lipkind, G. M., Shashkov, A. S., Knirel, Y. A., Vinogradov, E. V., & Kochetkov, N. K. (1988). A computer-assisted structural analysis of regular polysaccharides on the basis of 13C-n.m.r. Data. *Carbohydrate Research*, *175*(1), 59–75. https://doi.org/10.1016/0008-6215(88)80156-3

Lukasiewicz, J., Dzieciatkowska, M., Niedziela, T., Jachymek, W., Augustyniuk, A., Kenne, L., & Lugowski, C. (2006). Complete Lipopolysaccharide of *Plesiomonas shigelloides* O74:H5 (Strain CNCTC 144/92). 2. Lipid A, Its Structural Variability, the Linkage to the Core Oligosaccharide, and the Biological Activity of the Lipopolysaccharide·. *Biochemistry*, *45*(35), 10434–10447. https://doi.org/10.1021/bi060774d

Macarie, L., Pekar, M., Simulescu, V., Plesu, N., Iliescu, S., Ilia, G., & Tara-Lunga-Mihali, M. (2017). Properties in aqueous solution of homo- and copolymers of vinylphosphonic acid derivatives obtained by UV-curing. *Macromolecular Research*, *25*(3), 214–221. https://doi.org/10.1007/s13233-017-5026-8

Madigan, M. T., Kempher, M. L., Bender, K. S., Sullivan, P., Matthew Sattley, W., Dohnalkova, A. C., & Joye, S. B. (2017). Characterization of a cold-active bacterium isolated from the South Pole “Ice Tunnel”. *Extremophiles*, *21*(5), 891–901. https://doi.org/10.1007/s00792-017-0950-2

Makin, S. A., & Beveridge, T. J. (1996). The influence of A-band and B-band lipopolysaccharide on the surface characteristics and adhesion of Pseudomonas

aeruginosa to surfaces. *Microbiology*, *142*(2), 299–307. https://doi.org/10.1099/13500872-142-2-299

Mathee, K., Ciofu, O., Sternberg, C., Lindum, P. W., Campbell, J. I. A., Jensen, P., Johnsen, A. H., Givskov, M., Ohman, D. E., Søren, M., Høiby, N., & Kharazmi, A. (1999). Mucoid conversion of Pseudomonas aeruginos by hydrogen peroxide: A mechanism for virulence activation in the cystic fibrosis lung. *Microbiology*, *145*(6), 1349–1357. https://doi.org/10.1099/13500872-145-6-1349

Mauch, R. M., Jensen, P. Ø., Moser, C., Levy, C. E., & Høiby, N. (2018). Mechanisms of humoral immune response against Pseudomonas aeruginosa biofilm infection in cystic fibrosis. *Journal of Cystic Fibrosis*, *17*(2), 143–152. https://doi.org/10.1016/j.jcf.2017.08.012

Michaelis, C., & Grohmann, E. (2023). Horizontal Gene Transfer of Antibiotic Resistance Genes in Biofilms. *Antibiotics*, *12*(2), 328. https://doi.org/10.3390/antibiotics12020328

Mukherjee, S., Das, P., & Sen, R. (2006). Towards commercial production of microbial surfactants. *Trends in Biotechnology*, *24*(11), 509–515. https://doi.org/10.1016/j.tibtech.2006.09.005

Nguyen, M. P., Tran, L. V. H., Namgoong, H., & Kim, Y.-H. (2019). Applications of different solvents and conditions for differential extraction of lipopolysaccharide in Gram-negative bacteria. *Journal of Microbiology*, *57*(8), 644–654. https://doi.org/10.1007/s12275-019-9116-5

Nichols, C. M., Lardière, S. G., Bowman, J. P., Nichols, P. D., A.E. Gibson, J., & Guézennec, J. (2005). Chemical Characterization of Exopolysaccharides from Antarctic Marine

Bacteria. *Microbial Ecology*, *49*(4), 578–589. https://doi.org/10.1007/s00248-004-0093-8

Ober, M. F., Müller-Deku, A., Baptist, A., Ajanović, B., Amenitsch, H., Thorn-Seshold, O., & Nickel, B. (2022). SAXS measurements of azobenzene lipid vesicles reveal buffer-dependent photoswitching and quantitative *Z*→*E* isomerisation by X-rays. *Nanophotonics*, *11*(10), 2361–2368. https://doi.org/10.1515/nanoph-2022-0053

Olaitan, A. O., Morand, S., & Rolain, J.-M. (2014). Mechanisms of polymyxin resistance: Acquired and intrinsic resistance in bacteria. *Frontiers in Microbiology*, *5*. https://doi.org/10.3389/fmicb.2014.00643

Paduano, L., Sartorio, R., Vitagliano, V., Albright, J. G., & Miller, D. G. (1992). Measurement of the mutual diffusion coefficients at one composition of the four-component system α-cyclodextrin-l-phenylalanine-monobutylurea-H2O at 25 °C. *J. Phys. Chem. A*, *96*, 7478.

Pai, L., Patil, S., Liu, S., & Wen, F. (2023). A growing battlefield in the war against biofilm-induced antimicrobial resistance: Insights from reviews on antibiotic resistance. *Frontiers in Cellular and Infection Microbiology*, *13*, 1327069. https://doi.org/10.3389/fcimb.2023.1327069

Papa, R., Imperlini, E., Trecca, M., Paris, I., Vrenna, G., Artini, M., & Selan, L. (2023). Virulence of Pseudomonas aeruginosa in Cystic Fibrosis: Relationships between Normoxia and Anoxia Lifestyle. *Antibiotics*, *13*(1), 1. https://doi.org/10.3390/antibiotics13010001

Parsek, M. R., & Singh, P. K. (2003). Bacterial Biofilms: An Emerging Link to Disease Pathogenesis. *Annual Review of Microbiology*, *57*(1), 677–701. https://doi.org/10.1146/annurev.micro.57.030502.090720

Peng, P., Chen, Z., Wang, M., Wen, B., & Deng, X. (2023). Polysaccharide-modified liposomes and their application in cancer research. *Chemical Biology & Drug Design*, *101*(4), 998–1011. https://doi.org/10.1111/cbdd.14201

Perepelov, A. V., Senchenkova, S. N., Cedzynski, M., Ziolkowski, A., Vinogradov, E. V., Kaca, W., Shashkov, A. S., & Knirel, Y. A. (2000). Isolation using triflic acid solvolysis and identification of Nε-[(R)-1-carboxyethyl]-Nα-(d-galacturonoyl)-l-lysine as a component of the O-specific polysaccharide of Proteusmirabilis O13. *Carbohydrate Research*, *328*(3), 441–444. https://doi.org/10.1016/S0008-6215(00)00106-3

Perfetti, M., Gallucci, N., Russo Krauss, I., Radulescu, A., Pasini, S., Holderer, O., D'Errico, G., Vitiello, G., Bianchetti, G. O., & Paduano, L. (2020a). Revealing the Aggregation Mechanism, Structure, and Internal Dynamics of Poly(vinyl alcohol) Microgel Prepared through Liquid–Liquid Phase Separation. *Macromolecules*, *53*(3), 852–861. https://doi.org/10.1021/acs.macromol.9b02203

Perfetti, M., Gallucci, N., Russo Krauss, I., Radulescu, A., Pasini, S., Holderer, O., D'Errico, G., Vitiello, G., Bianchetti, G. O., & Paduano, L. (2020b). Revealing the Aggregation Mechanism, Structure, and Internal Dynamics of Poly(vinyl alcohol) Microgel Prepared through Liquid–Liquid Phase Separation. *Macromolecules*, *53*(3), 852–861. https://doi.org/10.1021/acs.macromol.9b02203

Perfumo, A., Banat, I. M., & Marchant, R. (2018). Going Green and Cold: Biosurfactants from Low-Temperature Environments to Biotechnology Applications. *Trends in Biotechnology*, *36*(3), 277–289. https://doi.org/10.1016/j.tibtech.2017.10.016

Peters, B. M., Jabra-Rizk, M. A., O'May, G. A., Costerton, J. W., & Shirtliff, M. E. (2012). Polymicrobial Interactions: Impact on Pathogenesis and Human Disease. *Clinical Microbiology Reviews*, *25*(1), 193–213. https://doi.org/10.1128/CMR.00013-11

Petersson, C., Niedziela, T., Jachymek, W., Kenne, L., Zarzecki, P., & Lugowski, C. (1997). Structural Studies of the O-Specific Polysaccharide of *Hafnia alvei* Strain PCM 1206 Lipopolysaccharide Containing D-Allothreonine. *European Journal of Biochemistry*, *244*(2), 580–586. https://doi.org/10.1111/j.1432-1033.1997.00580.x

Poltorak, A., He, X., Smirnova, I., Liu, M.-Y., Huffel, C. V., Du, X., Birdwell, D., Alejos, E., Silva, M., Galanos, C., Freudenberg, M., Ricciardi-Castagnoli, P., Layton, B., & Beutler, B. (1998). Defective LPS Signaling in C3H/HeJ and C57BL/10ScCr Mice: Mutations in *Tlr4* Gene. *Science*, *282*(5396), 2085–2088. https://doi.org/10.1126/science.282.5396.2085

Poole, K. (2011). Pseudomonas Aeruginosa: Resistance to the Max. *Frontiers in Microbiology*, *2*. https://doi.org/10.3389/fmicb.2011.00065

Pota, G., Gallucci, N., Cavasso, D., Krauss, I. R., Vitiello, G., López-Gallego, F., Costantini, A., Paduano, L., & Califano, V. (2023). Controlling the Adsorption of β-Glucosidase onto Wrinkled $SiO_2$ Nanoparticles To Boost the Yield of Immobilization of an Efficient Biocatalyst. *Langmuir*, *39*(4), 1482–1494. https://doi.org/10.1021/acs.langmuir.2c02861

Raetz, C. R. H., & Whitfield, C. (2002). Lipopolysaccharide Endotoxins. *Annual Review of Biochemistry*, *71*(1), 635–700. https://doi.org/10.1146/annurev.biochem.71.110601.135414

Ratjen, F. A. (2009). Cystic Fibrosis: Pathogenesis and Future Treatment Strategies. *Respiratory Care*, *54*(5), 595–605. https://doi.org/10.4187/aarc0427

Raue, S., Fan, S.-H., Rosenstein, R., Zabel, S., Luqman, A., Nieselt, K., & Götz, F. (2020). The Genome of Staphylococcus epidermidis O47. *Frontiers in Microbiology*, *11*, 2061. https://doi.org/10.3389/fmicb.2020.02061

Riccardi, C., D'Angelo, C., Calvanese, M., Ricciardelli, A., Tutino, M. L., Parrilli, E., & Fondi, M. (2022). Genome analysis of a new biosurfactants source: The Antarctic bacterium Psychrobacter sp. TAE2020. *Marine Genomics*, *61*, 100922. https://doi.org/10.1016/j.margen.2021.100922

Ricciardelli, A., Casillo, A., Corsaro, M. M., Tutino, M. L., Parrilli, E., & van der Mei, H. C. (2020). Pentadecanal and pentadecanoic acid coatings reduce biofilm formation of *Staphylococcus epidermidis* on PDMS. *Pathogens and Disease*, *78*(3), ftaa012. https://doi.org/10.1093/femspd/ftaa012

Ricciardelli, A., Casillo, A., Vergara, A., Balasco, N., Corsaro, M. M., Tutino, M. L., & Parrilli, E. (2019). Environmental conditions shape the biofilm of the Antarctic bacterium Pseudoalteromonas haloplanktis TAC125. *Microbiological Research*, *218*, 66–75. https://doi.org/10.1016/j.micres.2018.09.010

Russo Krauss, I., Picariello, A., Vitiello, G., De Santis, A., Koutsioubas, A., Houston, J. E., Fragneto, G., & Paduano, L. (2020). Interaction with Human Serum Proteins Reveals Biocompatibility of Phosphocholine-Functionalized SPIONs and Formation of Albumin-Decorated Nanoparticles. *Langmuir*, *36*(30), 8777–8791. https://doi.org/10.1021/acs.langmuir.0c01083

Ryder, C., Byrd, M., & Wozniak, D. J. (2007). Role of polysaccharides in Pseudomonas aeruginosa biofilm development. *Current Opinion in Microbiology*, *10*(6), 644–648. https://doi.org/10.1016/j.mib.2007.09.010

Schwechheimer, C., & Kuehn, M. J. (2015). Outer-membrane vesicles from Gram-negative bacteria: Biogenesis and functions. *Nature Reviews Microbiology*, *13*(10), 605–619. https://doi.org/10.1038/nrmicro3525

Scoffone, V. C., Chiarelli, L. R., Trespidi, G., Mentasti, M., Riccardi, G., & Buroni, S. (2017). Burkholderia cenocepacia Infections in Cystic Fibrosis Patients: Drug Resistance and Therapeutic Approaches. *Frontiers in Microbiology*, *8*, 1592. https://doi.org/10.3389/fmicb.2017.01592

Shaikh, M. O. F., Schaefers, M. M., Merakou, C., DiBlasi, M., Bonney, S., Liao, T., Zurakowski, D., Kehl, M., Tabor, D. E., DiGiandomenico, A., & Priebe, G. P. (2022). Multicomponent Pseudomonas aeruginosa Vaccines Eliciting Th17 Cells and Functional Antibody Responses Confer Enhanced Protection against Experimental Acute Pneumonia in Mice. *Infection and Immunity*, *90*(10), e00203-22. https://doi.org/10.1128/iai.00203-22

Söderman. (1998). *Synthesis, NMR spectroscopy and conformational studies of the four anomeric methyl glycosides of the trisaccharide D-Glc p-(1→ 3)-[D-Glc p-(1→ 4)]-α-D-Glc p*.

Srivastava, G. K., Alonso-Alonso, M. L., Fernandez-Bueno, I., Garcia-Gutierrez, M. T., Rull, F., Medina, J., Coco, R. M., & Pastor, J. C. (2018). Comparison between direct contact and extract exposure methods for PFO cytotoxicity evaluation. *Scientific Reports*, *8*(1), 1425. https://doi.org/10.1038/s41598-018-19428-5

Stewart, P. S. (2015). Antimicrobial Tolerance in Biofilms. *Microbiology Spectrum*, *3*(3), 3.3.07. https://doi.org/10.1128/microbiolspec.MB-0010-2014

Stover, C. K., Pham, X. Q., Erwin, A. L., Mizoguchi, S. D., Warrener, P., Hickey, M. J., Brinkman, F. S. L., Hufnagle, W. O., Kowalik, D. J., Lagrou, M., Garber, R. L.,

Goltry, L., Tolentino, E., Westbrock-Wadman, S., Yuan, Y., Brody, L. L., Coulter, S. N., Folger, K. R., Kas, A., … Olson, M. V. (2000). Complete genome sequence of Pseudomonas aeruginosa PAO1, an opportunistic pathogen. *Nature*, *406*(6799), 959–964. https://doi.org/10.1038/35023079

Sweet, C., Watson, R., Landis, C., & Smith, J. (2015). Temperature-Dependence of Lipid A Acyl Structure in Psychrobacter cryohalolentis and Arctic Isolates of Colwellia hornerae and Colwellia piezophila. *Marine Drugs*, *13*(8), 4701–4720. https://doi.org/10.3390/md13084701

Tripathi, L., Irorere, V. U., Marchant, R., & Banat, I. M. (2018). Marine derived biosurfactants: A vast potential future resource. *Biotechnology Letters*, *40*(11–12), 1441–1457. https://doi.org/10.1007/s10529-018-2602-8

Tsai, C.-M., & Frasch, C. E. (1982a). A sensitive silver stain for detecting lipopolysaccharides in polyacrylamide gels. *Analytical Biochemistry*, *119*(1), 115–119. https://doi.org/10.1016/0003-2697(82)90673-X

Tsai, C.-M., & Frasch, C. E. (1982b). A sensitive silver stain for detecting lipopolysaccharides in polyacrylamide gels. *Analytical Biochemistry*, *119*(1), 115–119. https://doi.org/10.1016/0003-2697(82)90673-X

Uruén, C., Chopo-Escuin, G., Tommassen, J., Mainar-Jaime, R. C., & Arenas, J. (2020). Biofilms as Promoters of Bacterial Antibiotic Resistance and Tolerance. *Antibiotics*, *10*(1), 3. https://doi.org/10.3390/antibiotics10010003

Vaccaro, M., Accardo, A., Tesauro, D., Mangiapia, G., Löf, D., Schillén, K., Söderman, O., Morelli, G., & Paduano, L. (2006). Supramolecular Aggregates of Amphiphilic Gadolinium Complexes as Blood Pool MRI/MRA Contrast Agents:

Physicochemical Characterization. *Langmuir*, *22*(15), 6635–6643. https://doi.org/10.1021/la053500k

Vassallo, V., Stellavato, A., Cimini, D., Pirozzi, A. V. A., Alfano, A., Cammarota, M., Balato, G., D'Addona, A., Ruosi, C., & Schiraldi, C. (2021). Unsulfated biotechnological chondroitin by itself as well as in combination with high molecular weight hyaluronan improves the inflammation profile in osteoarthritis in vitro model. *Journal of Cellular Biochemistry*, *122*(9), 1021–1036. https://doi.org/10.1002/jcb.29907

Vitiello, G., Luchini, A., Di Napoli, M., Gallucci, N., Cavasso, D., Koutsioubas, A., Varcamonti, M., Zanfardino, A., Fragneto, G., & Paduano, L. (2024). The affinity towards the hydrophobic region of biomimicking bacterial membranes drives the antimicrobial activity of EFV12 peptide from Lactobacillus gasseri gut microbiota. *Journal of Molecular Liquids*, *414*, 126086. https://doi.org/10.1016/j.molliq.2024.126086

Vuong, C., Gerke, C., Somerville, G. A., Fischer, E. R., & Otto, M. (2003). Quorum-Sensing Control of Biofilm Factors in *Staphylococcus epidermidis*. *The Journal of Infectious Diseases*, *188*(5), 706–718. https://doi.org/10.1086/377239

Weidenmaier, C., Kokai-Kun, J. F., Kristian, S. A., Chanturiya, T., Kalbacher, H., Gross, M., Nicholson, G., Neumeister, B., Mond, J. J., & Peschel, A. (2004). Role of teichoic acids in Staphylococcus aureus nasal colonization, a major risk factor in nosocomial infections. *Nature Medicine*, *10*(3), 243–245. https://doi.org/10.1038/nm991

Weidenmaier, C., & Peschel, A. (2008). Teichoic acids and related cell-wall glycopolymers in Gram-positive physiology and host interactions. *Nature Reviews Microbiology*, *6*(4), 276–287. https://doi.org/10.1038/nrmicro1861

Westphal. (1965). *Bacterial lipopolysaccharides: Extraction with phenol-water and further applications of the procedure.*

Whitfield, C., & Trent, M. S. (2014). Biosynthesis and Export of Bacterial Lipopolysaccharides. *Annual Review of Biochemistry*, *83*(1), 99–128. https://doi.org/10.1146/annurev-biochem-060713-035600

Wilton, M., Charron-Mazenod, L., Moore, R., & Lewenza, S. (2016). Extracellular DNA Acidifies Biofilms and Induces Aminoglycoside Resistance in Pseudomonas aeruginosa. *Antimicrobial Agents and Chemotherapy*, *60*(1), 544–553. https://doi.org/10.1128/AAC.01650-15

Yu, J. Y., Chuesiang, P., Shin, G. H., & Park, H. J. (2021). Post-Processing Techniques for the Improvement of Liposome Stability. *Pharmaceutics*, *13*(7), 1023. https://doi.org/10.3390/pharmaceutics13071023

Zhou, X., McGovern, A., Wells, M. J., Verma, D. B., Currie, H., Raka, A. M., Shen, J., Brown, K. A., Robertson-Anderson, R., & Gordon, V. D. (2023). *Incorporation of collagen into* Pseudomonas aeruginosa, Staphylococcus aureus *, and* Burkholderia pseudomallei *biofilms enhances their elasticity and resistance against phagocytic clearance*. Microbiology. https://doi.org/10.1101/2023.10.25.564018

Zhu, Y., Pan, Q., Thibaudeau, C., Zhao, S., Carmichael, I., & Serianni, A. S. (2006). [13C,15N]2-Acetamido-2-deoxy-d-aldohexoses and Their Methyl Glycosides: Synthesis and NMR Investigations of J-Couplings Involving 1H, 13C, and 15N. *The Journal of Organic Chemistry*, *71*(2), 466–479. https://doi.org/10.1021/jo051510k